Technical Report Documentation Page

1. Report No.	2. Government Accession No.	3. Recipient's Catalog No.

4. Title and Subtitle	5. Report Date
Development of Fatigue Design Procedures for Slender, Tapered Support Structures for Highway Signs, Luminaries, and Traffic Signals Subjected to Wind-Induced Excitation from Vortex Shedding and Buffeting	November 2007
	6. Performing Organization Code
7. Author(s)	**8. Performing Organization Report No.**
Brent M. Phares, Partha P. Sarkar, Terry J. Wipf, and Byungik Chang	
9. Performing Organization Name and Address	**10. Work Unit No. (TRAIS)**
Center for Transportation Research and Education Iowa State University 2711 South Loop Drive, Suite 4700 Ames, IA 50010-8664	**11. Contract or Grant No.**
12. Sponsoring Organization Name and Address	**13. Type of Report and Period Covered** Final Report
	14. Sponsoring Agency Code

15. Supplementary Notes

Visit www.ctre.iastate.edu for color PDF files of this and other research reports.

16. Abstract

Cantilevered signal, sign, and light support structures are used nationwide on major interstates, national highways, local highways, and at local intersections for traffic control purposes. Recently, there have been a number of failures of these structures that can likely be attributed to fatigue. In light of the fact that there is considerable uncertainty in the calculation of vortex shedding loads in both the American Association of State Highway and Transportation (AASHTO) and the Canadian Highway Bridge Design Code (CAN/CSA) code provisions, the current equations used for vortex shedding fatigue design need to be reevaluated and likely re-formulated or modified.

A luminary support structure or High Mast Light Pole (HMLP) is generally susceptible to two primary types of wind loading induced by natural wind gusts or buffeting and vortex shedding, both of which excite the structure dynamically and can cause fatigue damage. Vortex shedding is a unique type of wind load that alternatively creates areas of negative pressures on either side of a structure normal to the wind direction. This causes the structure to oscillate transverse to the wind direction.

The primary objective of this study was to develop a procedure for predicting wind loads in the time domain for the fatigue design of slender, tapered luminary support structures. To accomplish this, monitoring of long-term response behavior of a HMLP subjected to wind-induced vibration was needed. This was accomplished by full-scale measurement of the response of a HMLP located near Mason City next to I-35 in Iowa. Wind tunnel testing was also conducted to determine the required aerodynamic parameters of the pole cross section. Further, these aerodynamic parameters were cast into a coupled dynamic model for predicting the response of any HMLP in the time domain. Finally, the model was validated by comparing its results with the data collected from field monitoring.

17. Key Words	18. Distribution Statement
buffeting— fatigue design— indicial function—slender support structure—time domain model—vortex shedding—wind load	No restrictions.

19. Security Classification (of this report)	20. Security Classification (of this page)	21. No. of Pages	22. Price
Unclassified.	Unclassified.	116	NA

Form DOT F 1700.7 (8-72) **Reproduction of completed page authorized**

DEVELOPMENT OF FATIGUE PROCEDURES FOR SLENDER, TAPERED SUPPORT STRUCTURES FOR HIGHWAY SIGNS, LUMINARIES, AND TRAFFIC SIGNALS SUBJECTED TO WIND-INDUCED EXCITATION FROM VORTEX-SHEDDING AND BUFFETING

Final Report
November 2007

Principal Investigator
Brent M. Phares
Associate Director, Center for Transportation Research and Education
Associate Director, Bridge Engineering Center
Center for Transportation Research and Education, Iowa State University

Co-Principal Investigators
Partha P. Sarkar
Director, Wind Simulation and Testing Laboratory
Professor of Aerospace and Civil Engineering, Iowa State University

Terry J. Wipf
Professor of Civil Engineering
Director, Bridge Engineering Center
Center for Transportation Research and Education, Iowa State University

Research Assistant
Byungik Chang

Authors
Brent M. Phares, Partha P. Sarkar, Terry J. Wipf, and Byungik Chang

Preparation of this report was financed in part
through funds provided by the U.S. Department of Transportation
through the Midwest Transportation Consortium, Project 2005-02

A report from
Midwest Transportation Consortium
2711 South Loop Drive, Suite 4700
Ames, IA 50010-8664
Phone: 515-294-8103
Fax: 515-294-0467
www.ctre.iastate.edu/mtc

TABLE OF CONTENTS

LIST OF FIGURES

LIST OF TABLES

ACKNOWLEDGMENTS

The investigation presented in this report was conducted by the Bridge Engineering Center under the auspices of the Center for Transportation Research and Education at Iowa State University. The research was sponsored by the Iowa Department of Transportation and Midwest Transportation Consortium.

The authors wish to thank the numerous staff within the Office of Bridges and Structures at the Iowa DOT for their technical guidance and input during the research. Special thanks are accorded to Ian C. Hodgson, Research Engineer at the Advanced Technology for Large Structural Systems (ATLSS), in Lehigh University, who supported numerous aspects of the long-term monitoring, and William Rickard, Senior Technician in Wind Simulation and Testing (WiST) Laboratory, who guided the wind tunnel tests.

EXECUTIVE SUMMARY

Cantilevered signal, sign, and light support structures are used nationwide on major interstates, national highways, local highways, and at local intersections for traffic control purposes. Recently, there have been a number of failures of these structures that can likely be attributed to fatigue. In light of the fact that there is considerable uncertainty in the calculation of vortex shedding loads in both the American Association of State Highway and Transportation (AASHTO) and the Canadian Highway Bridge Design Code (CAN/CSA) code provisions, the current equations used for vortex shedding fatigue design need to be reevaluated and likely re-formulated or modified.

A luminary support structure or High Mast Light Pole (HMLP) is generally susceptible to two primary types of wind loading induced by natural wind gusts or buffeting and vortex shedding, both of which excite the structure dynamically and can cause fatigue damage. Vortex shedding is a unique type of wind load that alternatively creates areas of negative pressures on either side of a structure normal to the wind direction. This causes the structure to oscillate transverse to the wind direction.

The primary objective of this study was to develop a procedure for predicting wind loads in the time domain for the fatigue design of slender, tapered luminary support structures. To accomplish this, monitoring of long-term response behavior of a HMLP subjected to wind-induced vibration was needed. This was accomplished by full-scale measurement of the response of a HMLP located near Mason City next to I-35 in Iowa. Wind tunnel testing was also conducted to determine the required aerodynamic parameters of the pole cross section. Further, these aerodynamic parameters were cast into a coupled dynamic model for predicting the response of any HMLP in the time domain. Finally, the model was validated by comparing its results with the data collected from field monitoring.

1. INTRODUCTION

1.1. Problem Statement

Cantilevered signal, sign, and light support structures are used nationwide on major interstates, national highways, local highways, and at local intersections for traffic control purposes. Recently, there have been a number of failures of these structures that can likely be attributed to fatigue. According to National Cooperative Highway Research Program (NCHRP) Report 469 [1], most states have experienced failure of support structures. Table 1-1 [1] lists states that have reported problems with sign, signal, or light support structures. To date, these failures have not received significant attention in the mainstream media because, fortunately, no one has been injured or killed.

In Iowa, a high-mast light pole (HMLP), which are typically used at major interstate junctions, erected for service in 2001 along I-29 near Sioux City collapsed in November 2003 (see Fig. 1-1 [3]). Fortunately, the light pole fell onto an open area parallel to the interstate and injured no one. Following that failure, a state-wide special inspection revealed cracks in more than twenty other poles across the state. Most of these were taken out of service until a retrofit could be developed. Using the procedure contained in the Canadian Highway Bridge Design Code (CAN/CSA) [2], further study revealed that the identified cracking was likely due to wind-induced vibrations and, given the orientation of the cracking and knowledge of probable wind directions, were most likely due to vortex shedding induced loadings [3].

In February 2003, approximately 140 tapered aluminum light poles in western Illinois collapsed during a winter storm. At the time of preparation of this report, the cause of the failures was still under investigation; preliminary results seem to indicate that the collapse mechanism appears to have been due to traffic or wind-induced vibrations [4]. The Wisconsin Department of Transportation has also experienced failures of high-mast luminary support structures and cracking has been found in other support structures across the state [5]. The Missouri Department of Transportation discovered and documented failures of several cantilever mast arms in 1997 [6]. Investigations showed that both the Wisconsin and Missouri incidents were caused by fatigue due to wind-induced vibrations.

Of the 233 high-mast light poles in Iowa, over 10% have known fatigue problems. This is an alarmingly high number. These problems are likely due to a lack of understanding of the behavior of and loadings on luminary support structures.

In short, it appears that these structures may have been designed based on incomplete and/or insufficient code provisions. Specific deficiencies may include a lack of understanding of actual wind loads (including the dynamic effects of vortex shedding induced excitation), modes of vibration, and others.

Table 1-1. Documented fatigue cracking of sign, signal and light support structures

State	Date	Failed Component(s)	Notes
AK	1994	Column base	High-mast luminaries
AR	N.A.	Column base	Cracked fillet welds between baseplate and stiffener
		Truss connections	Cracked tube-to-tube welds
CA	1995	Column base	Failure of VMS after 18 months , AaLoose/missing anchor rods
	1999	Column base	Failure from socket-weld cracking
CO	1994	Mast arm connection	Failures in 3 sign structures over 5 years old
CT	1996	N.A.	Crack found during inspection
		Truss connection (Alumn.)	Crack found during inspection
FL	1996	N.A.	Excessive deflections on overhead VMS structure
	1997	Mast arm connections	15-m span signal support structure
GA	1994	Anchor bolt	Failed bridge support structure
ID	N.A.	Truss connections (Alumn.)	Tube-to-tube welds
IL	N.A.	Mast arm connection	N.A.
KS	1997?	N.A.	Failure of numerous signal structures
KY	N.A.	Column base	Cracks found in fillet welds connecting stiffener
		Truss connections (Alumn.)	50 cracked tube-to-tube welds
LA	N.A.	Anchor rods	Found to be loose/missing
MD	N.A.	High mast luminaries	Weathering steel
MI	1990	Anchor rods	Failure of 2 sign structures with truss-type mast arms etc.
	N.A.	Mast arm connection	Cracks in pipe wall at weld termination
	N.A.	Truss connections	Cracks in pipe wall near tube-to-tube weld
MN	1999	Handhole	Crack found near handhole
MO	1996	Mast arm connection	Failures of several signal support structures

Note: N.A. – data not available

Table 1-1. (Continued)

State	Date	Failed Component(s)	Notes
NE	N.A.	Monotube signs	N.A.
NV	1996	N.A.	Failure of VMS structure
NH	1993?	Truss connections (Alumn.)	Found many cracks during inspection
NJ	1995	N.A.	Excessive deflection on VMS
	N.A.	Column base	Failures of light poles
NM	1992	Column base	Failure of VMS socket joint after only a few weeks
	N.A.	Anchor rods	Found to be loose/missing
	N.A.	Hand hole	Cracking discovered
NC	N.A.	Anchor rods	Found to be loose/missing
ND	1998	N.A.	Excessive vibration of 15-m span signal
OR	1993	Column base	Failure of 25% of 160 straight square light poles in 6 months
TX	N.A.	N.A.	Excessive vibration of signal poles
		Anchor rods	Found to be loose/missing
VA	1993	Column base, Anchor rods	Cantilevered variable message sign
	1996	N.A.	Cantilevered variable message sign
	N.A.	Truss connections	Cracked tube-to-tube welds
	N.A.	Anchor rods	Found to be loose
WA	N.A.	Anchor rods	Found loose or missing in cantilever sign structures
		Truss connections	Cracked welds at ends of diagonals
WV	N.A.	Anchor rods	Found cracked/loose/missing during inspection
		Base and mast arm connections	Cracks found at toe of groove weld etc.
WI	1997	Numerous	N.A.
WY	1995	Mast arm connection	Cracks in 30% of signal structures inspected
	N.A.	Anchor rods	Found to be loose/missing

Figure 1-1. A collapsed high-mast light pole along I29 near Sioux City in 2003

1.2. Background

A luminary support structure or HMLP is generally susceptible to two primary types of wind loading induced by natural wind gusts, or buffeting and vortex shedding, both of which excite the structure dynamically and can cause fatigue damage [7]. Vortex shedding is a unique type of wind load that alternatively creates areas of negative pressures on either side of a structure normal to the wind direction. This causes the structure to oscillate transverse to the wind direction. When the vortex shedding frequency (i.e., the frequency of the negative pressure on one side of the structure) approaches the natural frequency of the structure, there is a tendency for the vortex shedding frequency to couple with the frequency of the structure (also referred to as "lock-in" phenomenon) causing greatly amplified displacements and stresses. Although a great deal of effort has been made during recent years to improve the analytical models used for predicting fatigue failure due to vortex shedding excitation, these models still need further refinement because they can fail to accurately capture the causes of this phenomenon.

While vortex shedding occurs at specific frequencies and causes amplified vibration near the natural frequencies of the structure, buffeting is a relatively "broad-band" excitation and includes frequencies of eddies that are present in the natural wind (usually up to 2 Hz) as well as those caused by wind-structure interactions. The dynamic excitation from buffeting can be significant if the mean wind speed is high, the natural frequencies of the structure are below 1 Hz, the wind turbulence intensity is high with a wind turbulence that is highly correlated in space, the structural shape is aerodynamically odd with a relatively rough surface, and the mechanical damping is low. In practice, a structure is always subject to both vortex shedding and buffeting

excitations. But unlike vortex shedding, where amplified dynamic excitation occurs within a short range of wind speeds, buffeting loads keep increasing with higher wind speeds. Thus, both phenomena are important and must be considered together.

The collapse or cracking occurring in support structures throughout the U.S. shows that there may be considerable uncertainty regarding the type of vibration and the level of stresses that wind is inducing in high-mast light poles. To date, cracking in Iowa poles has occurred only in towers constructed since 1991 and most cracks have been found in galvanized towers which have been constructed since 2000. The obvious questions could be why cracking has not occurred in towers constructed in the 1970s and 1980s and what is the potential for more cracking of towers erected since 1990 [8].

Invariably, the cracked HMLPs identified in Iowa were designed to the 1994 American Association of State Highway and Transportation (AASHTO) Specifications [9] which did not include comprehensive provisions for designing for fatigue due to vortex shedding-induced vibrations. In fact, the 2001 AASHTO Standard Specifications for Structural Supports for Highway Signs, Luminaries, and Traffic Signals [7] was the first edition to include provisions for fatigue design. However, the 2001 Specification has deficiencies that need to be modified to, at a minimum, require that all tapered support structures be checked for vortex shedding with appropriate loadings and checked for higher vibration modes (other than only the first mode as currently required). Significant deficiencies also exist in understanding the specific wind loading, general behavior of the support structures, and the interaction between the two.

The 2001 AASHTO Specification was developed based upon several phases of NCHRP sponsored research [1, 10, 11, and 12], during which a limited number of support structures were tested. Because of the limited scope and general test results, there is still uncertainty. In fact, there remain significant differences between the 2001 AASHTO Specifications and the CAN/CSA [2] procedure for the fatigue design of support structures. In light of the fact that there is considerable uncertainty in the calculation of vortex shedding loads in both the AASHTO and CAN/CSA code provisions, the current equations used for vortex shedding fatigue design need to be reevaluated and likely re-formulated or modified.

1.3. Objectives

The primary objective of this study was to develop a procedure for predicting wind loads in the time domain for the fatigue design of slender, tapered luminary support structures. To accomplish this, monitoring of long-term response behavior of a HMLP subjected to wind-induced vibration was needed. This was accomplished by full-scale measurement of the response of a HMLP located near Mason City next to I-35 in Iowa. The collection and evaluation of the HMLP performance data through monitoring (especially in an area known for high-wind occurrences) is an important, and unique, tool for understanding the known high-mast light pole problems and for the advancement of the future code provisions. From the long-term field monitoring, the two critical types of wind vibration (natural wind gusts or buffeting and vortex shedding) were extracted for in-depth analysis.

In order to develop the fatigue design procedure for wind-induced pressures on a structure, several wind parameters, such as the static drag coefficient, the slope of aerodynamic lift coefficient, Strouhal number, the lock-in range of wind velocities producing vibrations, and variation of amplitude of vortex-induced vibration with Scruton number, are required. Based on wind tunnel experiments and long-term monitoring, wind parameters and load profile parameters were obtained for a dodecagonal (12-sided cross section) tapered structure. Although several aerodynamic coefficients are known from past wind-tunnel test results, they needed to be refined based on further wind tunnel tests.

Mathematical modeling of the wind speed distribution and stress amplitudes was developed in the time-domain model and was compared with those calculated with the full-scale data. Based on the field monitoring results and the mathematical modeling results, it appears as though the developed procedures accurately predict buffeting and vortex shedding loads on slender tapered support structures.

1.4. Final Report Summary

This report is divided into six chapters. A literature review related to wind induced vibration is presented in Chapter 2. Chapter 3 presents the instrumentation utilized to monitor the high mast light poles in Iowa and the associated data analysis results. Wind tunnel testing configurations and the results are discussed in Chapter 4. In Chapter 5, a discussion of the mathematical modeling with specific consideration to the field data is given. Chapter 6 presents several concluding remarks and recommendations for predicting loads on a HMLP.

2. LITERATURE REVIEW

2.1. NCHRP Reports

Numerous studies have been completed to look at various aspects of wind induced vibration and the modeling of support structures. As an example, NCHRP report 469 [1], which provides a comprehensive assessment of the design provisions developed in NCHRP Report 412 [11], shows a tapered luminary support structure that was captured on videotape vibrating in double curvature. One of the conclusions from NCHRP report 469 was that there is a need for revision of the 2001 AASHTO Specification, with respect to vortex shedding fatigue design, which should be completed in parallel with long-term field testing.

Since the 1985 Edition of the AASHTO Specification was published, significant changes have occurred in design philosophies, material choices, and manufacturing processes for support structures. NCHRP Report 411 [10] provides detailed information on the development of wind loading criteria, revised allowable bending stresses, deflection limitations, and others for a proposed specification. NCHRP Report 494 [12] was prepared, for consideration of AASHTO, to address differences in the wind speed maps, the differences in design loads resulting from wind speed maps, and the treatment of gusts.

In NCHRP Report 412 [11], which was based on a master's thesis published at Lehigh University [13], the authors found more than half of states in the United States had experienced problems with wind-induced vibration of cantilevered support structures. NCHRP Report 412 stated that tapered light poles should generally not be susceptible to vortex shedding and the associated vibration and fatigue. This assertion was based primarily upon the Ontario Highway Bridge Design Code (OHBDC) [2], which states that the vortex shedding should only take place on a tapered light pole over a range of diameters from -10% to +10% of the critical diameter as determined by the Strouhal relation. Researchers from University of Western Ontario believe that the ±10% rule is not valid for first mode vibrations.

2.2. State Transportation Authority Research on Support Structures

Following the failure of a high-mast luminary support structure in Wisconsin [5], the response of support structures due to wind induced vibrations was investigated by analytical modeling. The analytical study suggested that vortex shedding need not be considered for high mast luminary support structures. Others [3], however, have pointed out the importance of vortex shedding after a limited investigation of cracking of high-mast luminary support structures in Iowa. It has also been acknowledged in other respects [14 to 17] that there is a need for field testing to verify vortex shedding loads and their impact on high mast luminary support structures.

The Wyoming DOT [18 and 19] recently experienced several failures of traffic signal structures and, as a result, inspected all poles in their inventory. It was found that one-third of the poles had fatigue cracks and various research projects [20 and 21] which were related to vibration mitigation, field monitoring, analytical analysis, and experimental testing were initiated. The Illinois DOT [22] combined pertinent wind loading and vibration theory, fatigue damage theory,

and experimental data into a fatigue analysis method for overhead sign and signal structures. In the project report, vibrations and forces induced by vortex shedding were studied analytically and measured experimentally.

University Transportation Center for Alabama (UTCA) [23 and 24] studied the impact of the new wind load provisions on the design of structural supports from the standpoint of safety and economy. UTCA [25] also developed computer-based design tools for the design of sign, luminaries and traffic signal supports that incorporates the latest adopted design guides and specifications. The University of Maryland [26] has similarly developed a program, which is called Sign Bridge Analysis and Evaluation System (SABRE), to shorten and simplify the design/analysis process for sign support structures. The Connecticut DOT [27 and 28], New York DOT [29], and Texas DOT [30] have also revised their overall design approach for support structures based upon the AASHTO 2001 Specification.

The Missouri DOT [31] investigated and documented failures of several cantilever mast arms in recent years. They found the main cause for the premature fatigue failure of the mast arms to be poor weld quality. The Florida DOT [32] conducted lab tests to develop a damping device to mitigate wind-induced vibrations in cantilevered mast arm signal structures and it was stated that a 3 ft tapered impact damper would be effective in preventing excessive displacements in cantilevered mast arm structures. Extensive research [33] was performed by Texas Tech and the Texas DOT due to the collapse of a cantilevered signal pole in 1991. The project aimed to revise the wind loads section of the Texas DOT standard for support structures and to develop strategies to mitigate vibrations in single mast traffic structures.

The Colorado DOT [34] recently studied the method and results for the development of a reliability-based design procedure for high-mast lighting structural supports. The research [35] performed by the Colorado DOT and Colorado State University resulted in the development of a comprehensive numerical analysis procedure for modeling the spatial correlation of wind turbulence and vortex shedding effects on the response resultant loading and fatigue performance of a slender structural system.

2.3. Wind Engineering

The general aerodynamic phenomena that should be considered are vortex shedding, buffeting, galloping and flutter. Slender tapered support structures are usually susceptible to two types of wind loading that may induce vibrations causing fatigue damage [7]. The two wind-loading types result from vortex shedding and natural wind gusts or buffeting. The purpose of this section is to define these phenomena and to present information from related research.

2.3.1. Vortex Shedding

Vortex-induced vibrations occur when vortices are shed alternately from opposite sides of an object [36]. This results in a fluctuating load which induces vibration perpendicular to the wind direction as depicted in Fig. 2-1 [36]. As a steady and uniform airflow travels over the face of a body, it reaches points of separation on each side where thin sheets of tiny vortices are

generated. As the vortex sheets detach, they interact with one another and roll up into discrete vortices that are shed alternately from the sides of the object. The sinusoidal pattern that forms in the wake of the object is known as a Von Karman street. The asymmetric pressure distribution by the vortices around the cross section results in a sinusoidal forcing function transverse to the object [36].

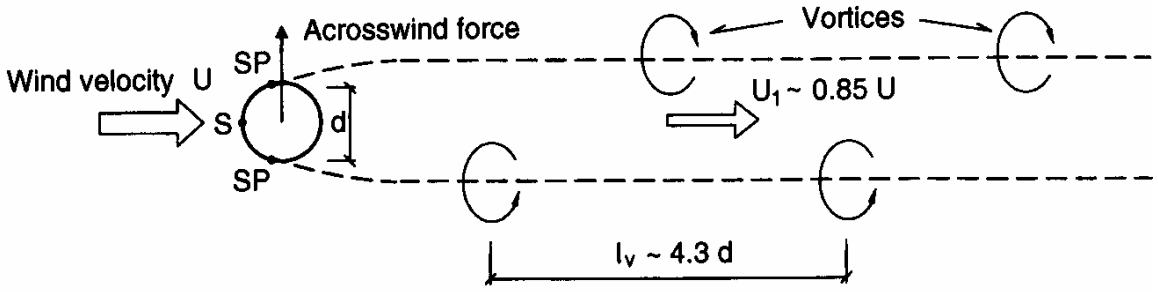

Note: S-point of stagnation
SP-points of separation where the vortices separate from the structure

Figure 2-1. Vortex street behind a cylinder

For a circular cylinder, the aerodynamic behavior of the wake, including the flow characteristics, Strouhal number, and correlation of vortex shedding along the length, are sensitive to a large number of influences; Reynolds number, surface roughness, and the turbulence scale intensity [37]. The following briefly describe these influences.

Reynolds number

Vortex shedding from smooth, circular cylinders with steady subsonic flow is a function of the Reynolds number. The Reynolds number is defined as the ratio of the inertial force and the viscous force on a body and is a parameter that is used to indicate dynamic similarity. When the ratio of these two forces is large, inertial forces control the fluid force balance; when the ratio is small, the viscous forces control. To evaluate the tendency for vortex shedding on a generic object, the Reynolds number, R_e (Eq. 2.1) [38], is commonly used and is given by:

$$R_e = \frac{\rho \cdot U \cdot D}{\mu} = \frac{U \cdot D}{\nu}, \tag{2.1}$$

where, U = the wind velocity

ρ = the flow density

μ = the coefficient of fluid viscosity

D = cross-wind dimension of the cross-section

ν = the coefficient of kinematics fluid viscosity (1.564×10^{-4} ft^2/sec for air)

It is commonly agreed that when the Reynolds number for a circular cylinder is between 300 and 3.5×10^5 vortex shedding is periodic and strong (see Fig. 2-2 [39]). In this range, the behavior is called subcritical. The supercritical range (Reynolds number greater than 3.5×10^6) is characterized by re-established vortex shedding with a turbulent boundary layer [39].

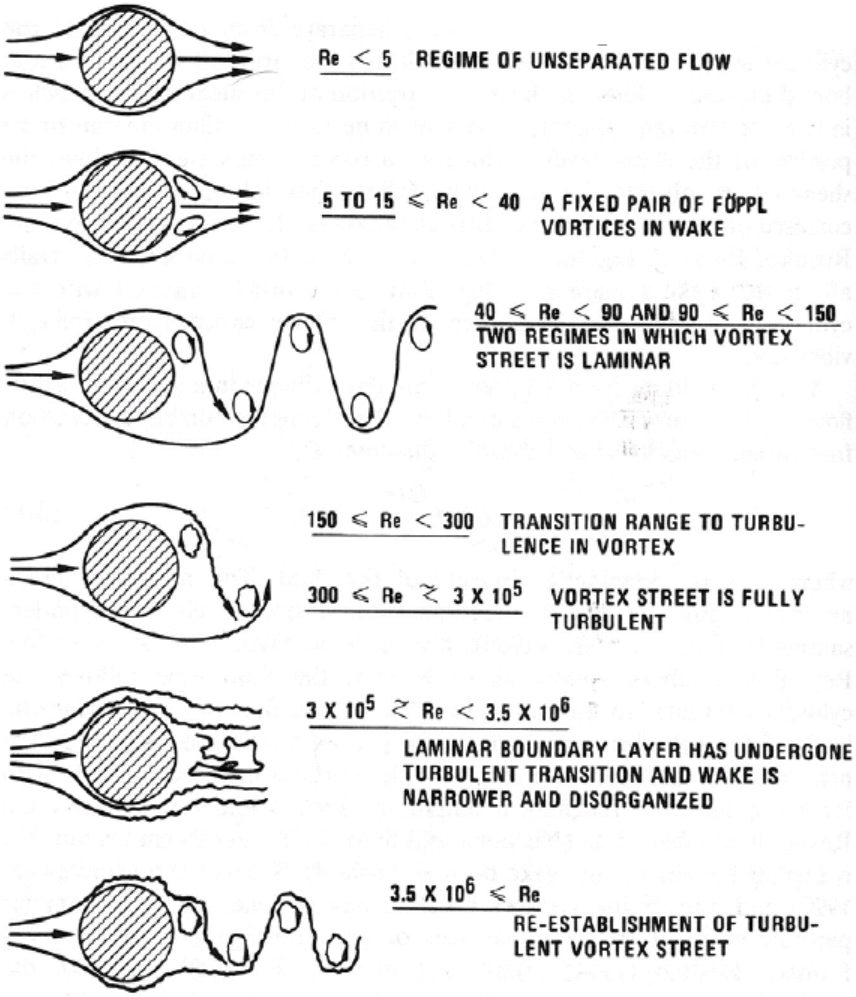

Figure 2-2. Regimes of fluid flow across smooth circular cylinders

Strouhal number

Within a certain range of flow velocities, a stationary bluff body sheds alternating vortices into the trailing wake at regular frequencies according to the Strouhal relation. The Strouhal number is a dimensionless proportional constant which relates the predominant vortex shedding frequency f_s, the free stream velocity, and the cylinder diameter. The Strouhal number (Eq. 2.2) [39] of a stationary circular cylinder is given by:

$$S_t = \frac{f_s \cdot D}{U}, \tag{2.2}$$

where, f_s = vortex shedding frequency

D = cross-wind dimension of the cross-section

U = the wind velocity

Throughout the subcritical range where the vortex shedding is strongest, $300 < Re < 3.0 \times 10^5$, the Strouhal number varies only slightly and is approximately 0.21 as shown in Fig. 2-3 [39]. At the upper end of the subcritical range, near the critical Reynolds number of 2.0×10^5, an abrupt shift of the separation point and a sudden decrease in the drag coefficient occur. Beyond this point and into the transitional range, the flow around smooth cylinders results in the irregular formation of separation bubbles that generate a chaotic, disorganized, high frequency wake and Strouhal numbers as high as 0.46.

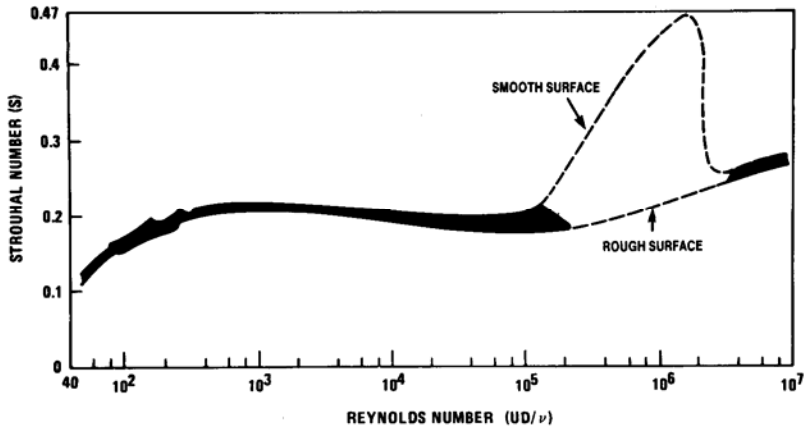

Figure 2-3. Strouhal number-Reynolds number relationship for circular cylinders

Lock-in phenomenon

If the vortex shedding frequency is sufficiently different, either smaller or greater, than the natural frequency of structure, there is little interaction between the near-wake dynamics and structural motion [37]. When the vortex shedding frequency approaches the natural frequency of the structure, an increase in vortex strength results and a tendency develops for the vortex shedding frequency to couple with the structure producing greatly amplified displacements and stresses. The wind velocity at the beginning of this phenomenon is known as the lock-in velocity, $U_{lock-in}$ (Eq. 2.3) [38] that expressed as given.

$$U_{lock-in} = \frac{f_n \cdot D}{S_t}, \tag{2.3}$$

where, f_n = the natural frequency of the structure

D = cross-wind dimension of the cross-section

S_t = the Strouhal number

The effect of lock-in on the vortex shedding frequency is represented in Fig. 2-4 [39]. In the lock-in region, the vortex shedding frequency is constant and nearly equal to the natural frequency of structure, rather than a linear function of the wind velocity as expressed in the Strouhal relationship [39].

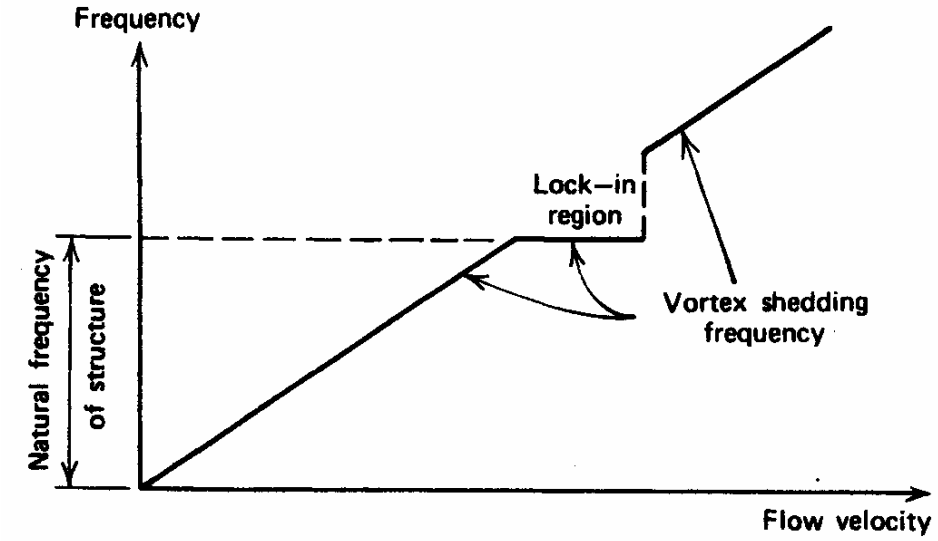

Figure 2-4. Evolution of vortex-shedding frequency with wind velocity over elastic structure

Figure 2-5 [39] depicts some illustrative experimental results for deflection response of an elastically supported circular cylinder before lock-in, at lock-in, and after lock-in, respectively. Further, the corresponding displacement spectra, where f_s, f_n are the vortex shedding and natural structural frequencies, respectively, are described in the figure.

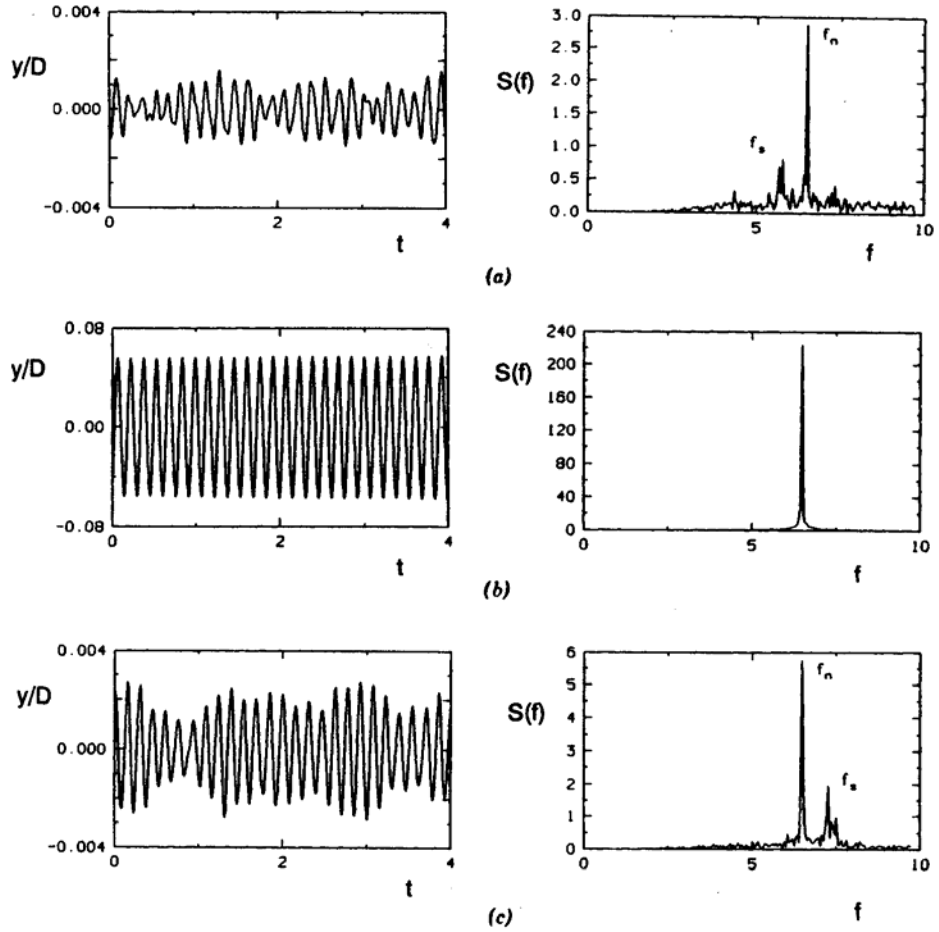

Figure 2-5. Across-flow oscillations y/D of elastically supported circular cylinder (a) before lock-in; (b) at lock-in; (c) after lock-in

The reduced velocity at lock-in, V_r, is equal to the inverse of the Strouhal number with the natural frequency of the structure, f_n, substituted for the vortex shedding frequency, f_s. For a circular cylinder of adequate length, lock-in begins when the ratio of f_s to f_n, is nearly 1.0 and ends when the ratio is approximately 1.40 [38]. The transverse vibration of a spring-mounted circular cylinder is shown in Fig. 2-6 [39].

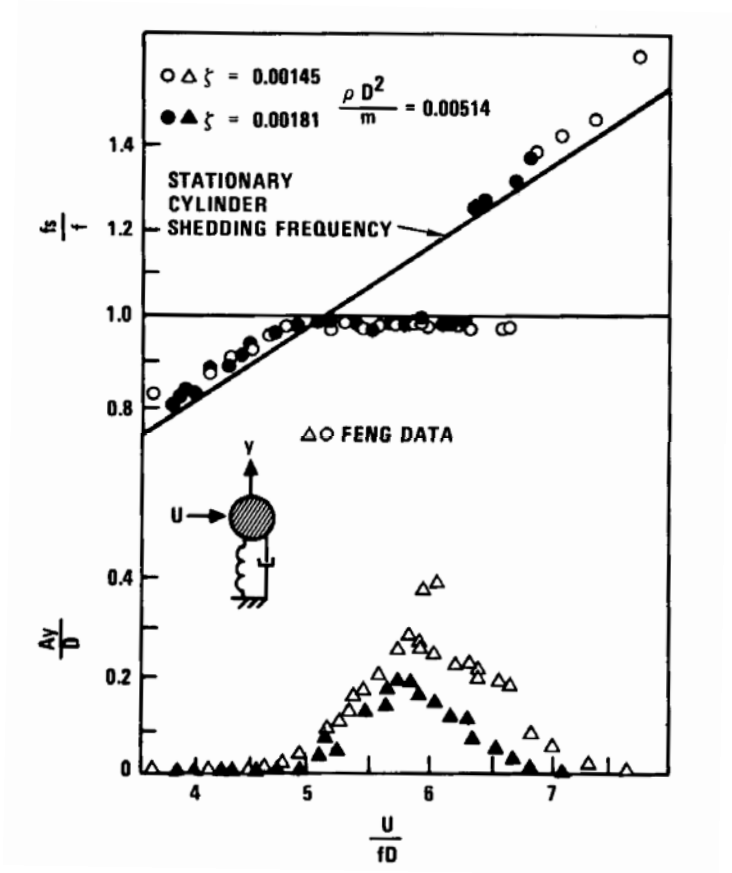

Figure 2-6. Vortex-induced vibration of a spring-supported, damped circular cylinder

2.3.2. Model for Vortex-Induced Vibration

Because vortex shedding is a more or less sinusoidal process, it is reasonable to model the vortex shedding transverse force imposed on a circular cylinder as harmonic in time at the shedding frequency [39]. The time varying force, $F_{vy}(t)$, in Scanlan's model [39], can be expressed as:

$$F_{vy}(t) = \frac{1}{2} \cdot \rho \cdot U^2 \cdot A \cdot \left[Y_1(k) \cdot (1 - \varepsilon \cdot \frac{y^2}{D^2}) \cdot \frac{\dot{y}}{U} + Y_2(k) \cdot \frac{y}{D} + \widetilde{C}_L(k) \cdot \sin(\omega_n \cdot t + \phi) \right] \tag{2.4}$$

where,

U = the wind velocity

A = Projected area of the structure

Y_1, ε, and Y_2 = aerodynamic functions of reduced frequency, k, at lock-in

D = cross-wind dimension of the cross-section

$\widetilde{C}_L$ = rms of lift coefficient

ω_n = the natural frequency

t = time

ϕ = phase angle

$(\dot{})$ = derivative with respect to time

The displacement magnitudes at lock-in are governed both by the structure's inherent damping characteristics and by the mass ratio between the structure and the fluid it displaces. These two effects are often combined in the Scruton number, S_c (Eq. 2.5) [38], defined as:

$$S_c = \frac{m\zeta}{\rho D^2}, \tag{2.5}$$

where, m = mass per unit length

ζ = critical damping ratio

ρ = flow density

D = cross-wind dimension of the cross-section

In previous research conducted by Griffin, Skop, and Ramberg [39], the Scruton number was used in an empirical formula (Eq. 2.6) to predict the maximum displacement amplitude for a circular cylinder. Figure 2-7 [39] shows the maximum amplitudes versus Scruton number based on the empirical formula.

$$\frac{y_0}{D} = \frac{1.29}{[1 + 0.43 \cdot (8\pi^2 \cdot S_t^{\,2} \cdot S_c)]^{3.35}}, \tag{2.6}$$

where, y_0 = maximum amplitude

D = cross-wind dimension of the cross-section

S_t = the Strouhal number

S_c = the Scruton number

It is also thought that the vortex shedding mechanism is not quite uniformly distributed along the cylinder axis (i.e., the cross correlation of the exciting force decreases along the axis [40]). In the case of a cantilevered structure, the maximum of the exciting force is below the top of the cantilever because disturbances of the three-dimensional flow around the top reduces the response and interrupts the vortex shedding.

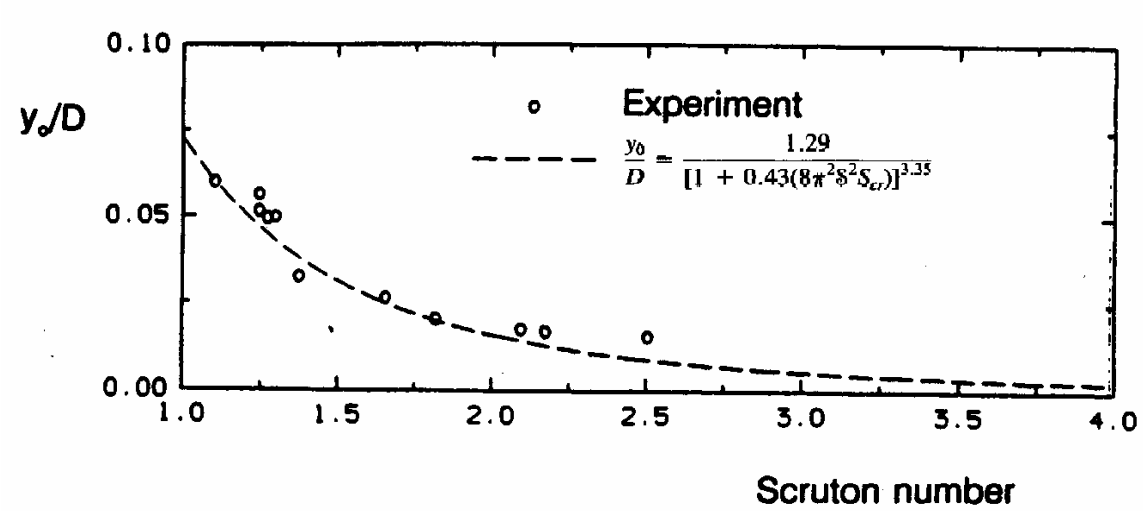

Figure 2-7. Maximum amplitude versus Scruton number

2.3.3. Buffeting

Buffeting is defined as the unsteady loading of a structure by velocity fluctuations in the incoming flow and is not self-induced [39]. While vortex shedding occurs at specific frequencies and causes amplified vibration near the natural frequencies of the structure, buffeting is a relatively "broad-band" excitation and includes frequencies of eddies that are present in the natural wind (usually up to 2 Hz) as well as those caused by wind-structure interaction. The dynamic excitation from buffeting can be significant if the mean wind speed is high, the natural frequencies of the structure are below 1 Hz, the wind turbulence intensity is high with a wind turbulence that is highly correlated in space, the structural shape is aerodynamically odd with a relatively rough surface, and the mechanical damping is low. In practice, a structure is always subject to both vortex shedding and buffeting excitations. But unlike vortex shedding, where amplified dynamic excitation occurs within a short range of wind speeds, buffeting loads keep increasing with higher wind speeds.

Aerodynamic Admittance Function

The relationship in the frequency domain between turbulence in the upstream flow and fluctuating wind load that it induces on a structure can be defined in terms of aerodynamic admittance that is a function of reduced frequency. A similar relationship in the time domain can be defined in terms of buffeting indicial functions. Generally, these relationships need to be determined experimentally since the flow around a structure in turbulent wind is too complex to be handled analytically.

An expression, known as Sears' function (Eq. 2.7), for the aerodynamic admittance of a thin symmetrical airfoil was theoretically derived by Sears [41], and Liepmann [42] suggested a somewhat simpler expression shown in Eq. 2.8. Jancauskas [43 and 44] verified the Sears'

theoretical plot experimentally for an airfoil and gave an approximate expression (see Fig. 2-8 [46]) as defined in Eq. 2.9. In addition, Scanlan and Jones [45] and Scanlan [46] studied the admittance functions for various structures.

$$\chi_{\text{aero}}(\text{n}) = \frac{J_0(k)\cdot K_1(i\cdot k) + i\cdot J_1(k)\cdot K_0(i\cdot k)}{K_1(i\cdot k) + K_0(i\cdot k)} \tag{2.7}$$

where, J_0 and J_1 = Bessel functions of the first kind

K_0 and K_1 = modified Bessel functions of the second kind

k = reduced frequency = $\text{n}\cdot\text{c}\cdot\pi$ / U

n = frequency (Hz)

c = chord length of an airfoil

U = mean wind velocity

$$\chi^2_{\text{aero}}(\text{n}) = \frac{1}{1 + 2\cdot\pi^2(\text{n}\cdot\text{c} / \text{U})} \tag{2.8}$$

where, $\chi^2_{\text{aero}}(\text{n})$ = aerodynamic admittance

$$\chi^2_{\text{aero}}(\text{k}) = \frac{1}{1 + 5\cdot k} \tag{2.9}$$

where, k = reduced frequency = $\text{n}\cdot\pi\cdot\text{c}$ / U

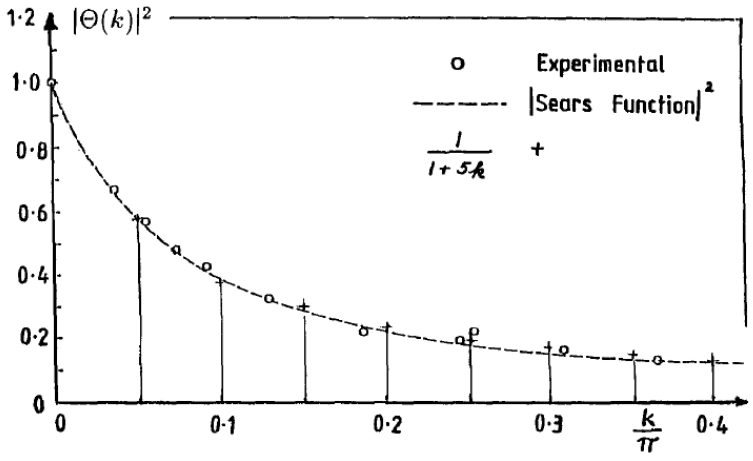

Figure 2-8. Airfoil aerodynamic admittance

Figure 2-9 [47] shows limited experimental data with an empirical function developed by Vickery [47] for a square plate in turbulent flow. The aerodynamic admittance function for drag on a flat plate is defined in Eq. 2.10. As shown in Figs. 2-8 and 2-9, low frequency gusts are nearly fully correlated, and fully envelope the face of s structure. For high frequencies, or very large bodies, the gusts are ineffective in producing total forces on the structure, due to their lack of correlation, and the aerodynamic admittance tends towards zero.

$$\left|\chi_u(n)\right| = 1/\left[1+\left(\frac{2\cdot n\sqrt{A}}{U}\right)^{4/3}\right] \text{ or } \chi_u(k)^2 = 1/\left[1+\left(\frac{k}{\pi}\right)^{4/3}\right]^2 \qquad (2.10)$$

where, A = projected area of the plate normal to the flow

k = reduced frequency = $\omega\cdot\sqrt{A}$ / U

D = the depth of body dimension

U = mean wind velocity

ω = 2·π·n

Hatanaka and Tanaka [48] proposed a new prediction method of developing aerodynamic admittance functions for lift and moment utilizing flutter derivatives. In their research, they compared the predicted values with the measured ones in the flow of actively generated turbulence. Peil and Behrens [49] recently investigated the influence of the lateral turbulence on the design of high and slender structures based on a nonlinear spectral approach which is confined to the correlated parts of the wind turbulence and the associated wind forces.

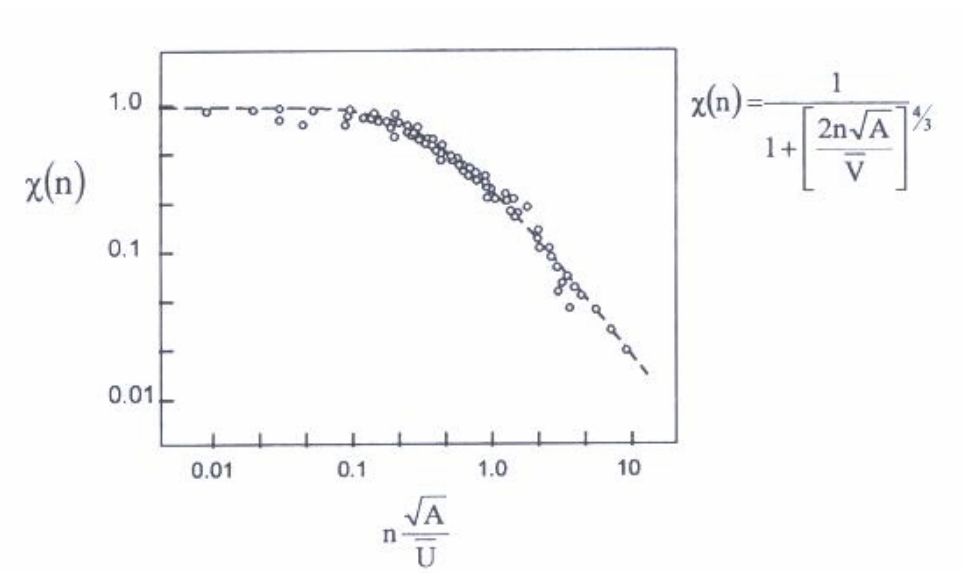

Figure 2-9. Aerodynamic admittance for a square plate in turbulent flow

Buffeting Indicial Function

It has been postulated that the aerodynamic admittance functions and the buffeting indicial functions are related. An expression, known as the Küssner function, for the indicial function of an airfoil was defined approximately by Jones [50] based on the Sears' function and its derivative, $\phi_w^{'}(s)$, (Eq. 2.11) is expressed with respect to non-dimensional time, s.

$$\phi_w^{'}(s) = 0.065 \cdot e^{-0.130 \cdot s} + 0.500 \cdot e^{-s} \tag{2.11}$$

where, s = non-dimensional time = U·t/c

t = time

c = chord length of an airfoil

U = mean wind velocity

Based on the theoretical expression, the effects of aerodynamic coupling on the buffeting and flutter response have been addressed by past studies. Chen and Kareem [51 and 52] worked in modeling aerodynamic phenomena, buffeting and flutter, in both the time and frequency domains, and Scanlan [46, 53, and 54], Jones [45 and 55], Zhang et. al. [56], and Costa [57 and 58] studied the indicial aerodynamic functions and admittance functions for bridge decks in time domain as well as in frequency domain.

2.4. Wind-Tunnel Testing and Full-Scale Measurements

The use of wind tunnels to aid in structural design and planning has been steadily increasing in recent years [59]. Full-scale measurements, however, are useful in their capability to quantify the boundary conditions, study the interaction between all parts of the structure, structural damping and its dependence on deflection, and, mainly, the exact conditions of wind loading [60].

2.4.1. Wind-Tunnel Test

Kitagawa et al [61] conducted a wind tunnel experiment using a circular cylinder tower to study the characteristics of the across-wind response at a high wind speed. The authors found from the tests that both the vortex induced vibration at a high wind speed and the ordinary vortex induced vibration were observed under uniform flow.

Bosch and Guterres [62] conducted wind tunnel experiments to establish the effects of wind on tapered cylinders using a total of 53 models representing a range of cross sections, taper ratios, and shapes (circular, octagonal, or hexagonal cross section), which were intended to be representative of those commonly found in highway structures. In a test of drag coefficient versus Reynolds number for the uniform circular cylinders, the results showed a consistent trend

of convergence with a range of Reynolds number for which drag coefficient flattens out to a constant value. It was also found that the introduction of taper ratio significantly altered the aerodynamic behavior of the cylinder shapes.

Wind tunnel experiments by James [63] were performed to establish the effects of wind on uniform cylinders using several models representing a range of shapes (octagonal, dodecagonal and hexdecagonal cross section), model orientations, and corner radii based on Reynolds number (Re) between 2.0×10^5 and 2.0×10^6. Balasubramanian et al. [64] carried out experiments to investigate the effects of axial taper of a circular cylinder. Further, vortex shedding from a finite circular cylinder was studied by Sumner et al. [65] using a hot-wire anemometer. Park and Lee [66] investigated the free end effect on the near wake of a finite circular cylinder in a cross flow.

Lift and drag coefficients for an octagonal cylinder was developed by Scanlan [39]. Figure 2-10 [39] depicts the lift and drag coefficients for an octagonal post structure having a variety of wind angles of attack. As shown in the figure, the slope of mean drag coefficient (C_D) is near zero and the slopes of the mean lift coefficient (C_L) with angle of attack were calculated to be approximately $-1.7 \cdot \pi$ and $0.45 \cdot \pi$ for flat and corner orientation, respectively.

Gabbai and Benaroya [67] reviewed the literature on the mathematical models used to investigate vortex-induced vibration of circular cylinders. Barhoush [68] discussed several numerical and empirical modeling efforts for vortex-induced vibration and the author applied Scanlan's model of vortex-shedding response for a long span bridge. The characteristics of the fluctuating lift forces were developed by Sakamoto [69] when a circular cylinder vibrates in the cross-flow direction. Wind tunnel tests on a circular cylinder were conducted by Gupta and Sarkar [70] to identify vortex-induced response parameters in the time domain. Diana et al. [71] performed buffeting response testing of a bridge deck in order to measure a complex aerodynamic admittance function. In addition, Scanlan and co-workers [72 to 76] studied various aspects for vortex-induced vibration. The authors analyzed an analytical model with linear/nonlinear aerodynamic damping and linear parametric coupling and compared the results with experimental wind tunnel data.

2.4.2. Full-Scale Measurements

Numerous full-scale measurements have been conducted to investigate the wind-induced loads and vibrations for tall buildings [77 and 78], stacks or chimneys [79, 80, and 81], towers or poles [73, 74, and 75], bridges or cable-stays, etc. Li et al. [77 and 78] conducted both full-scale measurements and wind tunnel tests to determine the spectral model of across-wind forces on tall rectangular buildings. The researchers evaluated the wind-induced along-wind and across-wind acceleration responses based on an established dynamic analysis model and an empirical model for the across-wind force spectra. From those measurements and tests, a proposed method as an alternative approach was evaluated for the across-wind response of rectangular buildings.

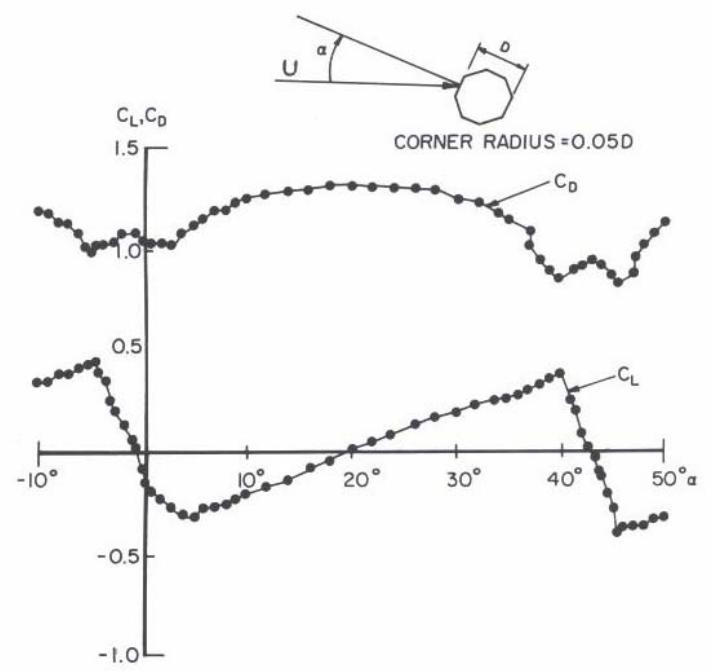

Figure 2-10. Force coefficients on an octagonal cylinder (Re = 1.2 × 10^6)

In order to verify the mathematical model for predicting vortex-induced vibrations of chimneys, several full-scale measurements on chimneys have been made by Ruscheweyh and Galemann [79], and the authors found that the predicted values are close to the measured values.

Ruscheweyh [80] presented the amplitude caused by cross-wind vibrations from long-term full-scale testing of four steel stacks. With the collected behavior data, fatigue calculations were made based on the Eurocode and were compared with the constant amplitude method. Tranvik and Alpsten [81] investigated the structural behavior of a 90 m high steel chimney and summarized the results collected from approximately four years of continuous measurements and regular observations of the chimney. The obtained data have some general relevance with respect to wind data, behavior of a slender structure under wind loading, and the effects of a mechanical damper. Also included in the report are the results from some theoretical studies related to the investigation of the chimney.

Miyashita et al., [82] showed that the effects of a tuned active damper upon wind-induced vibrations of the Hamamatsu ACT Tower and its structural characteristics are clear. Structural damping of steel lighting towers has been estimated through full scale experiments by Pagnini and Solari [83]. All the results concerning the first vibration mode point out the dependence of damping on motion amplitude and on stress, confirming the theoretical tendencies related to damping in ductile materials and friction joints. In order to determine the wind-induced fatigue loading, Robertson et al. [84] performed forced vibrations tests and made extensive observations. In the report, selected records were analyzed to obtain stress cycle counts. Mean drag coefficients were also derived form the strain data to investigate the impact of Reynolds number.

3. FIELD MONITORING

To collect the upstream wind and pole structural response characteristics, a long-term monitoring system was designed and sensors were installed on high mast luminary support structures in a known "high-wind" location in Northern Iowa. The collected data serve as the basis for much of the work presented subsequently.

3.1. Test Problem

Two weathering steel HMLPs (referred to as Pole 1 and Pole 2) located in open terrain, at the I35/US18 interchange near Mason City (see Figs. 3-1 [85] and 3-2), were monitored from the middle of October, 2004, to the beginning of January, 2006.

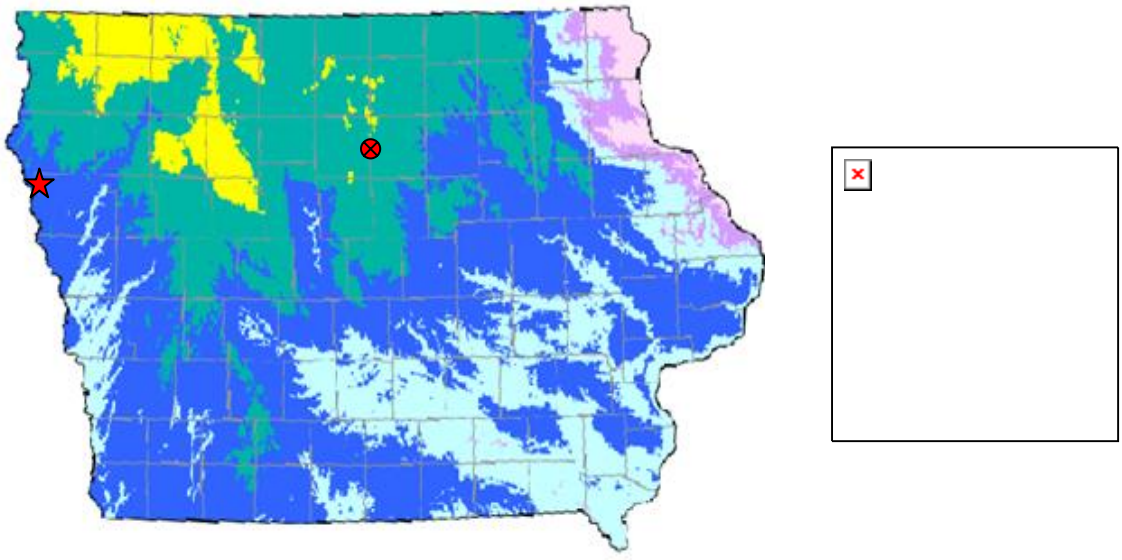

Near Sioux City:
Location where one HMLP collapsed in 2003

Near Mason City:
Location where field monitoring was performed

Note: Typical average wind speeds on well exposed sites at 50-m above ground. This map was generated from data collected by the Iowa Wind Energy Institute under the Iowa Energy Center. < http://www.energy.iastate.edu/renewable/wind/images/windmap-iowa_annual.gif >

Figure 3-1. Iowa estimated average annual speeds

(a) Pole 1

(b) Pole 2

Figure 3-2. Two monitored high mast light poles

3.1.1. HMLP Specification

The HMLPs were erected for service in 1999. Each HMLP monitored as part of this study consist of three discrete sections with "pole type" luminaries on the top; each section has a different, but constant thickness of: 0.313 in., 0.250 in., and 0.219 in., respectively, from bottom to top. The poles are 148 ft tall and each of the three sections has approximately the same length and taper ratio of approximately 0.14 in./ft. The poles are fixed into a concrete pad with a base-plate and six 2.25 in. diameter anchor bolts with a dodecagonal (12-sided) cylindrical cross section with a diameter (flat-side to flat-side distance) of 28.5 in. at the base and 8.77 in. at the top. Each HMLP also has an access port for electrical system maintenance. Detailed information is given in Table 3-1.

Table 3-1. Structural dimension of HMLPs

Segment	Base Diameter			Top Diameter			Thickness	Length	Taper Ratio
No.	Outer, in.	Center, in.	Inner, in.	Outer, in.	Center, in.	Inner, in.	in.	ft	in./ft
1	28.50	28.19	27.87	21.46	21.15	20.83	0.313	50.26	0.14
2	22.50	22.25	22.00	15.13	14.88	14.63	0.250	52.59	0.14
3	16.00	15.78	15.56	8.77	8.55	8.33	0.219	51.67	0.14

3.1.2. General Setup of the Monitoring System

Figure 3-3 shows the general setup of the long-term monitoring system. The system includes data acquisition equipment, strain sensors, accelerometers, anemometers, and video equipment. The data collected with this system were transmitted through a satellite-based internet connection to the Bridge Engineering Center at Iowa State University for interpretation and

analysis. Pole 1 was uncracked and had not been retrofitted prior to field monitoring and this pole was used to collect pole response data (using strain sensors and accelerometers). A temporary wooden power pole that was located near Pole 1 had a propeller vane anemometer installed on its top to collect wind speed and wind direction data at 33 ft.

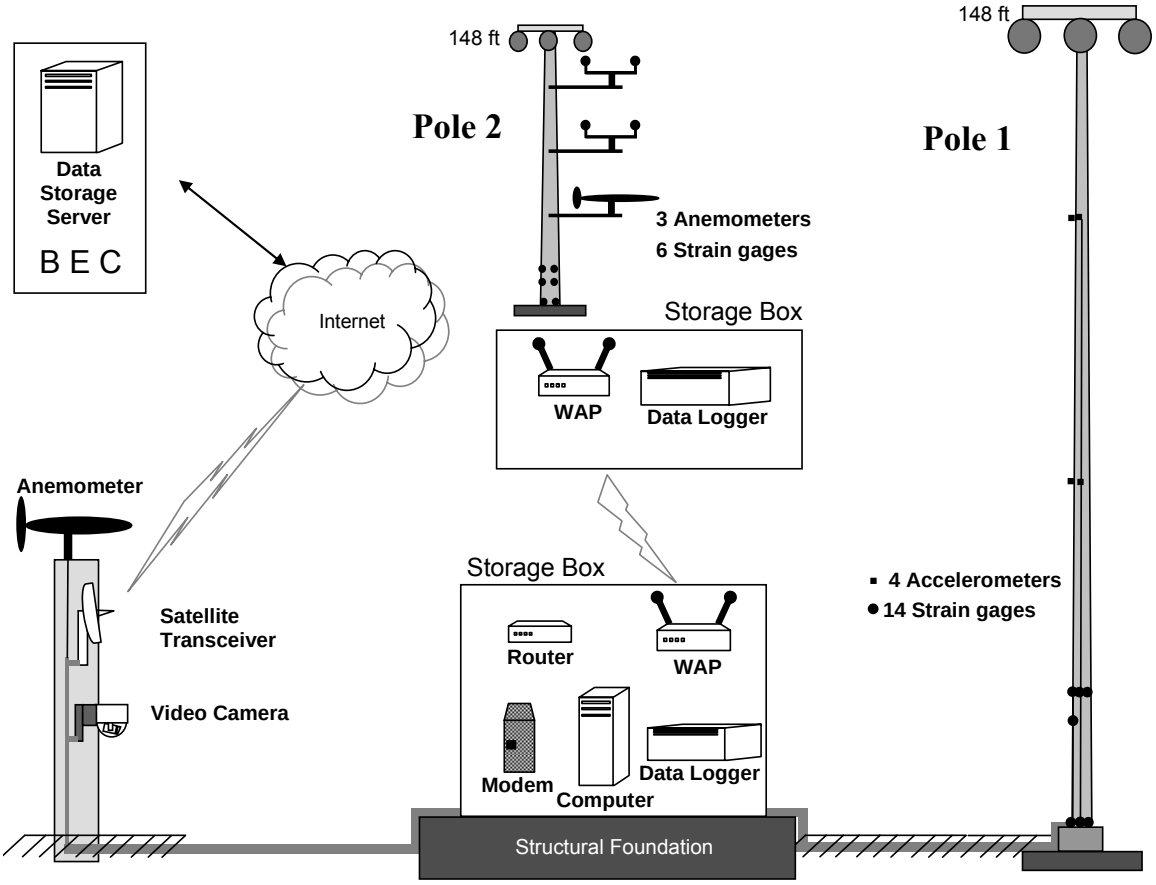

Figure 3-3. General setup of the long-term monitoring system

Pole 2, located approximately 2 miles to the South of Pole 1, had been retrofit with a steel splice jacket at the base with a thickness of 1.5 in. and a height of 5.25 ft. and this pole was used to collect detailed wind profile information. Wireless communication equipment was used to transmit data from both poles through the same satellite internet connection.

3.1.3. Instrumentation

Table 3-2 and Figures 3-4 and 3-5 summarize the locations of all the sensors installed on Pole 1 while Table 3-3 and Figures 3-6 and 3-7 summarize the locations of all the sensors installed on Pole 2. There were a total of 20 channels of data collected at Pole 1: 14 strain gages, 4 accelerometers, wind speed and direction at 33 ft and a total of 10 channels of data collected at Pole 2: 6 strain gages, wind speed at three different elevations and wind direction at 33 ft. Monitoring of the poles was conducted from the middle of October, 2004 and continued for approximately 15 months.

Table 3-2. Instrumentation locations for Pole 1

Side Number	Direction	Strain gage designation		Accelerometer designation	
		at 3 in. above base	at 5.75 ft above base	at 43.25 ft above base	at 120 ft above base
1	North	S8			
2	N+30˚	S6			
3	N+60˚	S4	S13		
4	East				
5	E+30˚				
6	E+60˚	S2	S14		
7	South				
8	S+30˚				
9	S+60˚	S3	S10	A4	A2
10	West	S5			
11	W+30˚	S7			
12	W+60˚	S1	S12	A3	A1

Note:
Gage No. 9 was installed at 3.75 ft near the upper left side of the hand hole (see Fig. 3-5 (b))
Gage No. 11 was installed at the corner between side No. 1 and 12 (see Fig. 3-5(a))

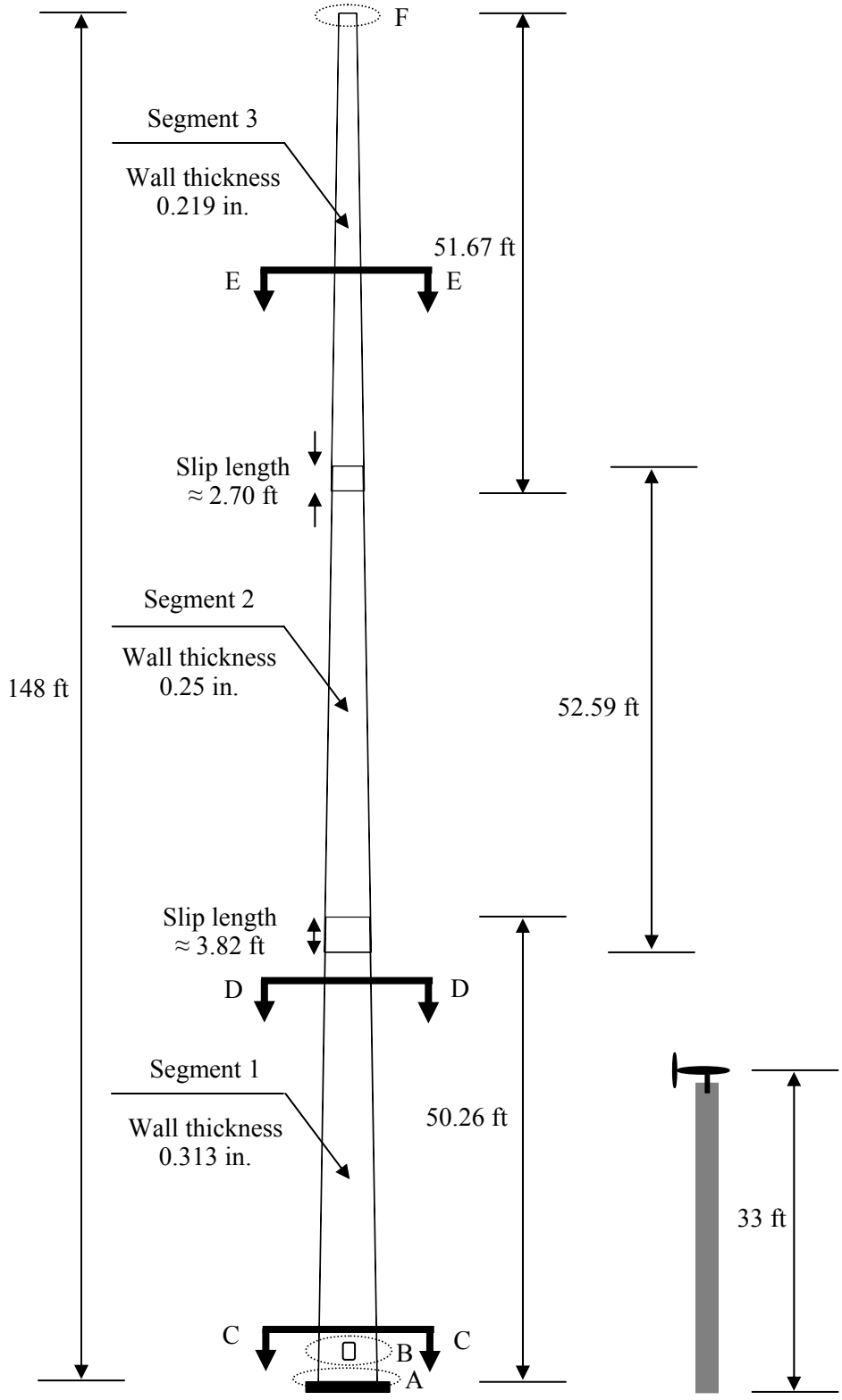

Figure 3-4. Elevation view of Pole 1

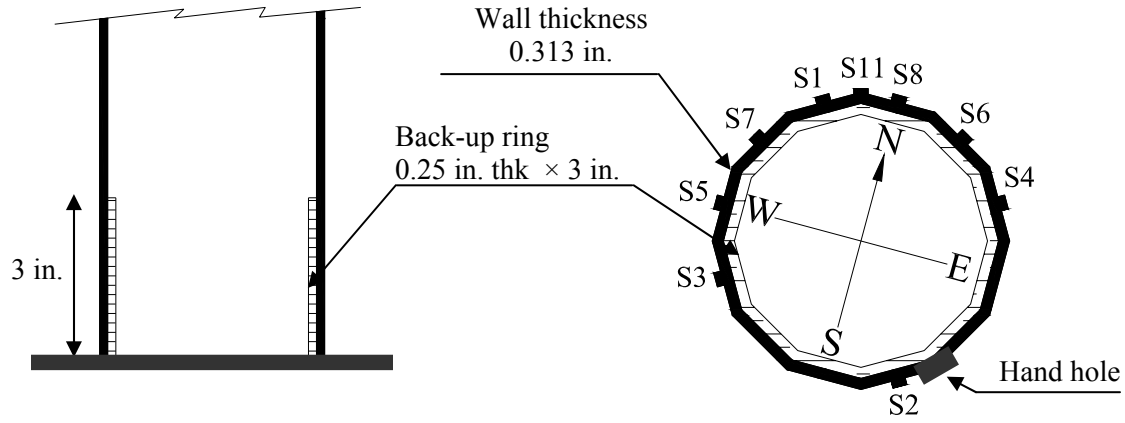

(a) Detail A: Pole base and cross section at 3 in. from base

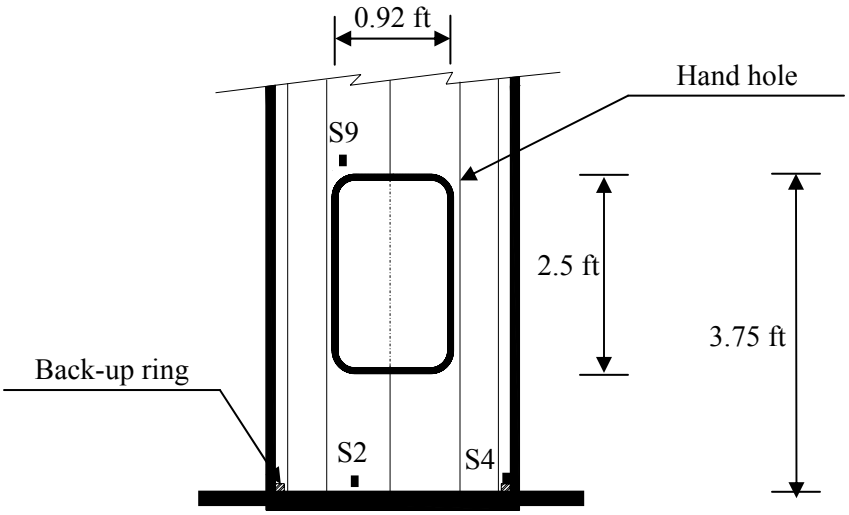

(b) Detail B: Hand hole

Figure 3-5. Detail description of Pole 1 (Refer Fig. 3-4)

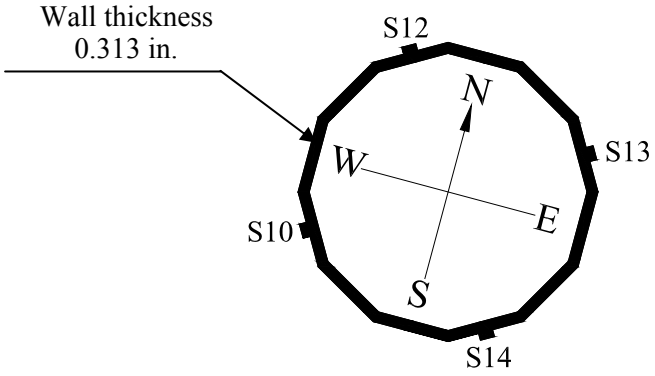

(c) Detail C: Cross section at 5.75 ft

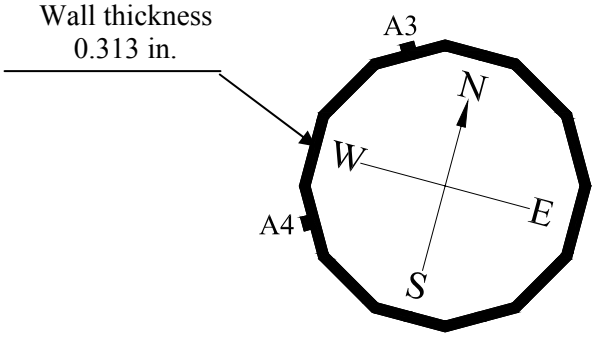

(d) Detail D: Cross section at 43.25 ft

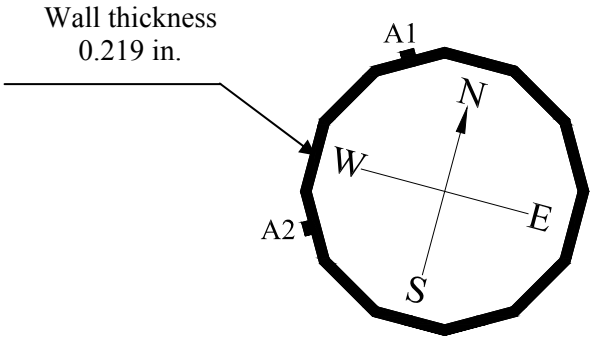

(e) Detail E: Cross section at 120 ft

Figure 3-5. (Continued)

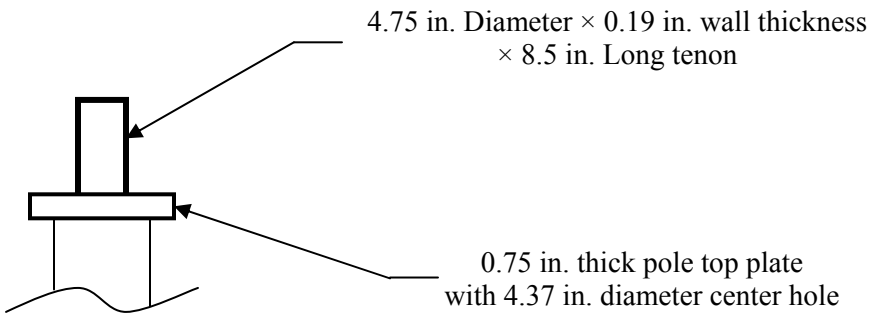

(f) Detail F: Pole top at 148 ft

Figure 3-5. (Continued)

Table 3-3. Instrumentation locations for Pole 2

Side Number	Direction	Strain Gage designation			Anemometer designation
		at 3 in. above base	at 4 ft above base	at 4.92 ft above base	
1	N+15˚				
2	N+45˚				
3	N+75˚				
4	E+15˚	1	3	5	
5	E+45˚				at 33 ft / 86.5 ft / 140 ft
6	E+75˚				
7	S+15˚				
8	S+45˚				
9	S+75˚	2	4	6	
10	W+15˚				
11	W+45˚				
12	W+75˚				

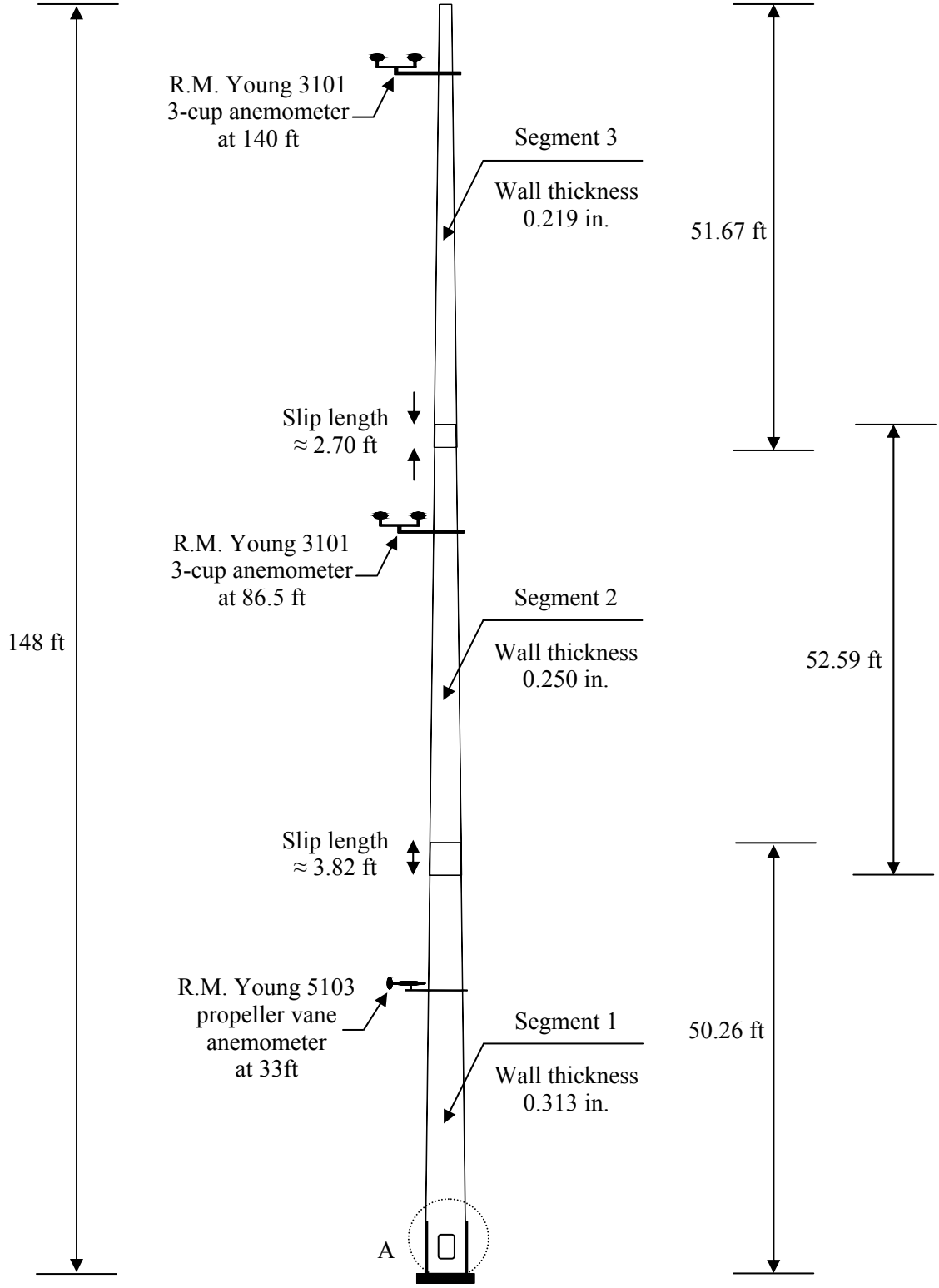

Figure 3-6. Elevation view of Pole 2

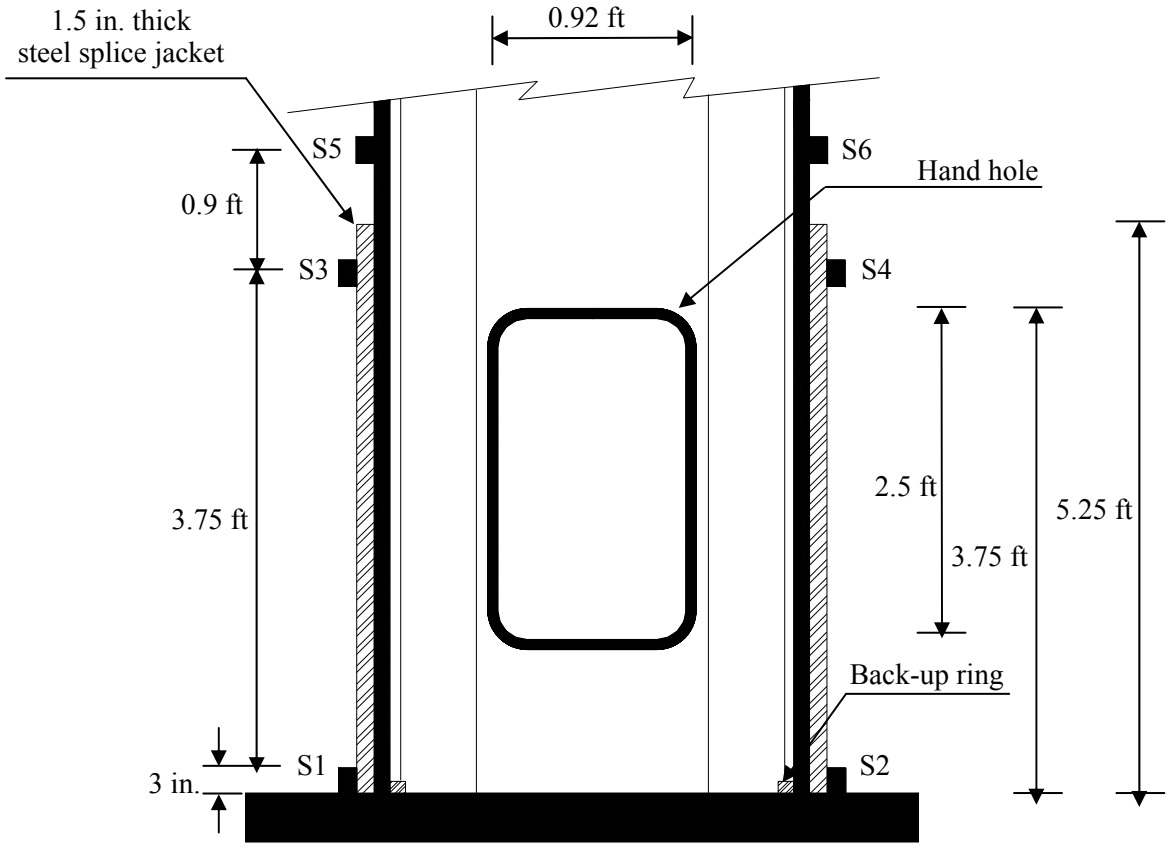

(a) Detail A: Hand hole

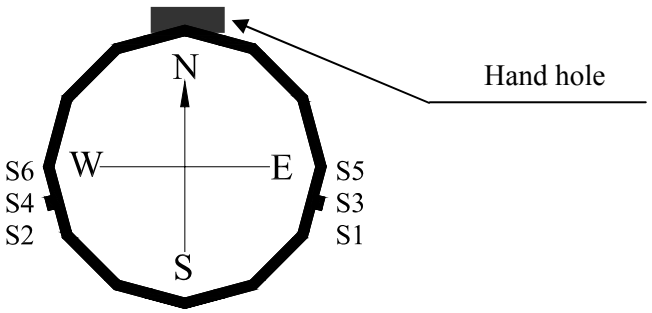

(b) Cross section at gage location

Figure 3-7. Detail description of Pole 2 (Refer Fig. 3-6)

Strain Gages

All strain gages (Model LWK-06-W250B-350) had a uniaxial gage length of 0.25 in. and were protected with a multi-layer weather proofing system and then sealed with a silicon type compound. Figures 3-8 shows the view of the strain gages installed at the HMLPs.

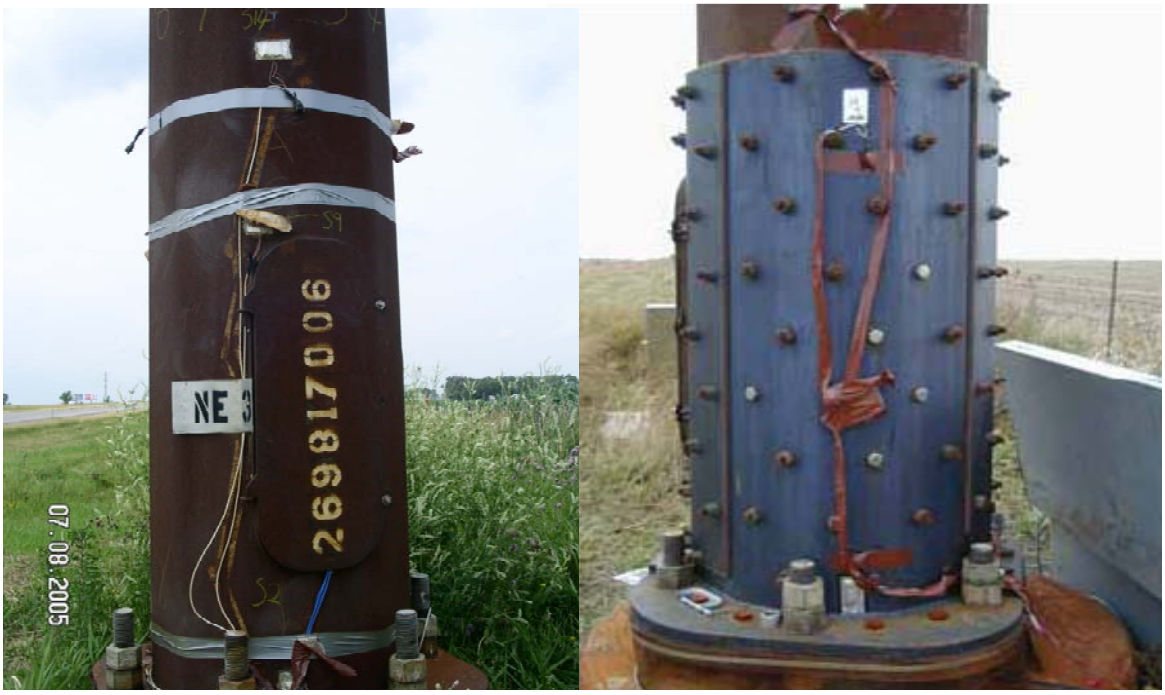

(a) Pole 1 (b) Pole 2

Figure 3-8. View of strain gages installed at Pole 1 and Pole 2

Accelerometers

At two elevations, two pairs of orthogonally oriented uniaxial accelerometers (Model 3701G3FA50G), were installed on the outside surface of Pole 1. Four accelerometers (a peak measurable acceleration of 50 g) were used on Pole 1. The selected accelerometers were specifically designed for measuring low-level, low-frequency accelerations, such as that found on a bridge or a HMLP. The locations of accelerometers installed on Pole 1 are described in Figs. 3-5 (d) and (e); Figure 3-9 shows temporary BDI strain sensors used during a short-term pluck test and the permanently installed accelerometers on Pole 1.

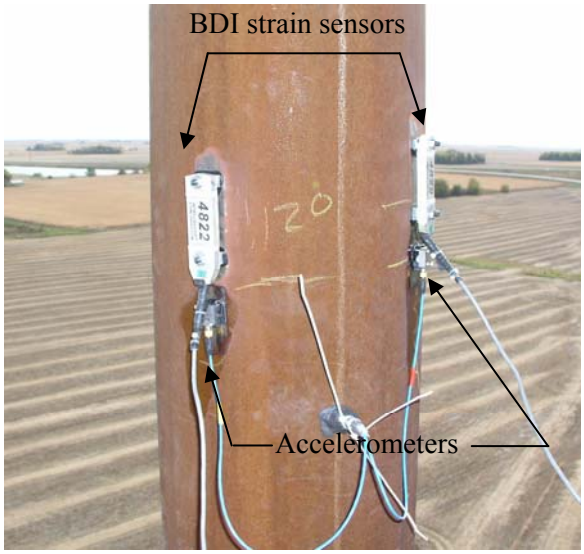

Figure 3-9. Temporary BDI gages and accelerometers on Pole 1

Anemometers

Wind speed and direction measurements were recorded atop a 33 ft tall temporary wooden pole directly adjacent to Pole 1 using a propeller vane anemometer (see Figs. 3-4 and 3-10). In addition, wind speed records were also obtained using 3-cup anemometers (Young Model 3101) at 140 ft as well as at 86.5 ft and a propeller vane anemometer (Young Model 5103) at 33 ft, on Pole 2. The anemometer locations at Pole 2 are shown in Figs 3-6 and 3-11 [86].

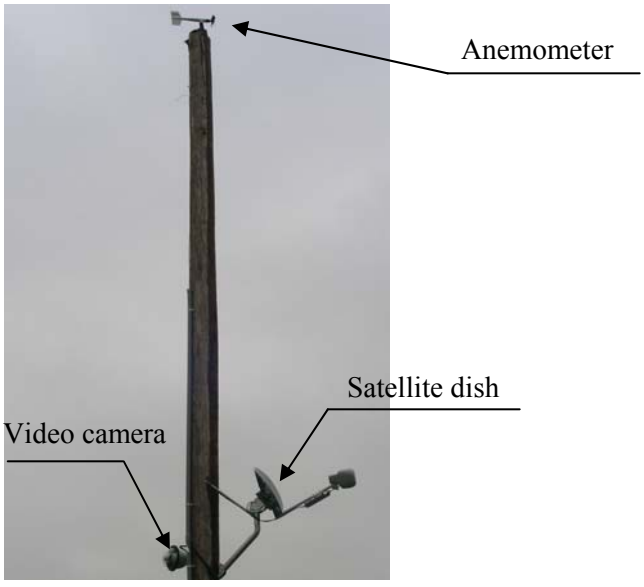

Figure 3-10. Anemometer, satellite dish and camera installed at temporary pole near Pole 1

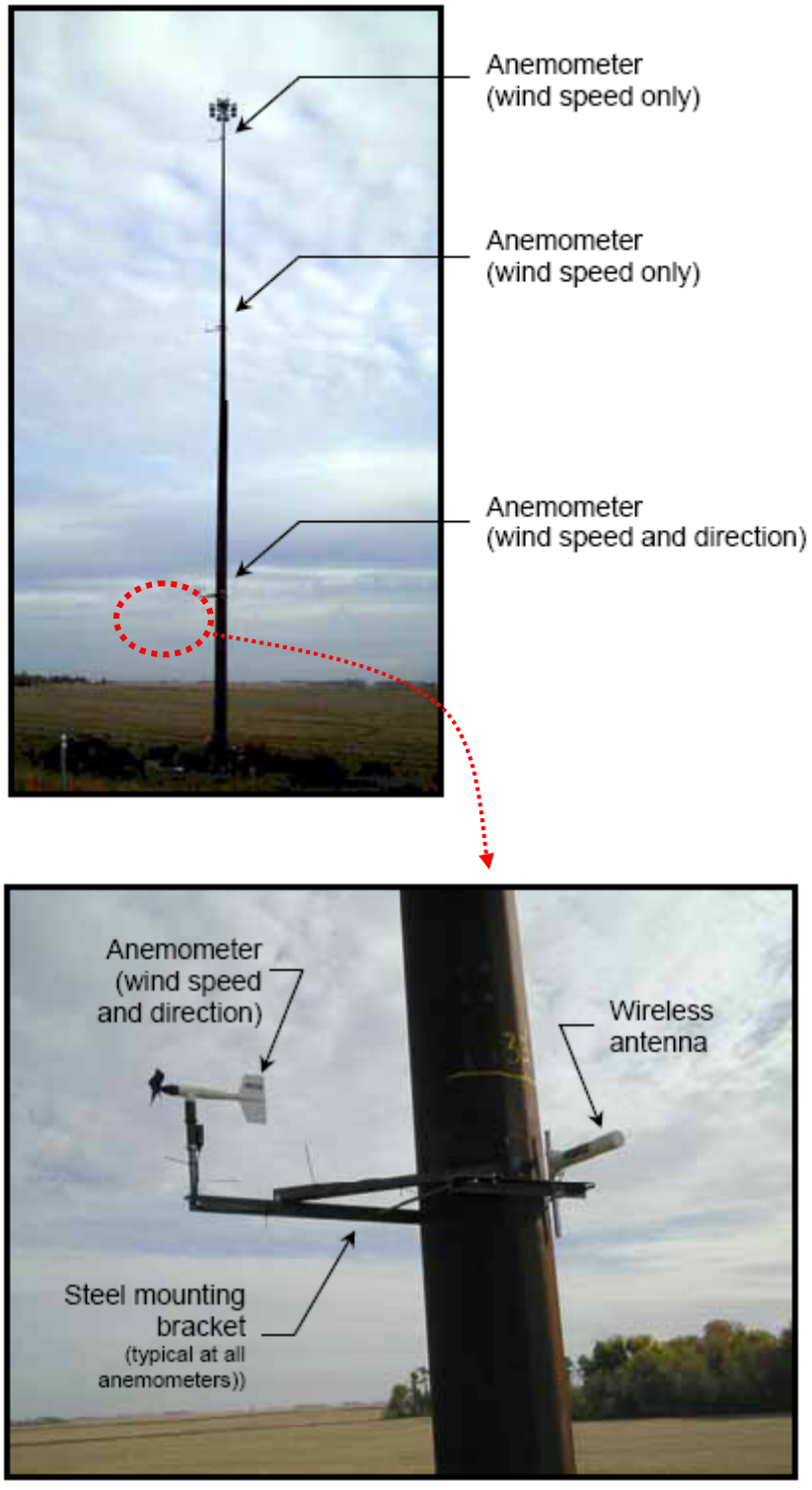

Figure 3-11. Anemometer installed at Pole 2

Camera

A remote monitoring video camera (see Figs. 3-3, 3-4 and 3-10) was installed to record the Pole 1 vibrations. The camera (model SNCRZ30N) has a variety of functionality with Pan/Tilt/Zoom (PTZ) capacity. By simply using a popular web browser, images and the PTZ movement of the camera could be controlled using a PC.

3.1.4. Data-Logger System

A data-logger system was located at each pole to store the data. One-minute duration strain and acceleration records were stored when the wind velocity was between specific ranges. 3-minute (1-minute for Pole 2) mean wind speed and direction information were recorded continuously and rain-flow information for six selected strain gages were also recorded every 10-minutes.

3.1.5. Data Development Approach

A Campbell Scientific CR9000 data logger (see Fig. 3-12), which is a high speed and multi-channel 16-bit data acquisition system (a sampling rate of 50 Hz) was used for the collection of data at Pole 1. The logger was configured with digital and analog filters to assure noise-free signals. A Campbell Scientific CR5000 data logger (see Fig. 3-13 [86]), which is also a high speed and multi-channel 16-bit data acquisition system (a sampling rate of 50 Hz), was used for the collection of data from Pole 2; however the CR5000 does not have on-board digital and analog filtering.

After data were received at the Bridge Engineering Center, several data processing steps were completed to: check acceleration values, validate the stress record, monitor the general pole behavior, develop general wind information and count the number of induced stress cycles (see Fig. 3-3). The data from the anemometers were also used to parse the data and to determine the most dominant wind velocity at a given time and to evaluate the associated stress level induced. The acceleration and strain gage data were also specifically used to check for the occurrence of vortex shedding. Fast Fourier Transform (FFT) analysis was also performed to obtain vibrations frequencies at specific wind velocities.

3.2. Results

This section summarizes the results from pluck tests and long-term monitoring for the described HMLPs. The pluck tests were conduced before the long-term monitoring was performed and the long-term monitoring lasted for approximately 15 months.

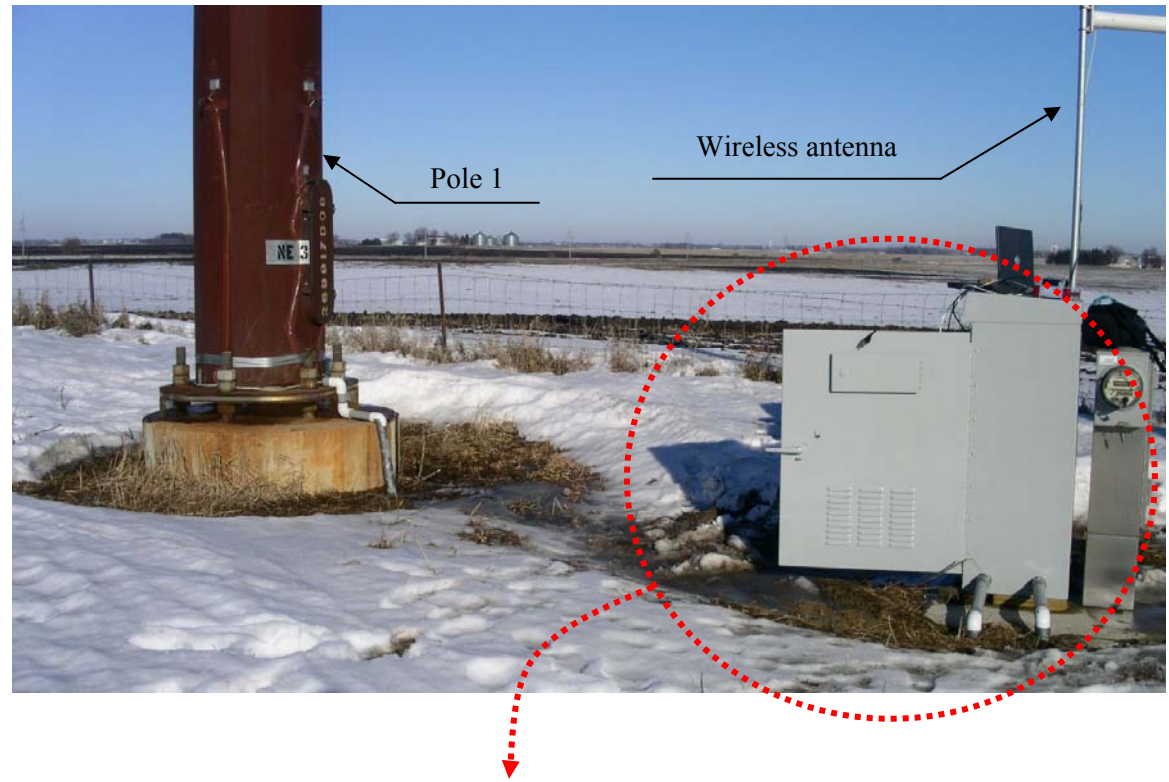

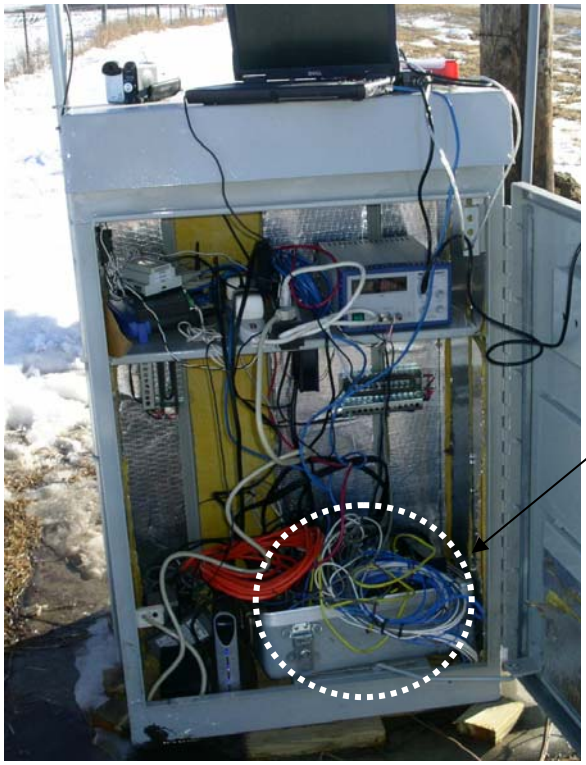

Figure 3-12. Data acquisition system at Pole 1

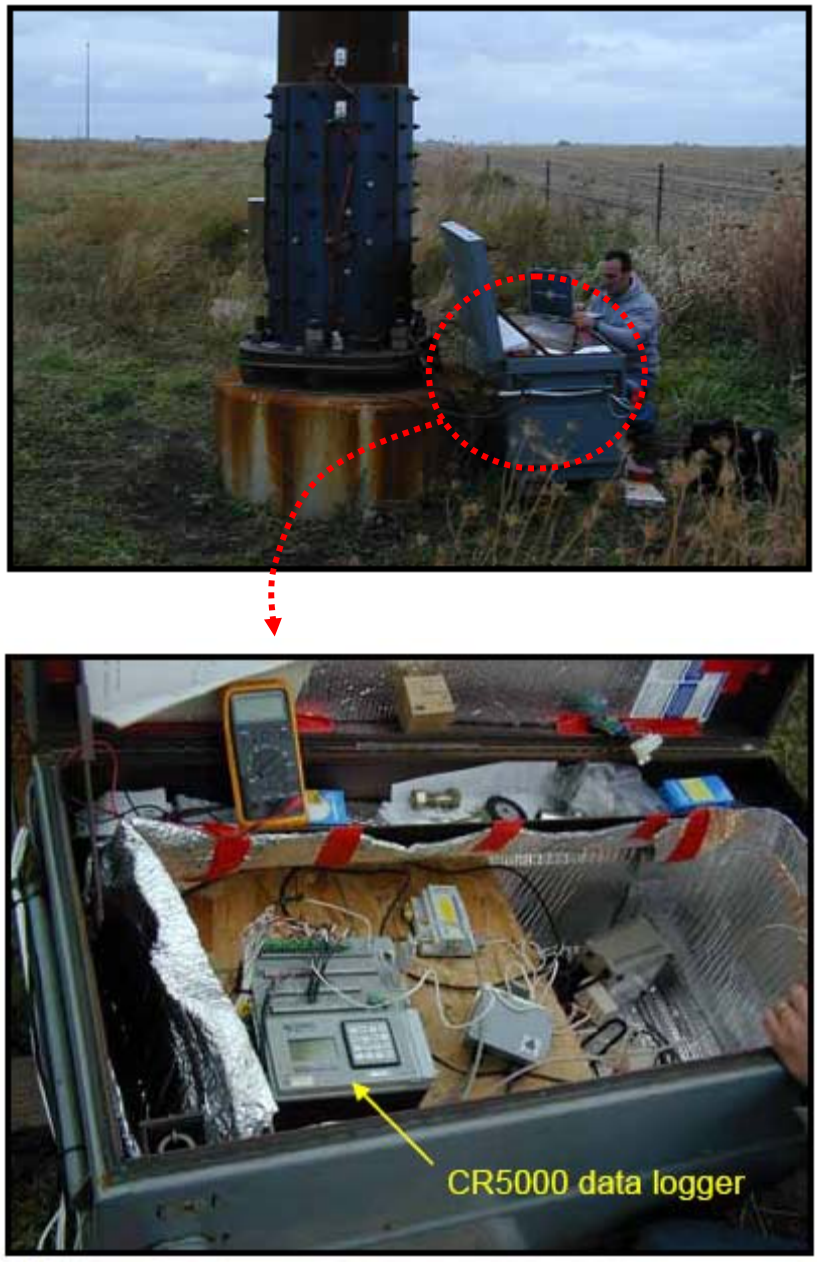

Figure 3-13. Data acquisition system at Pole 2

3.2.1. Pluck-Test

The natural frequencies and damping characteristics of the subject HMLP were determined from "pluck" tests. Pluck tests (see Fig. 3-14) were performed by pulling and releasing a cable attached to the pole shaft and a stationary object. The cable was attached to the shaft at a suitable height in order to realize appropriate oscillations, and the force level was controlled to induce large deformation states, bearable by the structure, and suitable to excite the investigated vibration modes.

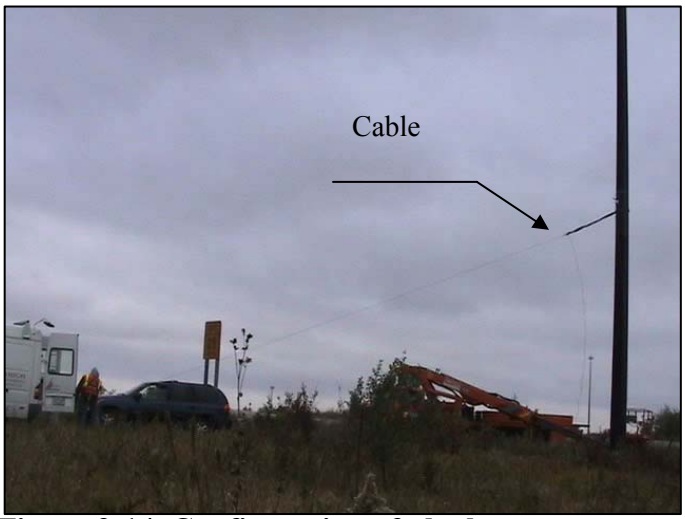

Figure 3-14. Configuration of pluck test

FFT analyses (see Fig. 3-15) were performed with the strain and the acceleration data to obtain the first four vibrations frequencies for Pole 1 as: $f_1 = 0.3$ Hz, $f_2 = 1.3$ Hz, $f_3 = 3.3$ Hz, and $f_4 = 6.4$ Hz. The first four damping ratios of the pole, on average, were also determined as: $\zeta_1 = 0.60\%$, $\zeta_2 = 0.17\%$, $\zeta_3 = 0.27\%$ and $\zeta_4 = 0.30\%$ [86]. Note that In the 2001 AASHTO Specification, a "conservative" damping ratio of 0.50% is specified.

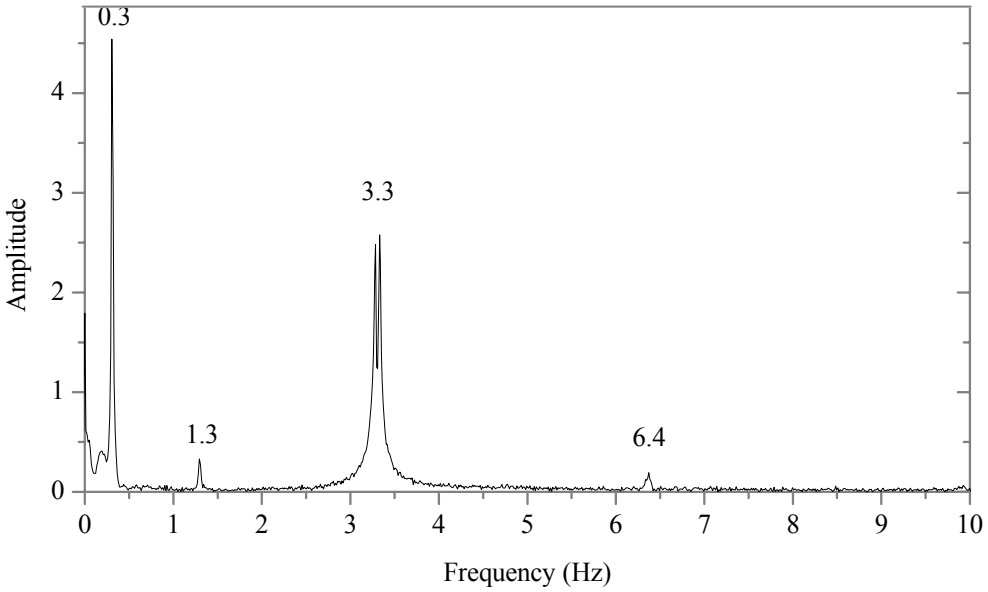

Figure 3-15. Sample of FFT

Finite Element Analysis (FEA) using commercially available software, ANSYS [87], was performed to compare with the results of the FFT analysis. Pole 1 was modeled using a series of tapered elements (Beam 54) each 1 foot in length with the base fixed from all translations and rotations. Element Mass 21 was used to represent the luminary located at the top of the pole. As

Table 3-4 shows, the natural frequencies from field tests are in good agreement with the results from FEA. Also, the mode shapes for the first four modes were obtained from the FEA (see Fig. 3-16).

Table 3-4. Modal frequency and damping ratio

Mode	FEA	FFT	Difference	Damping ratio [86]
1	0.338	0.305	10.82%	0.60%
2	1.337	1.294	3.32%	0.17%
3	3.407	3.333	2.22%	0.27%
4	6.702	6.396	4.78%	0.30%

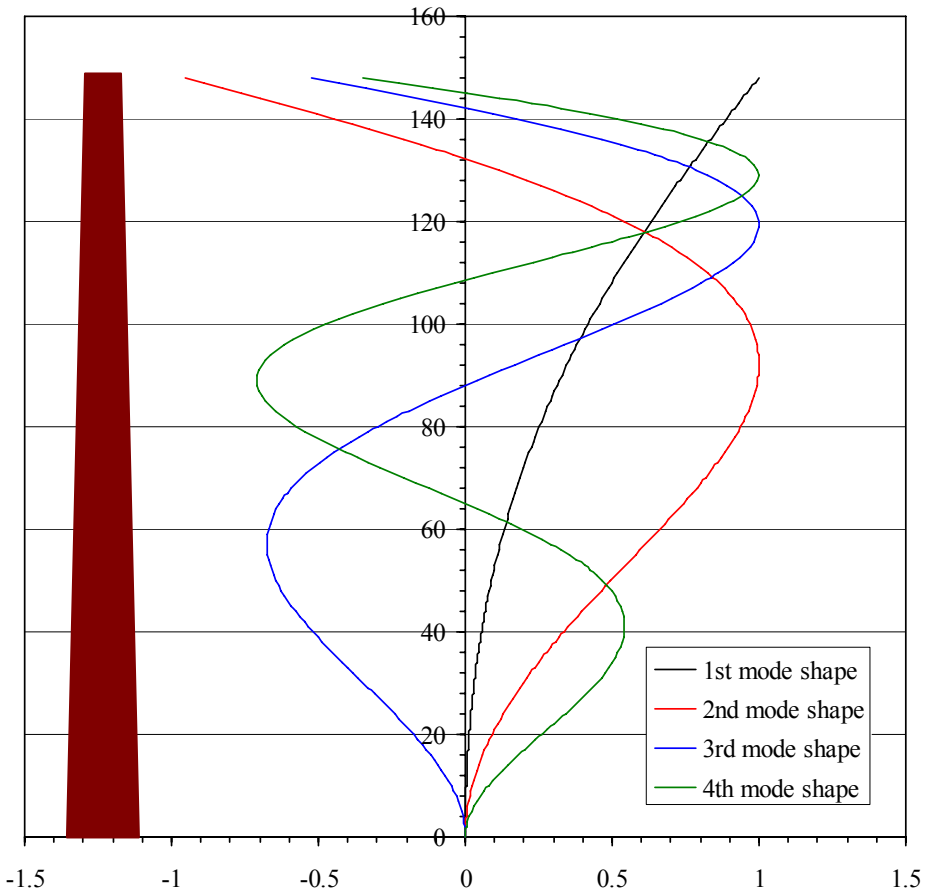

Figure 3-16. HMLP mode shapes

Figure 3-17 shows experimentally determined damping ratio versus frequency for poles tested by Connor and Hodgson [86]. The damping ratio in the first mode is considerably higher than the other modes. The damping ratios in first four modes are considerably lower than the values given in the AASHTO (0.50%) and CAN/CSA (0.75%) specifications.

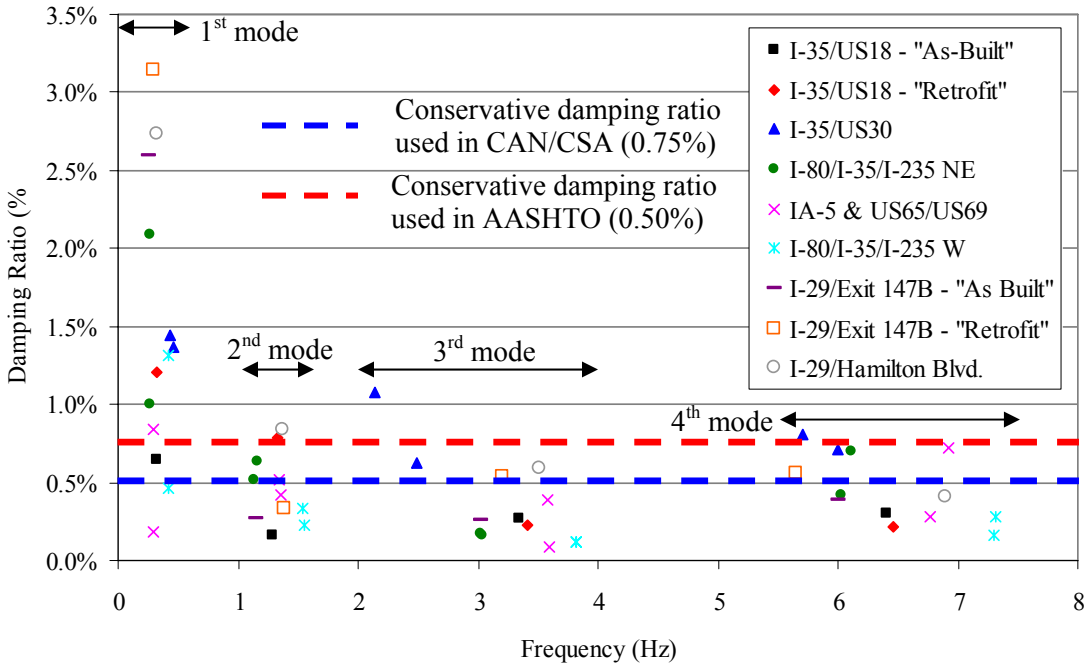

Figure 3-17. Damping ratio vs. frequency

3.2.2. Long-Term Monitoring

The results of the long-term monitoring are essential to formulate a mathematical model for predicting aerodynamic loads, which will be described subsequently. As discussed previously, two HMLPs located at the interchange between I35 and US18 near Mason City, Iowa were monitored for approximately 15 months. The resulting data are summarized as follows.

Frequency of wind speed and direction

Average wind data were recorded continuously at each HMLP; on a three-minute interval at Pole 1 and on a one-minute interval at Pole 2. During each interval, the data logger recorded the average and maximum wind speed as well as the average wind speed. Based on these data, dominant wind direction and speed could be obtained.

Table 3-5 and Fig. 3-18 describe the frequencies of three-minute mean wind speeds and directions recorded at Pole 1. The frequencies of one-minute mean wind speeds and direction recorded at Pole 2 are also shown in Table 3-6 and Fig. 3-19.

Table 3-5. Frequencies of three-minute mean wind speed and direction measured at Pole 1

Spd, mph		Wind Direction Designation																	
Min	Max	N	NNE	NE	ENE	E	ESE	SE	SSE	S	SSW	SW	WSE	W	WNW	NW	NNW	Sum	%
0	5	1530	1400	1605	1925	2141	1263	633	1872	2073	1903	1792	2169	2536	2727	2015	1514	29098	19.2
5	10	2886	2500	2258	2316	3249	1455	1372	9224	5968	3798	2463	4015	4472	5805	6349	3455	61585	40.6
10	15	1668	1090	773	1146	1638	628	1146	6381	4209	2746	2058	1450	1835	3073	5741	2606	38188	25.2
15	20	888	619	374	513	1214	307	519	2322	1169	1054	727	443	408	1348	3236	1431	16572	10.9
20	25	231	193	131	82	289	103	89	547	208	178	223	173	97	246	1583	433	4806	3.2
25	30	45	4	9	20	42	11	8	62	10	20	48	64	11	55	603	30	1042	0.7
30	35	2	2	2	1	4	7	0	8	0	1	23	22	1	3	177	3	256	0.2
35	40	0	1	0	0	2	0	0	0	0	0	1	0	0	0	30	0	34	0.0
40	45	0	0	0	0	0	0	0	0	0	0	0	0	0	0	0	0	0	0.0
45	50	0	0	0	0	0	0	0	0	0	0	0	0	0	0	0	0	0	0.0
50	100	0	0	0	0	0	0	0	0	0	0	0	0	0	0	0	0	0	0.0
Sum		7250	5809	5152	6003	8579	3774	3767	20416	13637	9700	7335	8336	9360	13257	19734	9472	151581	100
%		4.8	3.8	3.4	4.0	5.7	2.5	2.5	13.5	9.0	6.4	4.8	5.5	6.2	8.7	13.0	6.2	100	

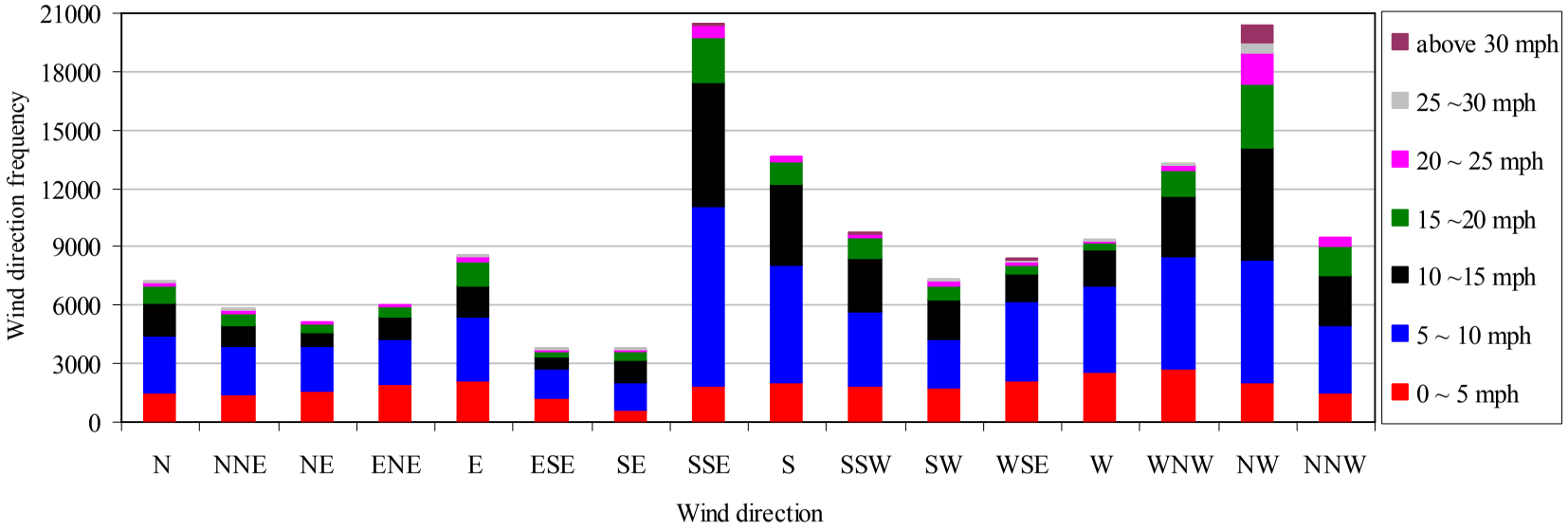

Figure 3-18. Frequencies of three-minute mean wind speed and direction measured at Pole 1

Table 3-6. Frequencies of three-minute mean wind speed and direction measured at Pole 2

Spd, mph		Wind Direction Designation																	
Min	Max	N	NNE	NE	ENE	E	ESE	SE	SSE	S	SSW	SW	WSE	W	WNW	NW	NNW	Sum	%
0	5	450	229	32	106	202	323	321	233	288	316	309	560	240	188	372	401	4570	5.4
5	10	1133	712	15	433	374	706	886	934	1005	590	500	741	1127	791	1690	1521	13158	15.5
10	15	1584	914	15	948	817	707	1457	2472	2151	843	883	483	1361	1084	1933	2352	20004	23.6
15	20	1441	868	7	485	434	293	1239	3301	1782	1048	608	240	689	677	1165	2264	16541	19.5
20	25	901	536	0	193	222	408	752	2741	1556	495	380	43	373	309	1014	1968	11891	14.0
25	30	835	337	0	21	40	231	479	1647	1127	174	286	1	131	263	714	1658	7944	9.4
30	35	403	128	0	0	0	36	327	1118	494	78	100	0	54	316	808	1434	5296	6.2
35	40	136	28	0	0	0	1	62	541	170	17	48	0	35	136	625	975	2774	3.3
40	45	12	2	0	0	0	0	5	226	36	3	19	0	3	53	450	535	1344	1.6
45	50	0	0	0	0	0	0	0	50	8	0	3	0	0	15	364	263	703	0.8
50	100	0	0	0	0	0	0	0	1	2	0	0	0	0	2	336	198	539	0.6
Sum		6895	3754	69	2186	2089	2705	5528	13264	8619	3564	3136	2068	4013	3834	9471	13569	84764	100
%		8.1	4.4	0.1	2.6	2.5	3.2	6.5	15.6	10.2	4.2	3.7	2.4	4.7	4.5	11.2	16.0	100	

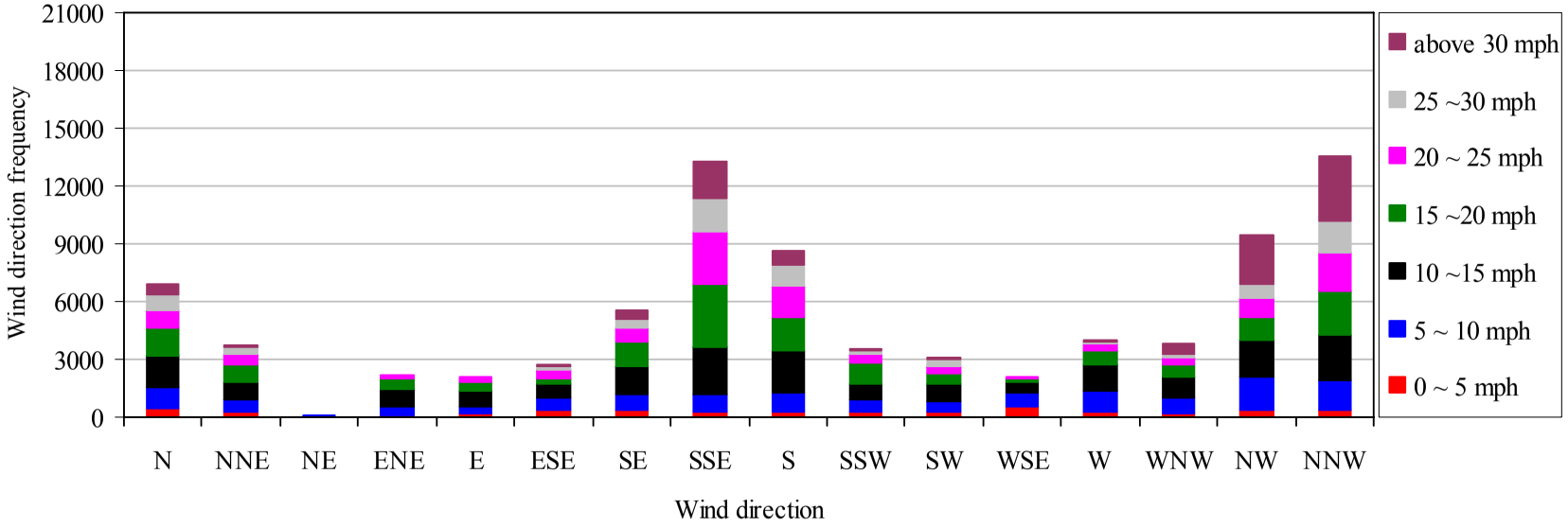

Figure 3-19. Frequencies of one-minute mean wind speed and direction measured at Pole 2

The NW (North-West), NNW (North-North-West) and SSE (South-South-East) wind directions were observed to be the most frequent directions and a wind speed below 15 mph was observed to be the most frequent wind speed range. Overall wind data were expressed using a wind-rose polar histogram for prevailing wind direction and magnitude of prevailing winds for both HMLPs. Figure 3-20 shows the percent occurrence of winds from all directions in polar form.

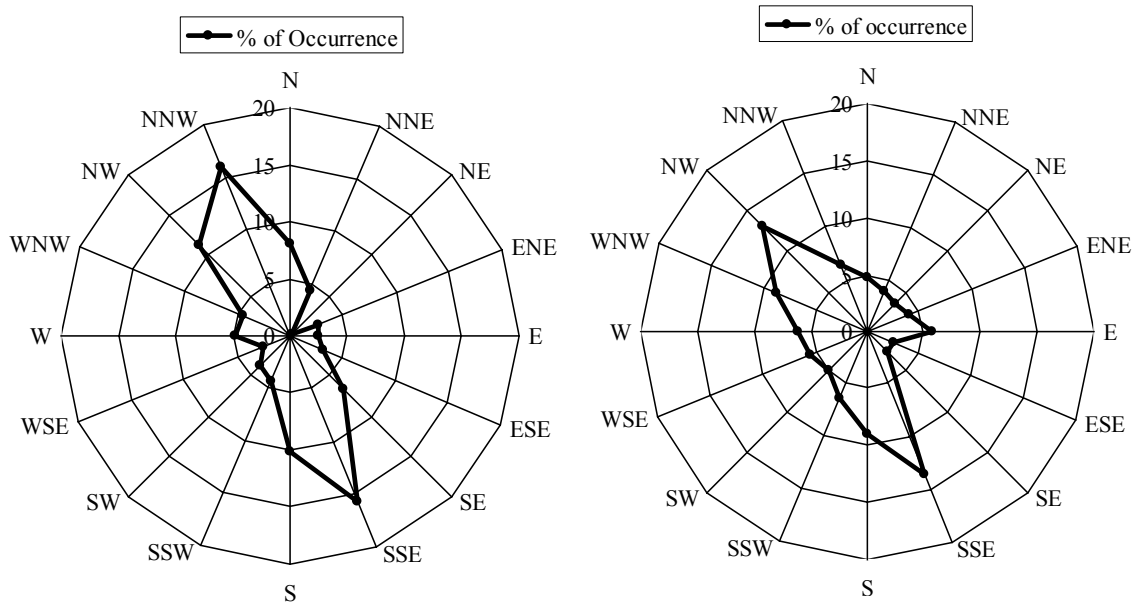

(a) Pole 1 (b) Pole 2

Figure 3-20. Percentage of wind direction occurrence

Probability density (see Fig. 3-21) shows that the winds speed between 5 mph and 8 mph are the most dominant wind speed range. Figure 3-22 (b) shows the cumulative probability density based on the data in Fig. 3-22 (a). In Fig. 3-22 (b), the three-minute mean wind speed less than 8 mph corresponds to a cumulative probability density of approximately 50% and three-minute mean wind speeds less than 16 mph correspond to a cumulative probability density of approximately 90%.

Wind profile parameters (Z_0, α and I)

As described previously, there were three anemometers mounted at Pole 2. However, the mid-height anemometer did not correctly operate and the data from the mid-anemometer data have been discarded herein. Using the wind speed data from Pole 2, the roughness length Z_0, which is the distance above ground level where the wind speed should be theoretically zero, can be determined. The terrain factor α, which is power-law exponent dependant on roughness, can also be obtained. The roughness length and the terrain factor can be computed using the log law (Eq. 3.1) and the power law (Eq. 3.2) [39], respectively.

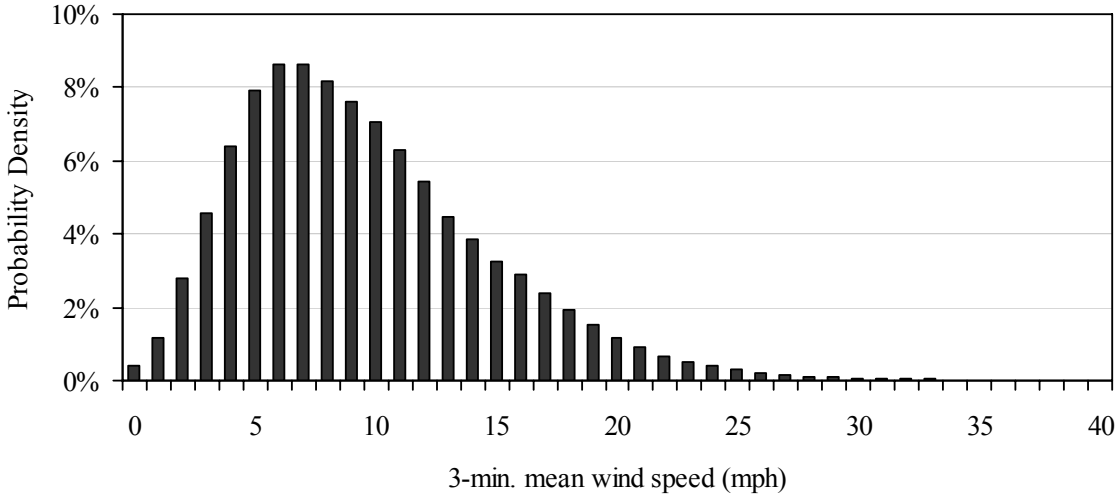

(a) Probability density

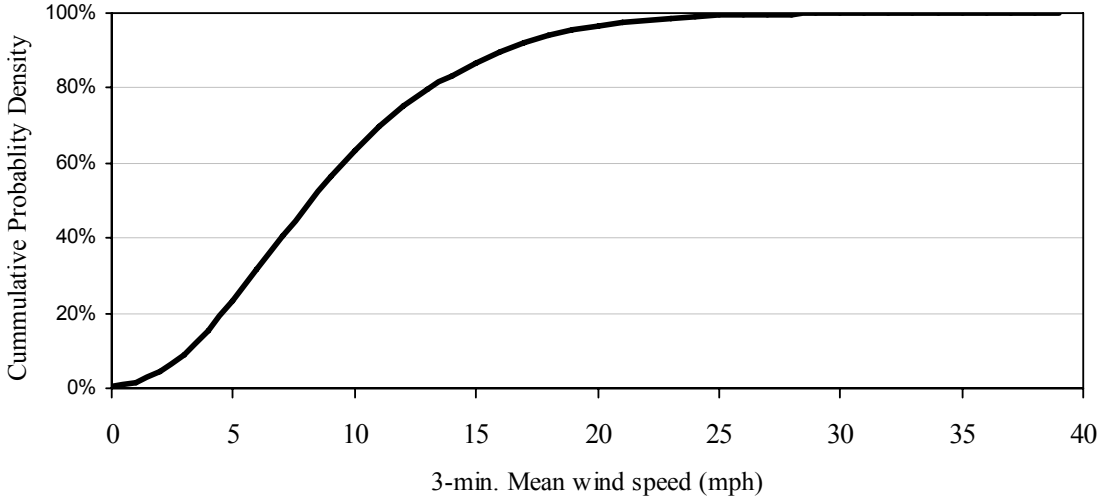

(b) Cumulative probability density

Figure 3-21. Wind speed density

$$U(z_g, z_0) = 2.5U_* \cdot \ln\frac{z_g}{z_0} = 2.5u_*(\ln z_g - \ln z_0) \qquad (3.1)$$

where, $U(Z_g, Z_0)$ = the mean wind speed at height of Z_g

Z_g = the height above Z_0

Z_0 = the roughness length

u_* = the shear friction velocity of the flow

$$\frac{U(z_1)}{U(z_2)} = \left(\frac{z_1}{z_2}\right)^{\alpha} \tag{3.2}$$

where, $U(Z_1)$ and $U(Z_2)$ = the mean wind speed at height Z_1 and Z_2, respectively

Z_1 and Z_2 = the heights above ground

According to previous research [36, 38, and 39], for "Open" terrain, the exponent α is typically between 0.12 and 0.15 and the roughness length is typically between 2 cm and 7 cm. The two poles are located in "Open" terrain and the roughness length and the terrain factor computed from Pole 2 are approximately 0.213 ft (6.5 cm) and 0.145, on average, at wind speeds of above 20 mph, respectively. These values are in general agreement with previous research (see Table 3-7).

Turbulence intensities, Eq. 3.3, for along-wind and across-wind directions can be also determined from the field data. Reference [88] shows the turbulence intensity at 33 ft is generally 20% in an open terrain and it decreases with height. The turbulence intensity at the HMLP was calculated to be approximately 14%, on average, above 20 mph wind speed (see Table 3-7).

$$I_{\bar{z}} = c \cdot \left(\frac{33}{\bar{z}}\right)^{1/6} \tag{3.3}$$

where, $I_{\bar{z}}$ = the intensity of turbulence at height $\bar{z}$

$\bar{z}$ = the equivalent height of the structure

c = exposure coefficient

Table 3-7. Wind parameters determined from long-term monitoring

Parameter	Field	Reference [39]
Z_0	0.213 ft (6.5 cm)	2 ~ 7 cm
α	0.145	0.12 ~ 0.15
I_u	14%	20%
I_w	14%	$0.8 \cdot I_u$

Along-wind response (buffeting induced vibration)

Figure 3-22 shows stress range distribution against one-minute mean wind speed for Pole 1 at a wind direction of S+60˚ (111 Deg., see Table 3-1) which is typical of all along-wind responses. As shown in the figure, the stress ranges above a wind speed of 10 mph for along direction seem to be generally proportional to the square of wind speed. Above the mean wind speed of 10 mph, the stress range at channel S12 in the cross direction shows similar magnitude to the stress range at channel S10, in the along direction. This indicates that the pole vibrated in both the along-wing and cross-wind directions. This behavior was also confirmed by the video equipment installed at the pole. The bi-directional vibrations could be the result of variable wind direction. Thus, steady increase of stress range with wind speeds in both the along-wind and across-wind directions showed the importance of buffeting loads in any dynamic analysis.

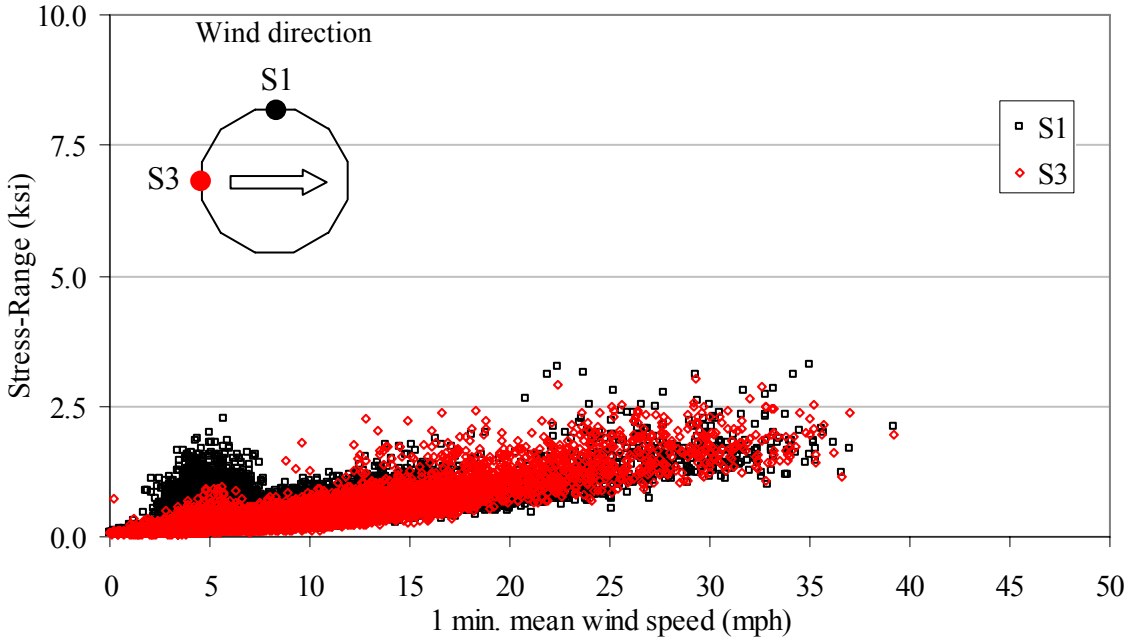

(a) Channels S1 and S3 at base

Figure 3-22. Stress range at wind direction of S+60 (111 Deg.) at Pole 1

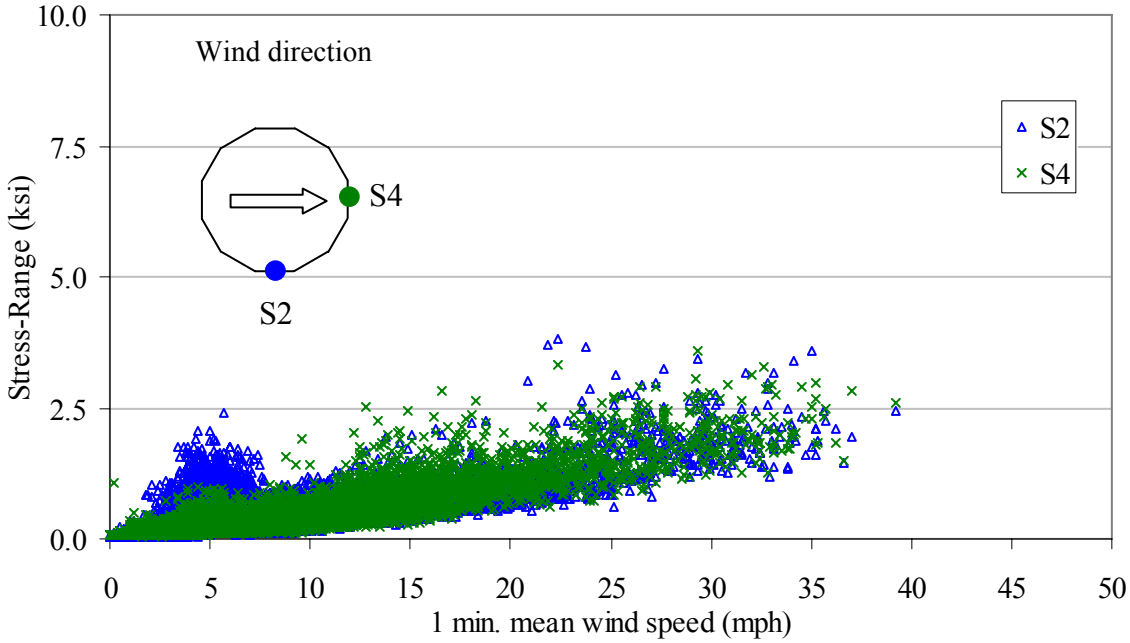

(b) Channels S2 and S4 at base

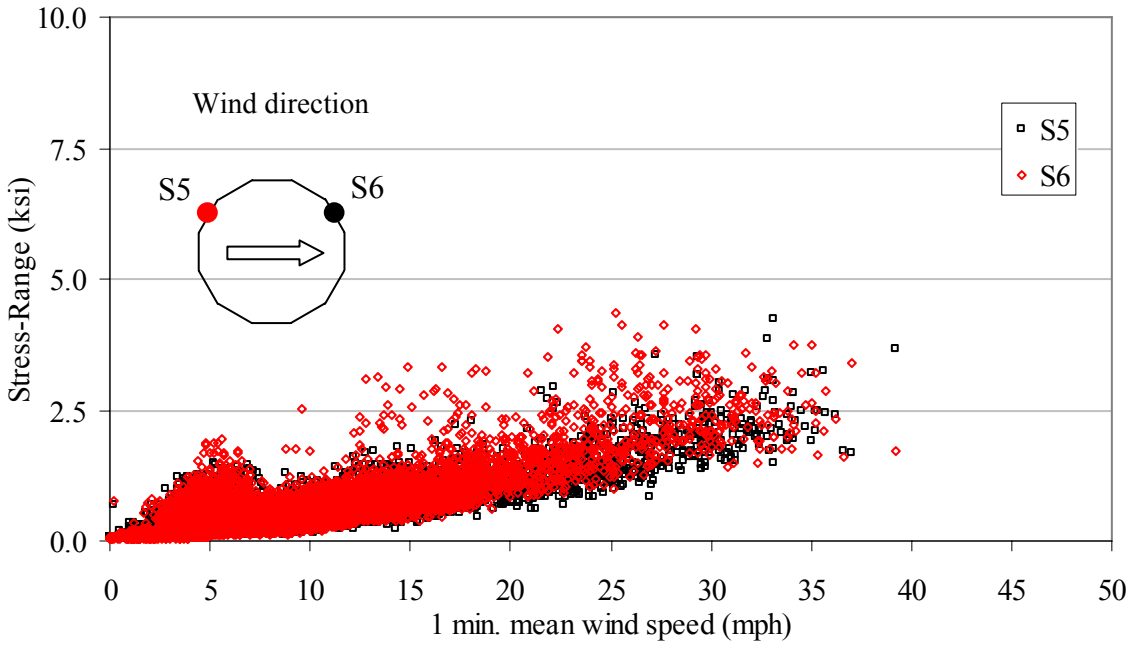

(c) Channels S5 and S6 at base

Figure 3-22. (Continued)

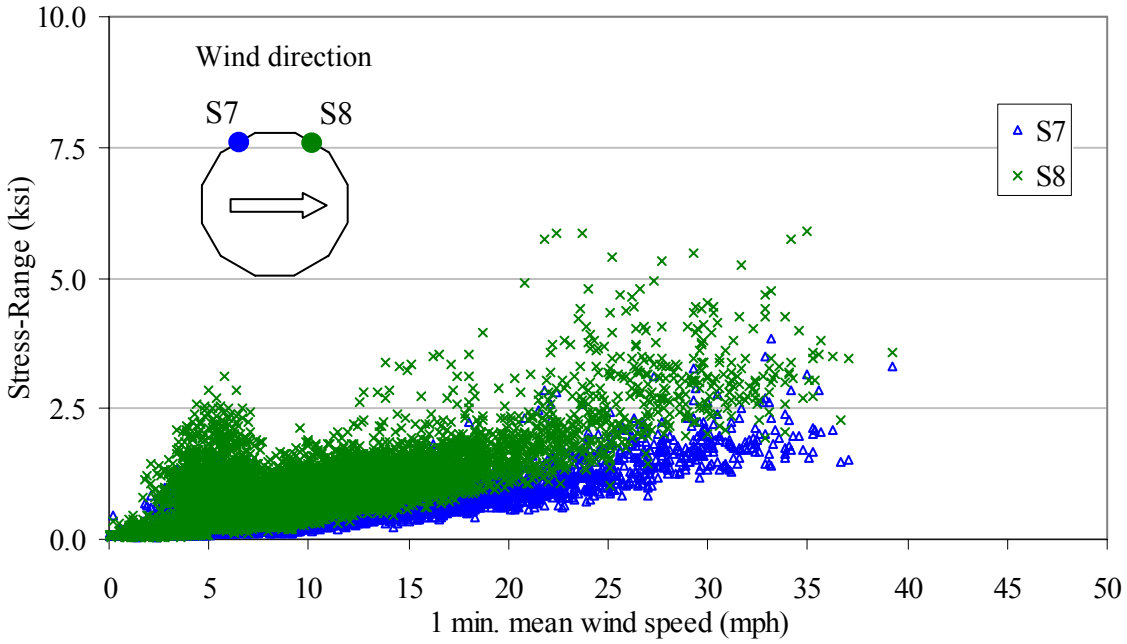

(d) Channels S7 and S8 at base

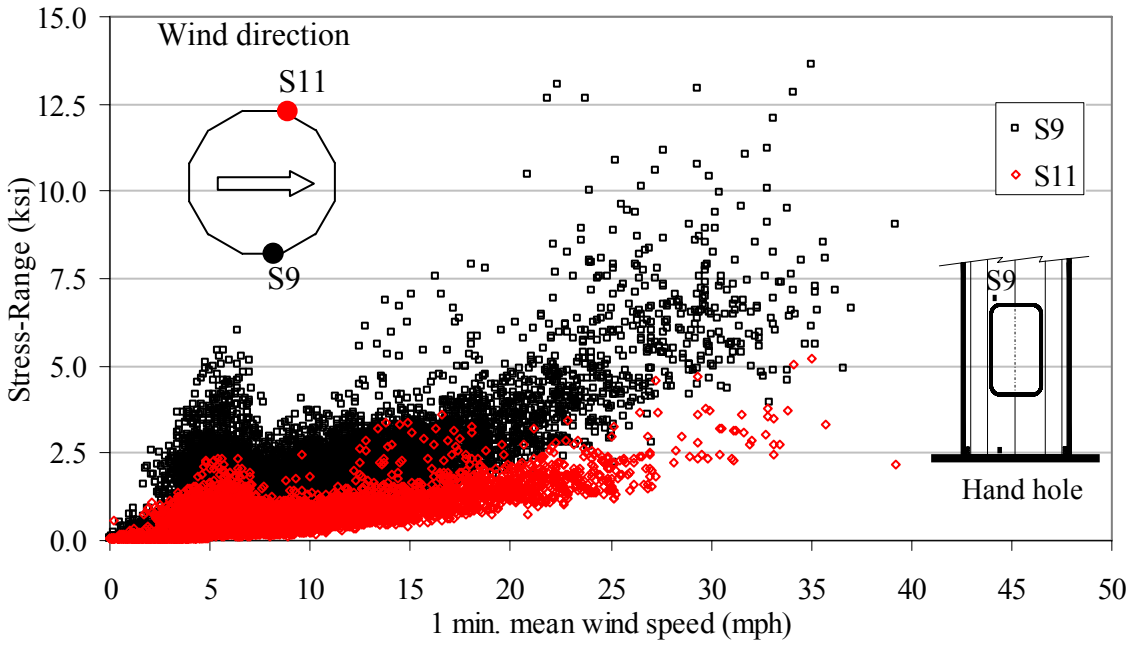

(e) Channels S9 near hand hole and S11 at base

Figure 3-22. (Continued)

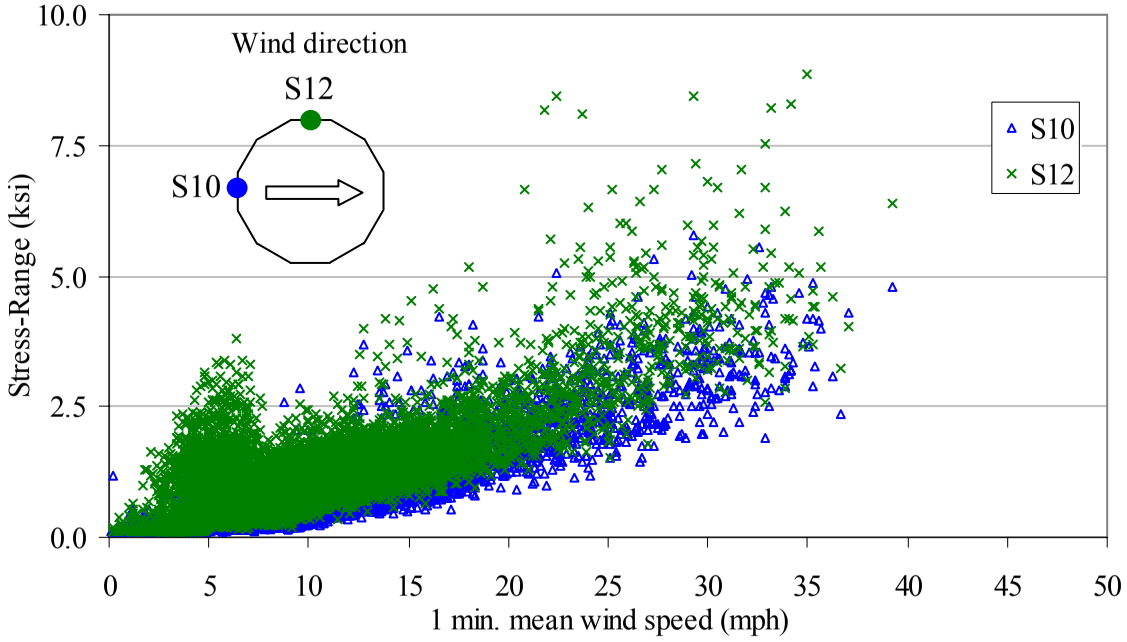

(f) Channel S10 and S12 at 5.75 ft from base

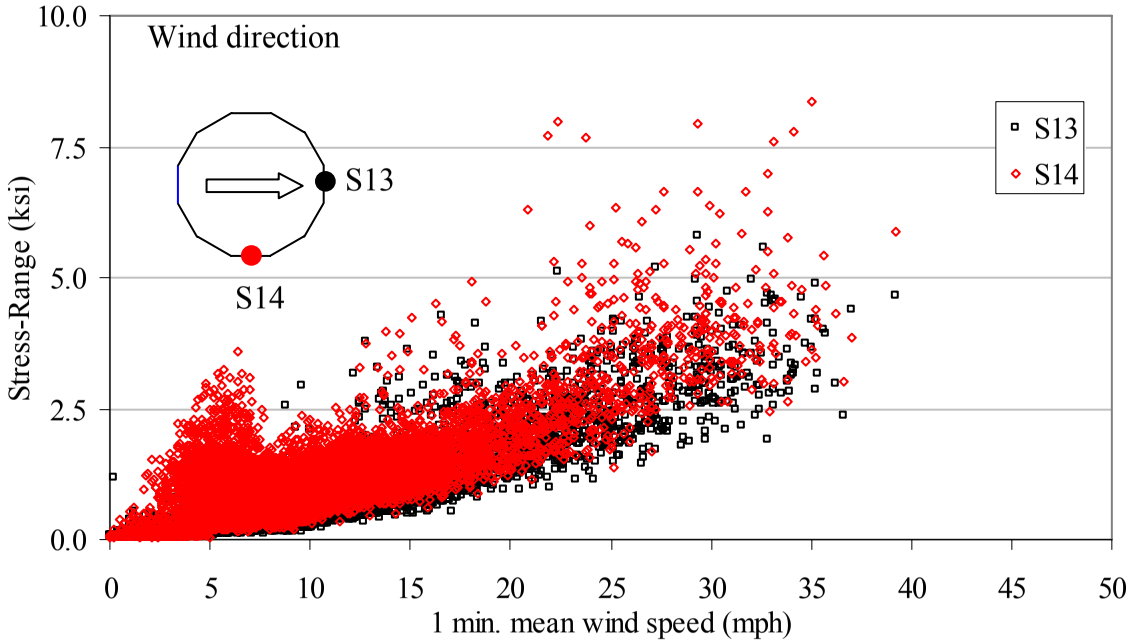

(g) Channels S13 and S14 at 5.75 ft from base

Figure 3-22. (Continued)

Stress ranges at locations near the base plate are lower than those at 5.9 ft from pole base as shown in Fig. 3-22. This is because there is a backer ring at the pole base with a thickness of 0.25 in. and a height of 3 in. Due to the additional thickness, it is estimated that the stress recorded at the nine strain gages would decrease approximately 50% and the stress ratio between an elevation of 5.75 ft and the pole base (ignoring any stress concentration) would be about 2. Figure 3-23 illustrates this and the stress ratios between channels near base plate and channels at 5.75 ft from pole base were determined to be between 1.5 and 2.5.

Table 3-8 shows the maximum stress range recorded at each channel during the monitoring. The largest stress range (19.68 ksi) during monitoring was observed at channel S9. S9 was oriented vertically on the Pole 1 at the upper left corner of the hand-hole in which high stress concentration might occur (see Fig. 3-5 (b)). At the elevation of 5.75 ft, the maximum stress range was measured as 12.4 ksi during the long-term monitoring.

Table 3-8. Maximum stress range (ksi) observed at each location for 1-minute interval

S1	S2	S3	S4	S5	S6	S7	S8	S9	S10	S11	S12	S13	S14
4.852	5.488	6.598	11.095	7.646	8.962	6.412	7.953	19.680	11.500	8.202	12.400	11.749	11.776

Figures 3-24, 3-25 and 3-26 show the maximum recorded stress time history at each channel for Pole 1. As an example, Figure 3-24 shows wind speed and direction time histories for a high-wind event which occurred on November 28, 2005 at 3:37 AM. It can be seen that the wind speed begun to increase suddenly to about 35 mph after approximately 35 second. Note that 321 degree wind direction denotes a generally East wind. This sudden gust event derived mostly largest stress rages as also shown in Figs. 3-25 and 3-26. A vibration period of 3.3 seconds was observed and this corresponds to the first modal frequency of the pole (0.3 Hz). Generally, the largest stress ranges were caused by natural wind gusting, primarily in the first mode.

Across-wind response (vortex shedding induced vibration)

When the wind speed reaches a critical level, vortex shedding commences. When the frequency of the vortex shedding reaches one of the natural frequencies, the poles lock-in and begin to oscillate in a specific mode corresponding to the vortex shedding frequency. The wind velocity at this phenomenon is known as the lock-in velocity, $V_{lock-in}$ (see Eq. 2.3). Table 3-9 shows the critical lock-in velocity along the height with respect to each mode shape. The peak normalized mode value (anti-node) possibly derives large displacement at the location and the vortex shedding induced stress would be great once lock-in phenomenon occurs at the anti-node. First, second and third mode vortex shedding vibration could occur at wind speed of 0.6 mph, 5.11 mph and 9.97 mph at 33 ft, respectively.

As previously shown in Fig. 3-22, when wind speeds are approximately 6.0 mph at 33 ft, the pole was excited in a direction perpendicular to the wind direction due to vortex shedding; this is especially evident from the output of channels S1, S2, S12 and S14. This indicates that the vortex shedding induced vibration corresponds well to the possible wind velocity for second mode vortex shedding vibration shown in Table 3-9.

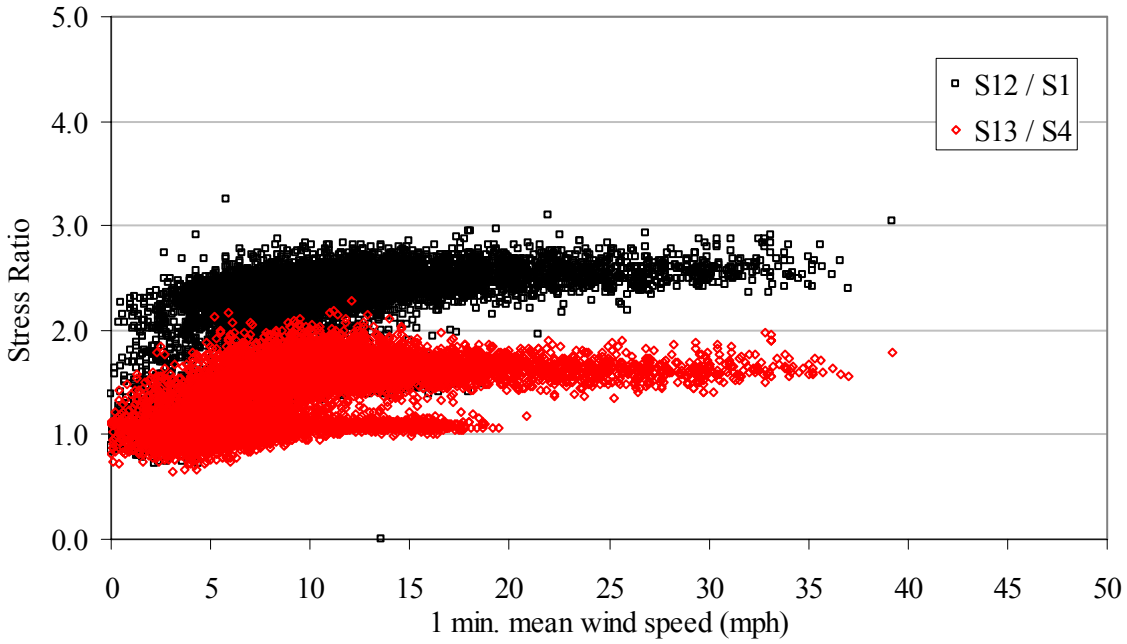

(a) S12/S2 and S13/S4

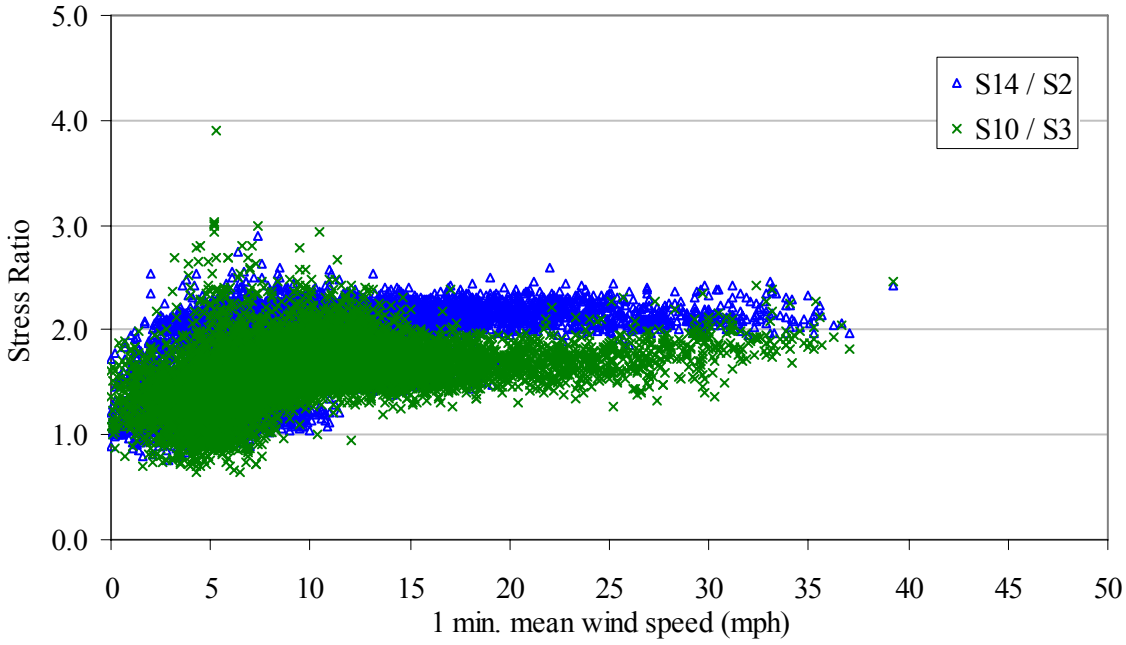

(b) S14/S2 and S10/S3

Figure 3-23. Stress ratios between pole base and 5.75 ft from the pole base

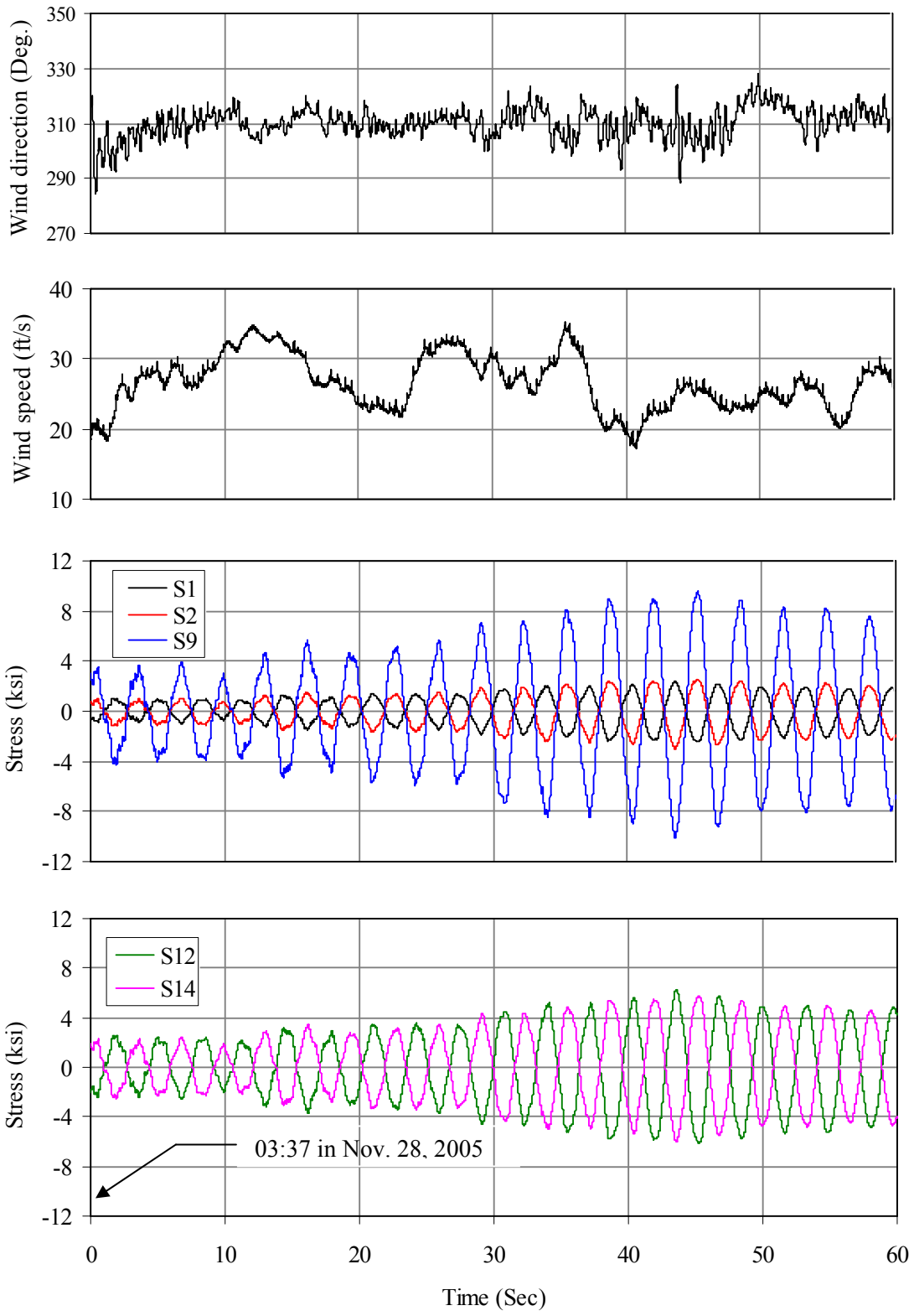

Figure 3-24. Wind gust-induced vibration at 1 min. mean wind speed of 26.55 mph

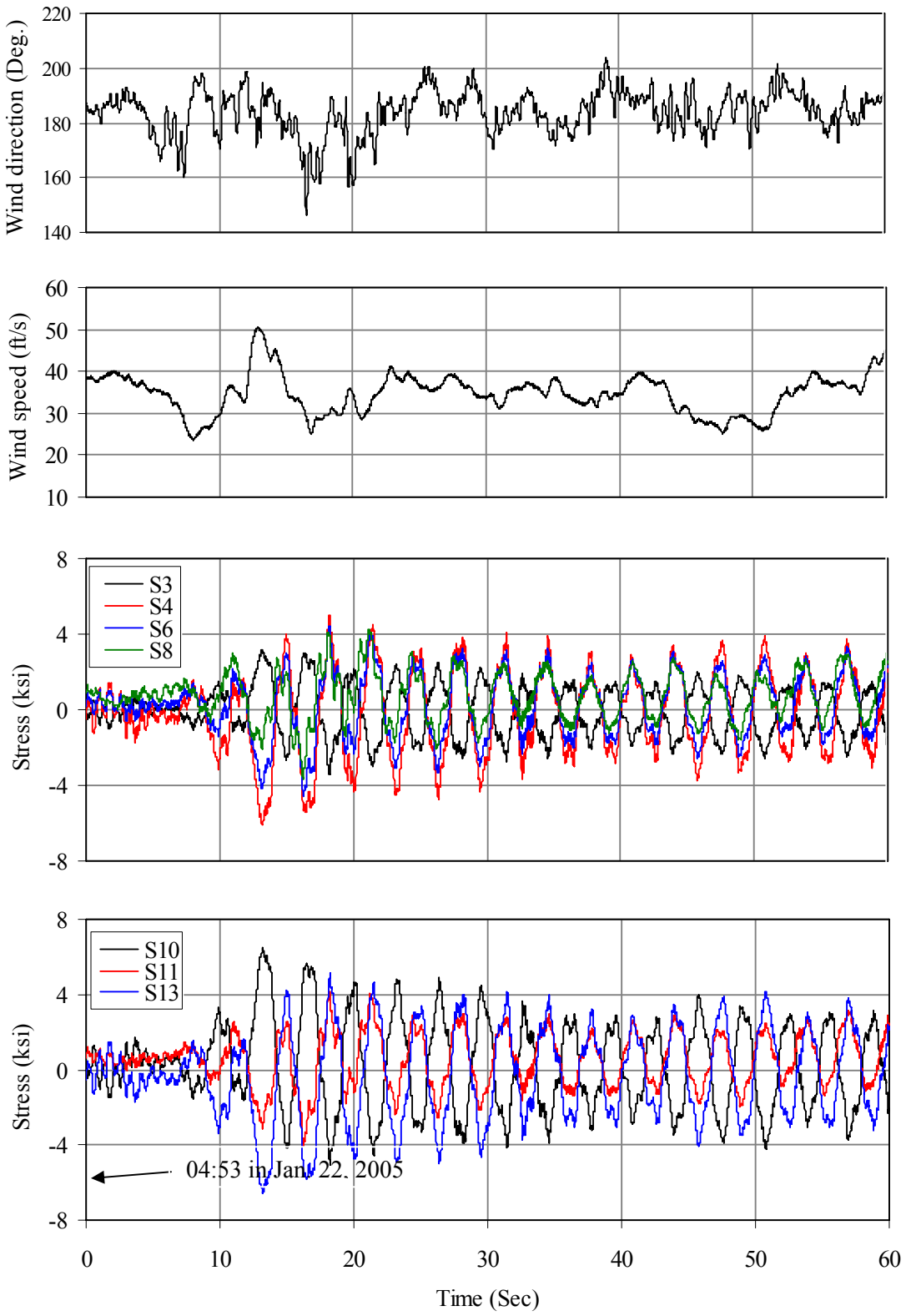

Figure 3-25. Wind gust-induced vibration at 1 min. mean wind speed of 34.63 mph

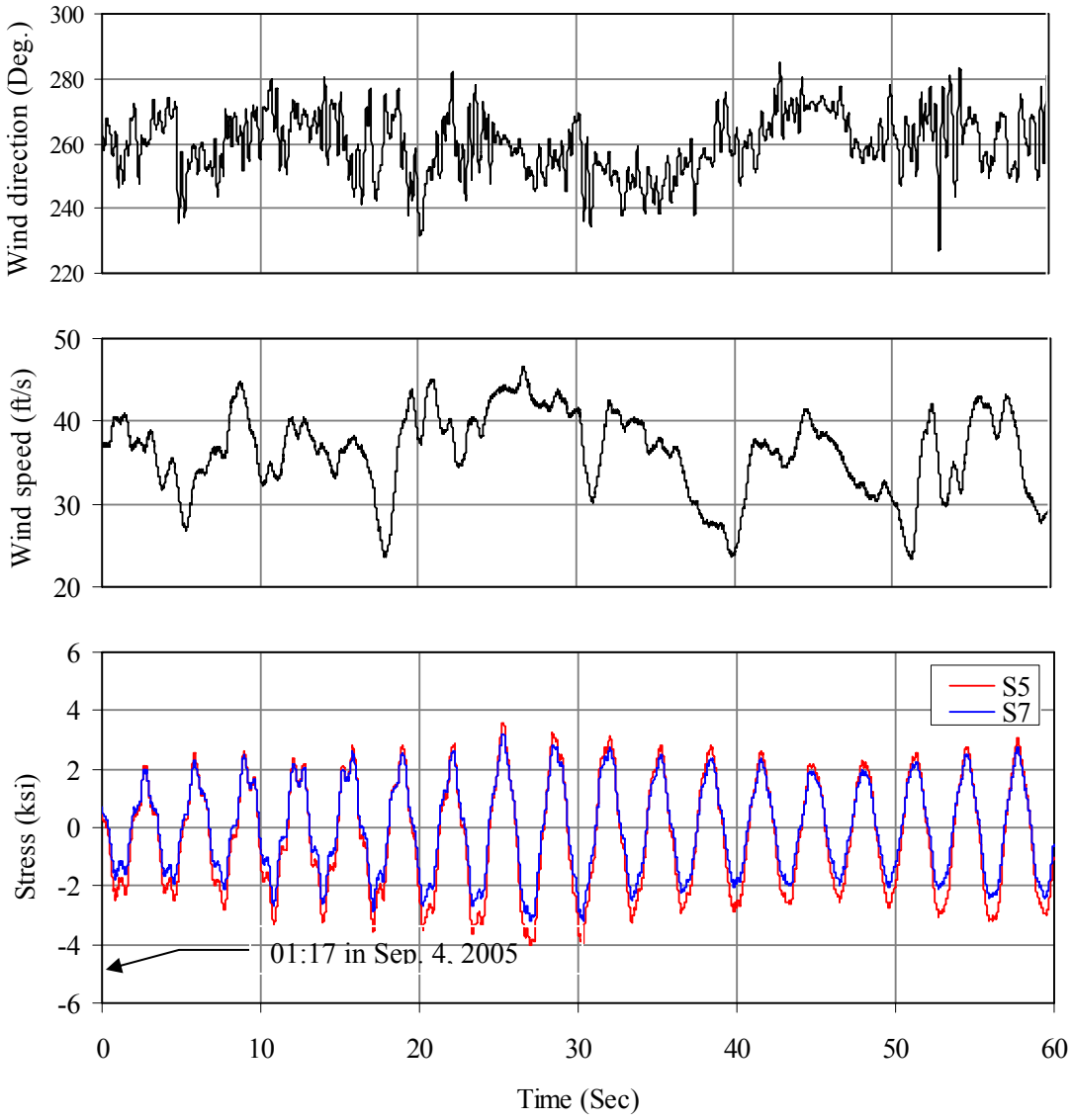

Figure 3-26. Wind gust-induced vibration at 1 min. mean wind speed of 36.31 mph

Table 3-9. Critical wind speed (at 33 ft) to induce vortex shedding vibration on HMLP

Event	Height	Critical diameter		Critical wind speed at 33 ft, mph			
	ft	in.	ft	f_1, 0.3 Hz	f_2, 1.3 Hz	f_3, 3.3 Hz	f_4, 6.4 Hz
Antinode1 (f_4)	41	22.75	1.90				39.83
Antinode1 (f_3)	57	21.02	1.75			18.12	
S.P.1 (f_4)	65	19.90	1.66				
S.P.1 (f_3)	88	16.68	1.39				
Antinode2 (f_4)	89	16.54	1.38				25.96
Antinode1 (f_2)	92	16.10	1.34		5.11		
S.P.2 (f_4)	109	14.23	1.19				
Antinode2 (f_3)	119	12.84	1.07			9.97	
Antinode3 (f_4)	129	11.42	0.95				17.01
S.P.1 (f_2)	132	11.02	0.92				
S.P.2 (f_3)	142	9.62	0.80				
S.P.3 (f_4)	145	9.19	0.77				
Top	148	8.77	0.73	0.6			

Note: S.P. stands for Stationary Point

An example of the second mode vortex resonant vibration is shown in Fig. 3-27. Figure 3-27 shows wind speed and direction time histories for a vortex shedding event which occurred on January 17, 2005 at 7:01 PM. Within the observed period, the stress range amplitude remained rather stable because there was only minor along-wind response. A maximum stress range of approximately 3.5 ksi at channel S4 was observed at a mean wind speed of approximately 5.5 mph. Interestingly, the vibration period of 0.77 seconds observed and the dominant frequency of vibration due to vortex shedding at that wind speed was measured to be 1.3 Hz (second modal frequency, see Table 3.4). This is contrary to current design procedure in AASHTO [7] which was the first mode frequency for calculating equivalent static pressure.

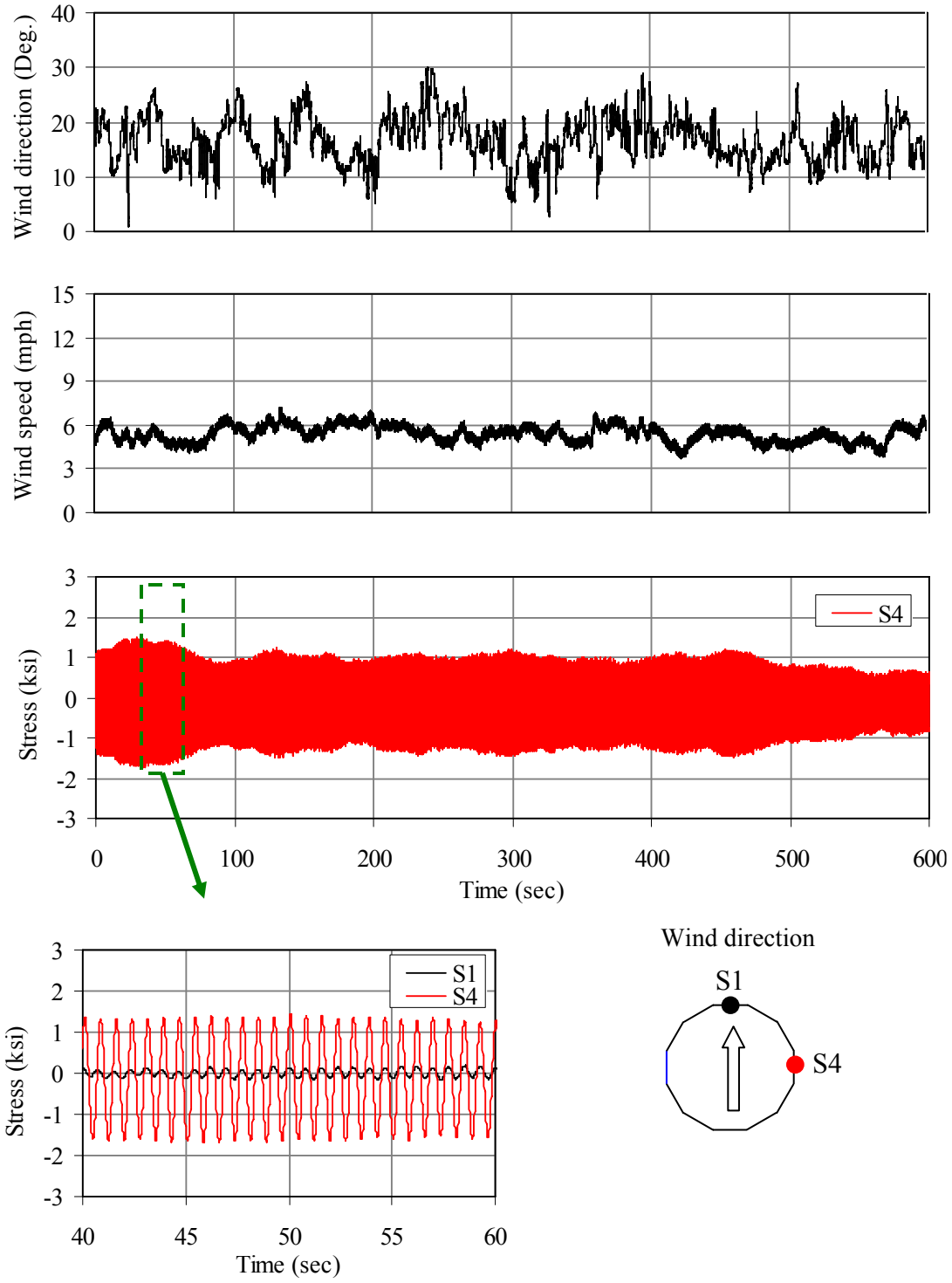

Figure 3-27. 2nd mode vortex shedding induced vibration at mean wind speed of 5.5 mph

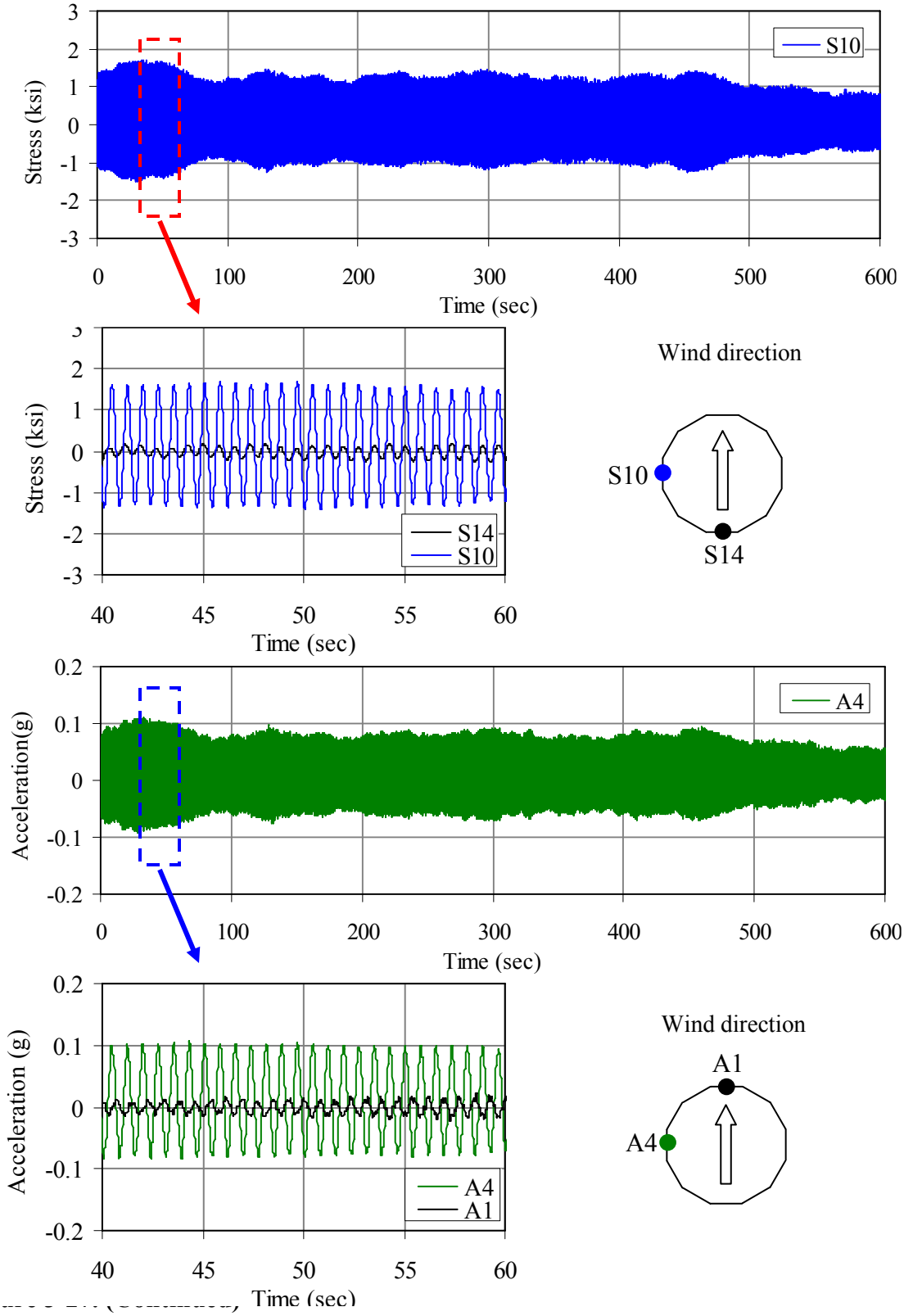
Stress (ksi)
Time (sec)
S10
S14
Wind direction
Acceleration(g)
Acceleration (g)
A4
A1

The subcritical range where the vortex shedding is strongest is approximately $300 < Re < 3.0 \times 10^5$ [39] and proper range of Reynolds number should be considered for the vortex shedding vibration. This is because there may not be potential critical lock-in velocities for 3rd or 4th mode vortex shedding vibration. Even third mode vortex shedding for antinode1 as shown in Table 3-8, the Re at the location which wind velocity is 18.12 mph exceed Re of 3.0×10^5. Thus, the magnitude of vortex shedding vibration as this location may not be fully resonant.

An example is shown in Fig. 3-28 and it shows wind speed and direction time histories for a vortex shedding event which occurred on November 1, 2005 at 1:150 AM. Within the observed period, the stress range amplitude did not remain stable because there was along response as well as vortex shedding resonance phenomena. A maximum stress range of approximately 2.9 ksi at channel S13 was observed at mean wind speed of about 18.67 mph when the vortex shedding occurred. The vibration period of 0.3 seconds also observed and the dominant frequency of vibration due to vortex shedding at that wind speed was measured to be 3.3 Hz. This third mode vortex shedding vibration was observed a range of wind speed between approximately 8 mph and 20 mph.

It has been found that second mode vortex shedding is most common at the HMLP. The stress range at some specific channels exceeded the Constant Amplitude Fatigue Limit (CAFL) for Category E' (2.6 ksi) [7].

Stress-Cycle Counting

Six specific strain channels on each HMLP were used to develop stress range histograms based on the rain-flow cycle counting algorithm [86]. There were 20 stress range bins at 0.5 ksi each with a max of 10 ksi for Pole 1. Figure 3-29 shows the number of stress cycles at the selected strain gages (Channels S1, S3, S9, S10, S11, and S11). The stress cycles of less than 0.5 ksi were discarded due to the small magnitude. Strain gage S9 observed the largest number of stress cycles because the gage was placed near the hand hole in which stress concentration might occur.

For Pole 2, there were 16 stress range bins at 0.5 ksi each with a max of 8 ksi . Figure 3-30 shows the number of stress cycles at the selected strain gages (Channels S1 to S6). The stress cycles of less than 0.5 ksi were also discarded due to the small amount of magnitude. The strain gages S5 and S6 observed the largest number of stress cycles because the other sensors (S1 to S4) were located on the retrofitted area.

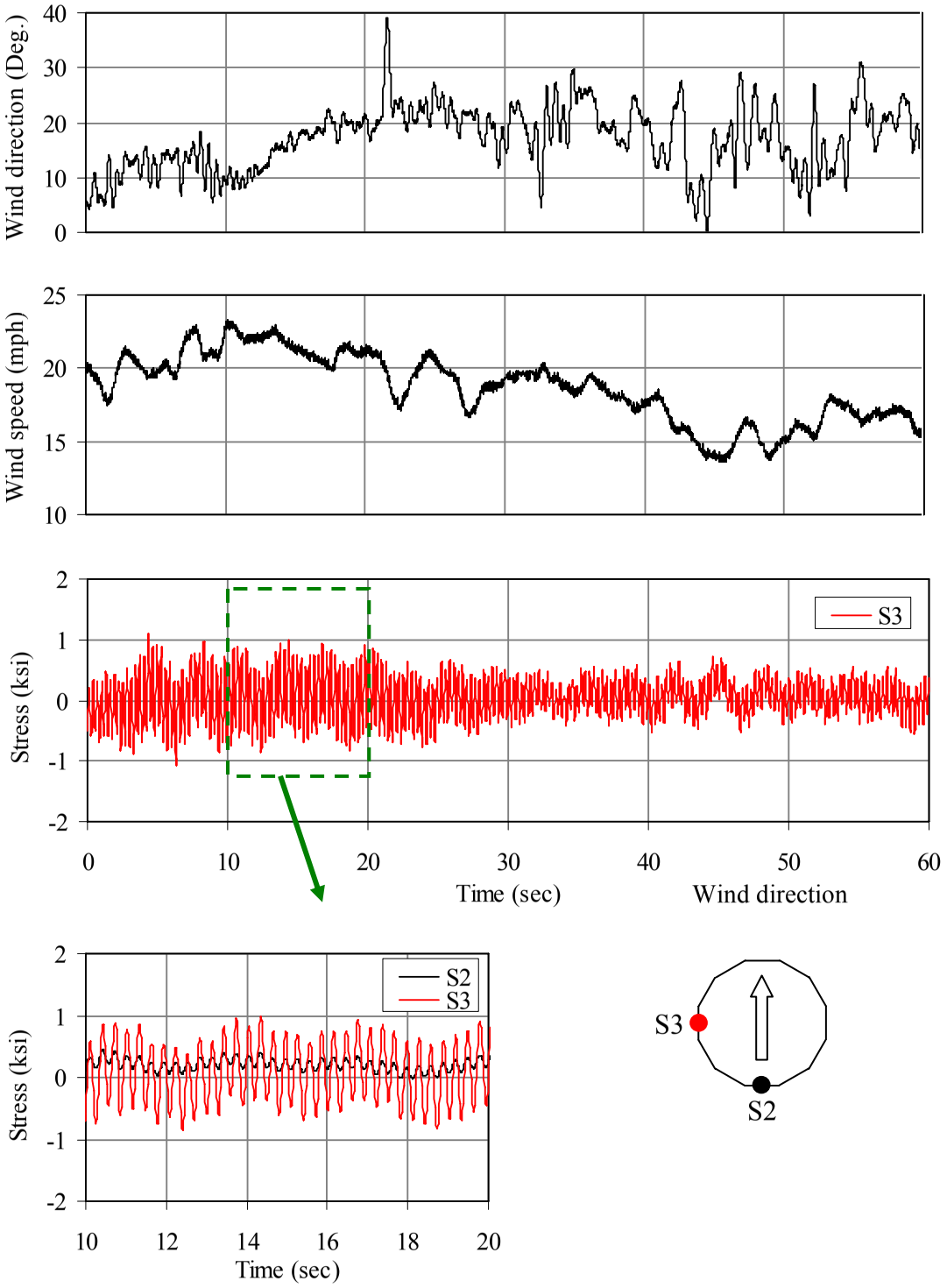

Figure 3-28. 3rd mode vortex shedding induced vibration at mean wind speed of 18.67 mph

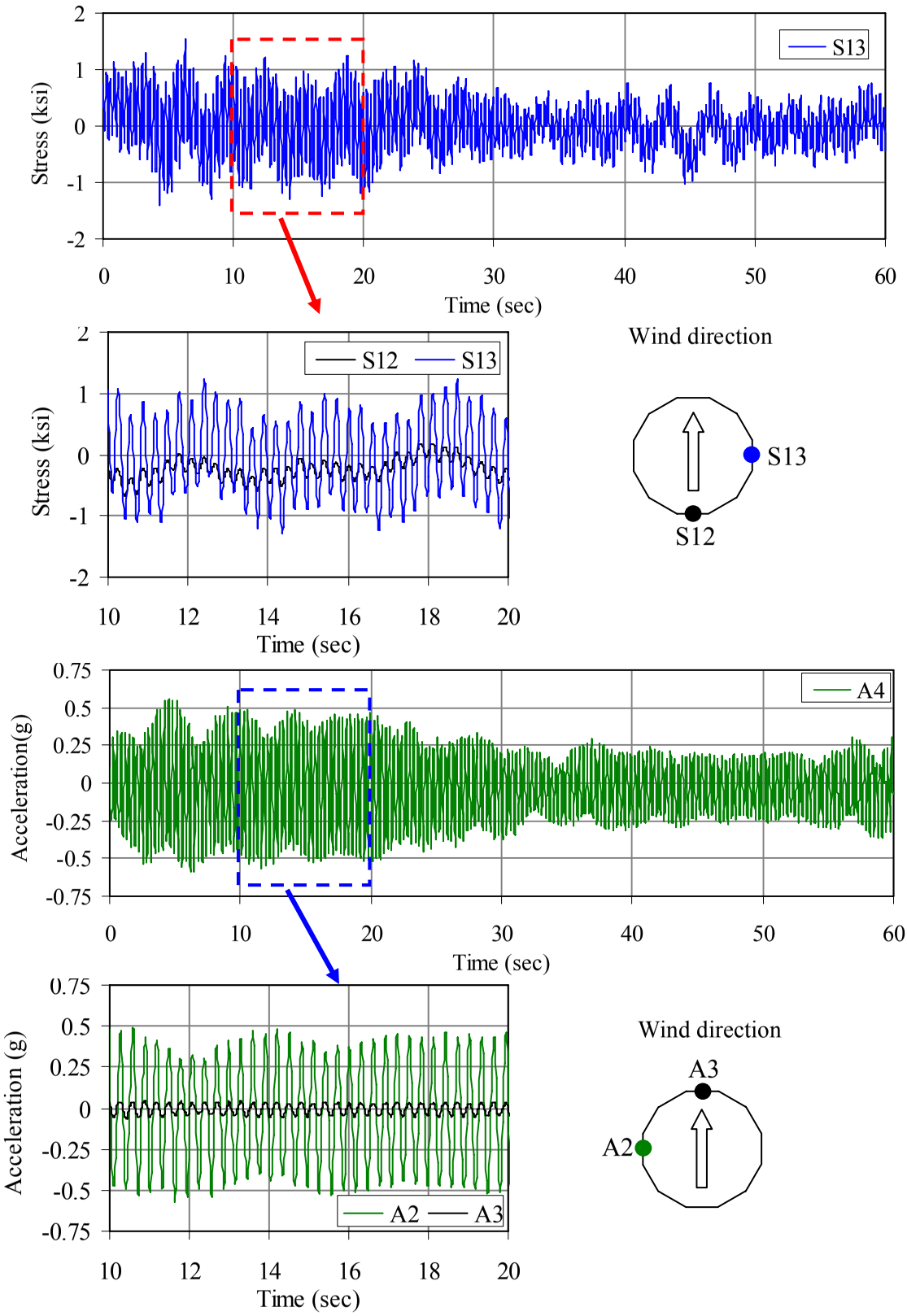

Figure 3-28. (Continued)

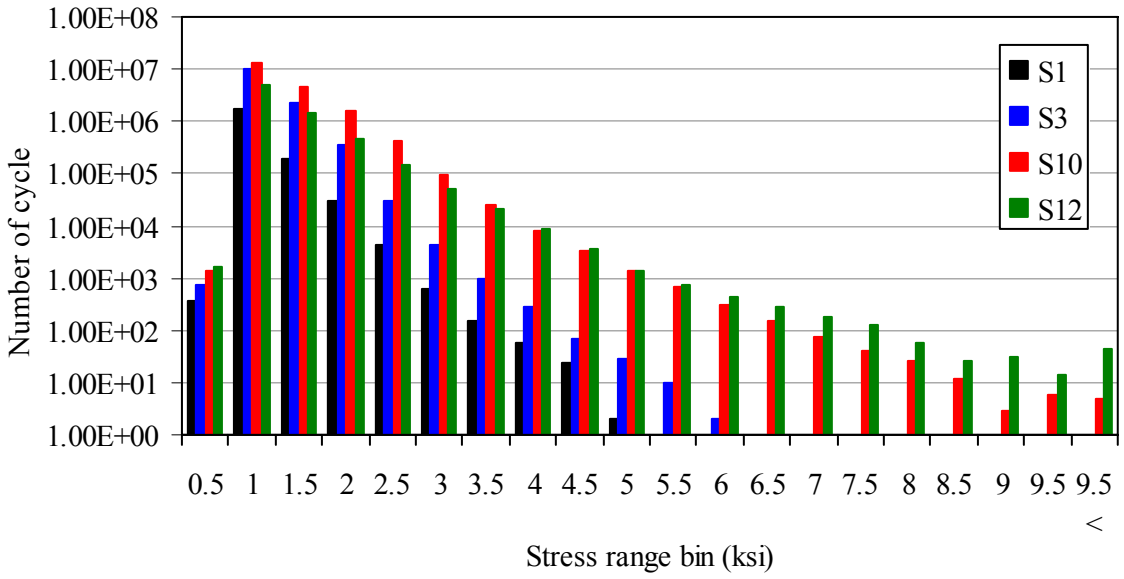

(a) Strain gage No. 1, 3, 10, and 12

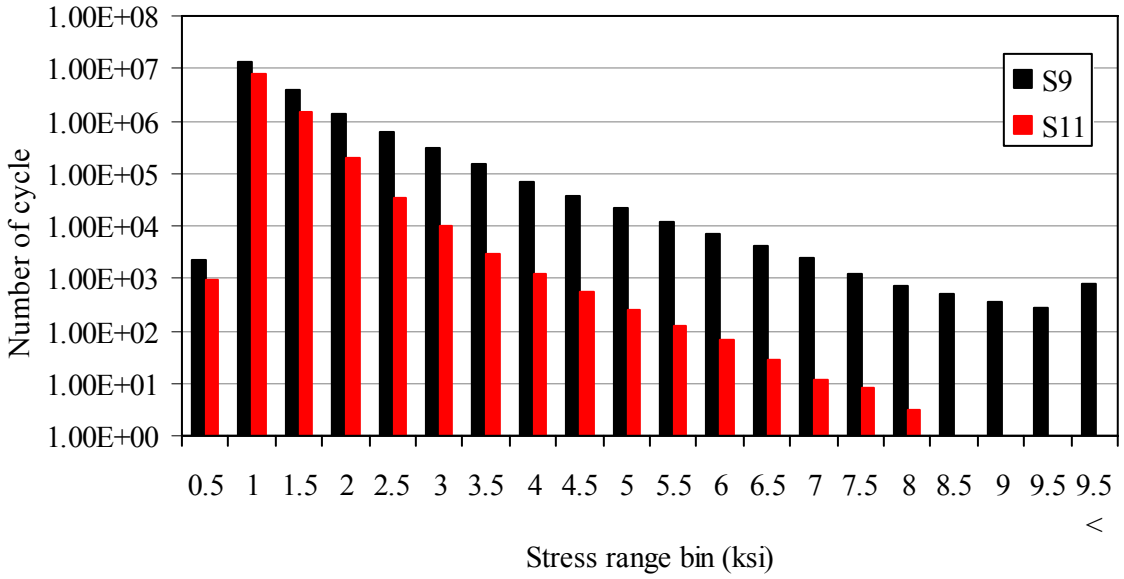

(b) Strain gage No. 9 and 11

Note:

Data were recorded only during approximately 92.4 % of the total duration (October 15, 2004 to January 5, 2006).

Figure 3-29. Number of stress cycles collected from Pole 1

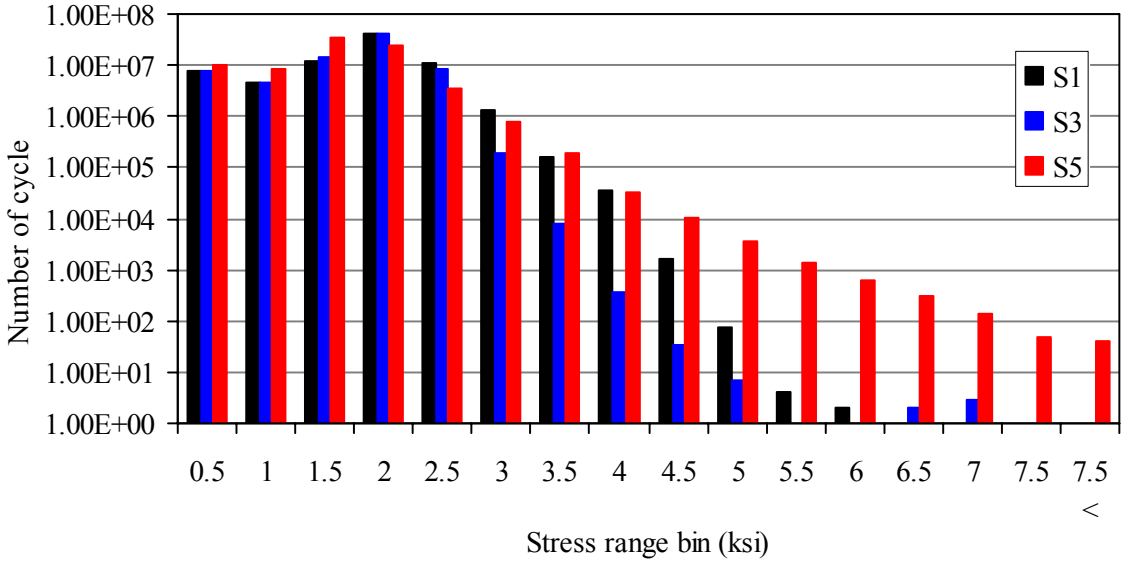

(a) Strain gage No. 1, 3 and 5

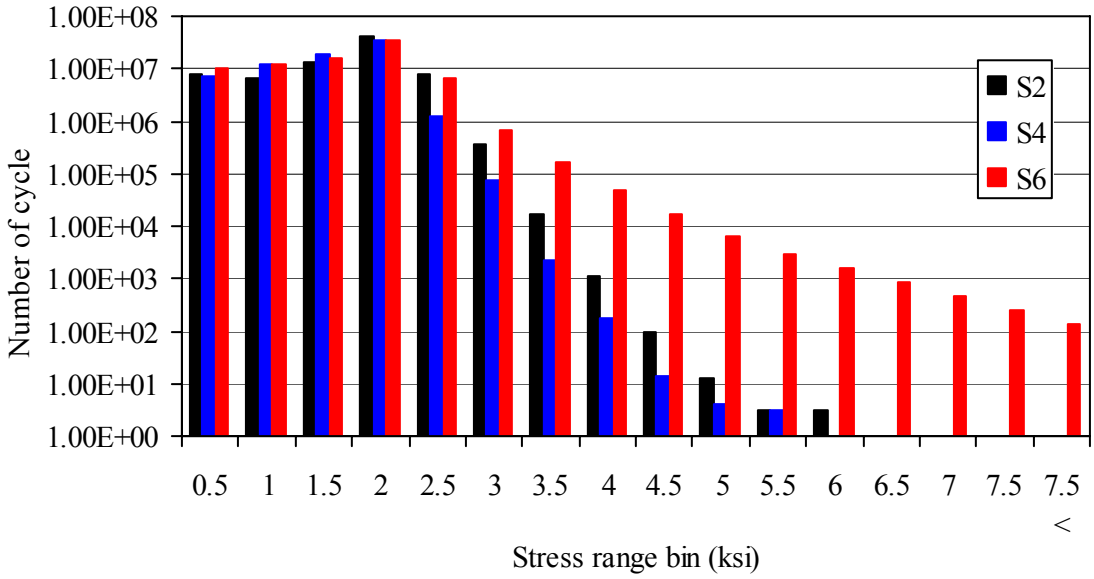

(b) Strain gage No. 2, 4 and 6

Note:

Data were recorded only during approximately 67.5 % of the total duration (October 15, 2004 to January 5, 2006).

Figure 3-30. Number of stress cycles collected from Pole 2

4. WIND TUNNEL TESTING

Wind tunnel testing is routinely used to study various aerodynamic phenomena and determine aerodynamic parameters of civil engineering structures. Also, the general flow pattern around structures can be determined from wind tunnel testing, particularly in the case of unusual structural shapes. Wind tunnel testing aids in structural design and planning because required aerodynamic coefficients may not always be available in codes or standards [59]. Recall that the light pole that was instrumented for this work has a dodecagonal (12-sided) cross-section with a taper. For this specific shape, the current AASHTO code does not provide all the aerodynamic parameters such as the static force coefficients, their slopes with angle of attack, Strouhal number, the lock-in range of wind velocities and amplitude of vortex-induced vibration as a function of Scruton number, etc, that are needed for proper evaluation of aerodynamic behavior. Thus, wind tunnel testing was required to obtain these parameters.

4.1. Wind Tunnel

In order to determine wind-induced loads on a structure, aerodynamic parameters such as, Strouhal number, drag and lift coefficients, etc, are necessary. However, only a few references provide values of some of these parameters in a certain range of Reynolds number for the dodecagonal shape studied here. The wind tunnel that was used in this study is the Bill James Open Circuit Wind Tunnel located in the Wind Simulation and Testing Laboratory (WiST Lab) at Iowa State University, Ames. This is a suction type wind tunnel with a 22:1 contraction ratio. The wind tunnel has a test section of size 3ft x 2.5ft and length of 8ft following the contraction exit. The test section has an acrylic viewing window adjacent to the wind tunnel control station and an access door on the opposite side (see Fig. 4-1). The fan, located downstream of the test section, is powered by a 100 hp, 3-phase, 440-volt motor. An analog remote control knob, located at the wind tunnel control station and connected to the variable frequency fan, provides continuous control of the fan speed. The fan speed can be changed stepwise, in increments of approximately 0.51 ft/s per 0.1 Hz, using this control. The fan can generate a maximum wind velocity of approximately 180 mph or 264 ft/sec [89].

Figure 4-1. Bill James Wind Tunnel at Iowa State University

4.2. Test Model

For all tests, a wooden cylindrical model with dodecagonal (12-sided) cross section of a diameter 4 in. (corner to corner distance) and length 20 in. was used. These dimensions were selected based on the need to maintain a wind tunnel blockage criterion of 8% or less. The actual blockage was 7.4% and, thus, blockage effects could be ignored. The length of the model was chosen as 20 in. to maximize the area of the model exposed to the air stream while at the same time leaving enough space on either side of the model for clamping additional fixtures that would be required to vary certain parameters.

Figure 4-2 shows a schematic diagram of the model. The model was prismatic with sharp edges along its length. The model was lightly sanded with extra fine grit sand paper to obtain a smooth surface finish and to remove any excess adhesive. A block was set into each end of the model and glued into place. The face of the block was flush with the end of the model. A collar with set-screws was attached to each block that helped to clamp a hollow aluminum alloy rod at each end of the model. The 0.625 in. diameter aluminum alloy rod was installed by sliding a rod through a 0.75 in. diameter hole at the center of the block and the center of the model. A collar was then slid over each end of the rod and attached to the block. This helped to clamp the model to the rod with the set screw and this configuration could be connected to a force balance system.

End plates made out of clear plastic were attached to the model to minimize three-dimensional end effects and to thus maintain a two-dimensional flow on the model. To test multiple specimens of the model with a different mass, pairs of commercially available C clamps were clamped to the end plates. The clamps were attached to the end plates at equal distance from the centerline to avoid torsion.

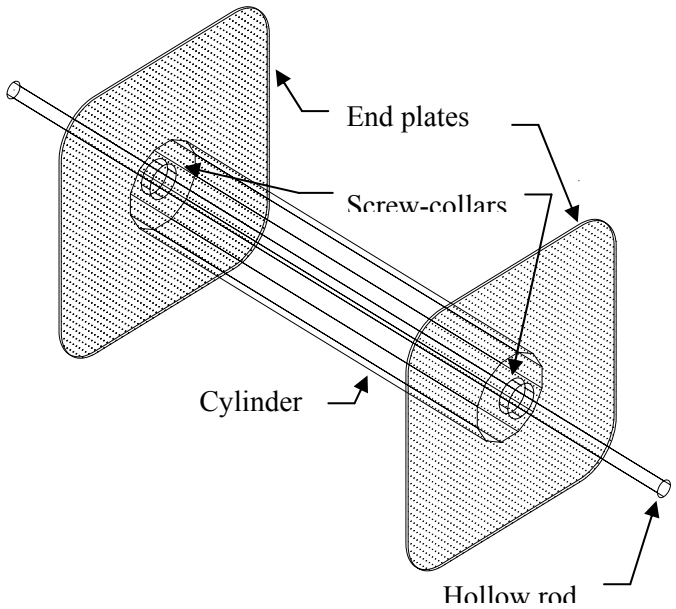

Figure 4-2. Schematic diagram of the 12-sided cross section model

4.3. Test Setup and Procedure

Several tests were conducted on the model to obtain the desired aerodynamic parameters. Results of primary importance include the following: the static drag coefficient, the derivative of the static lift coefficient with respect to the angle of attack, Strouhal number, the lock-in range of wind velocities for vortex shedding, amplitude of vortex-induced vibrations as a function of Scruton number, and aerodynamic admittance functions.

4.3.1. Static Test

For the static tests, the model was fixed horizontally in the wind tunnel with zero yaw angle and the aerodynamic forces were measured at various wind speeds. Figure 4-3 shows a photograph of the setup with the model in place. The angle of attack was varied by rotating the model about its longitudinal axis. Wind speeds were carefully chosen to provide a large range of Reynolds numbers.

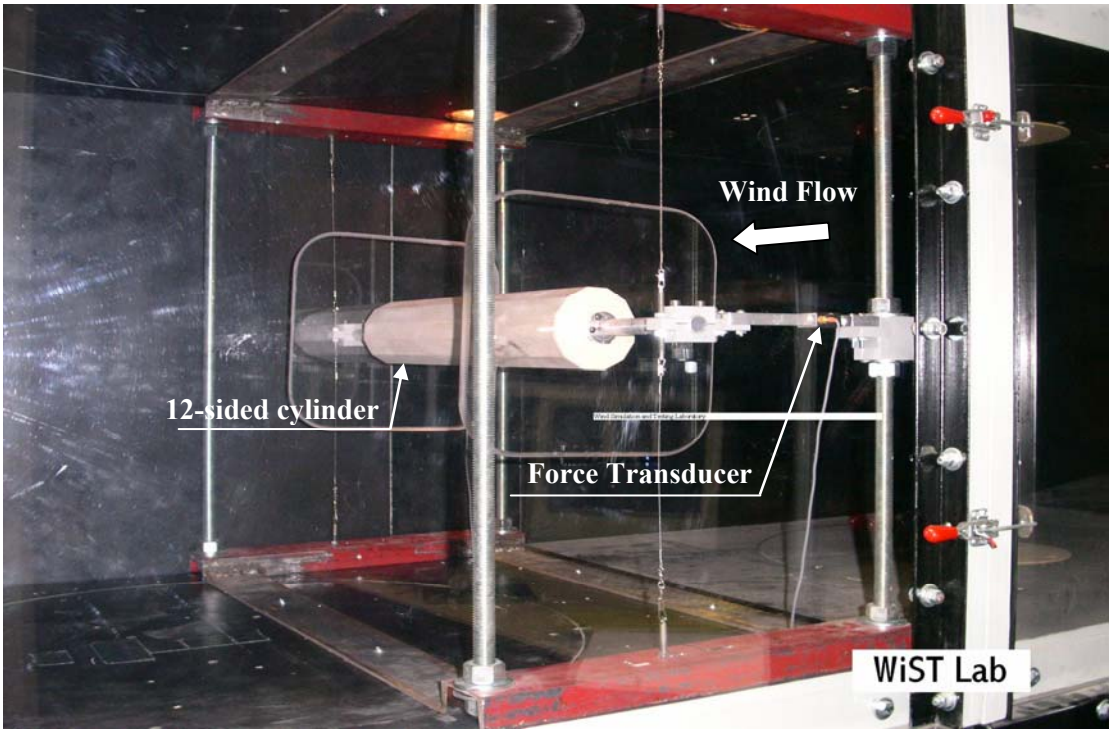

Figure 4-3. Drag measurement

The load cells for this system were fixed to the test frame as shown in Fig. 4-4. Thin strings were attached to the aluminum block at each end of the model to avoid vertical deflection of the model.

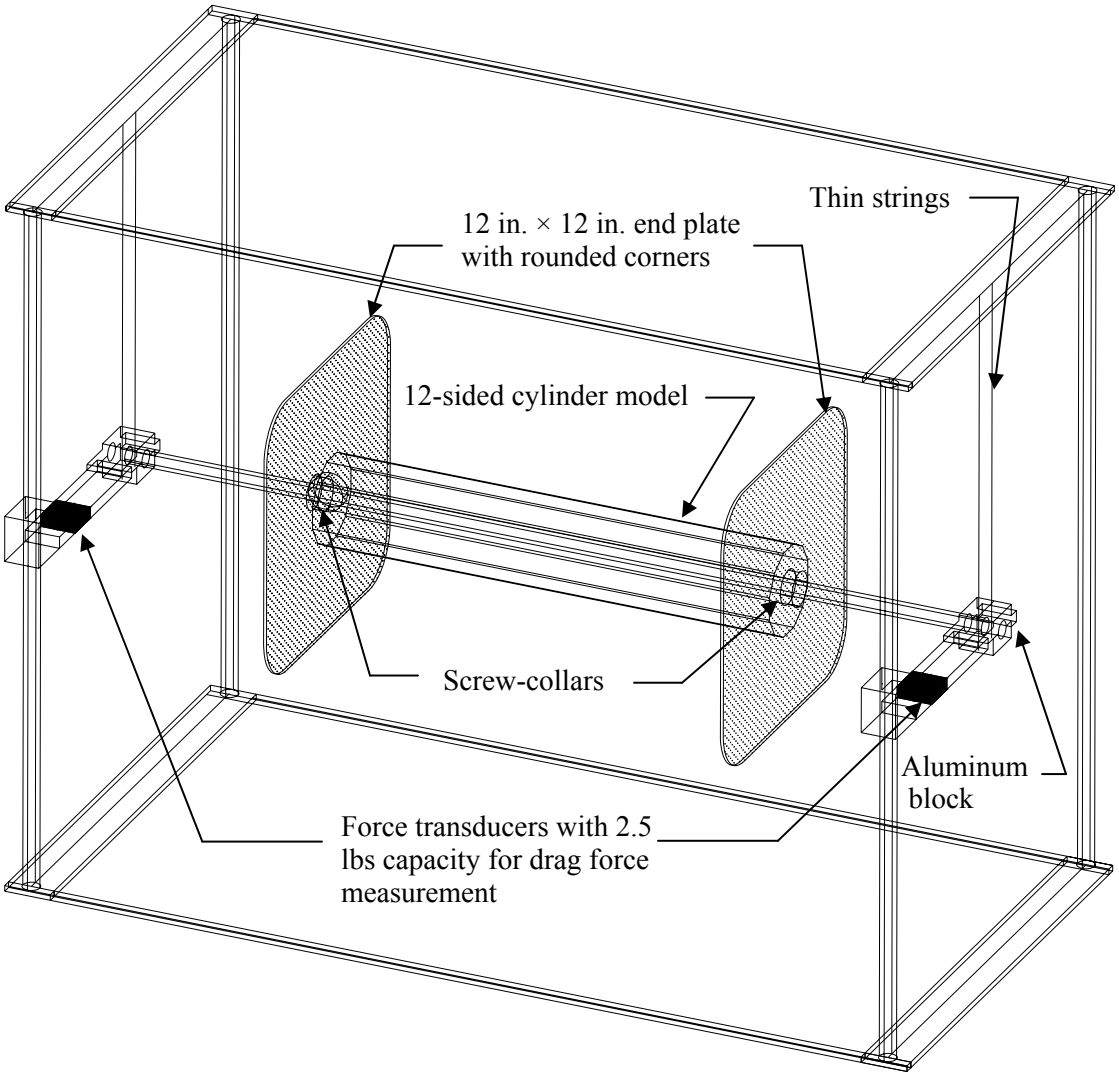

Figure 4-4. Schematic diagram for static drag measurement

Data Acquisition System

The force measurements were made with two transducers (Transducer Techniques, SL 146502 and SL 146503) each with a capacity of 2.5 *lbs*. The transducers were rated at 2.1576 *mV/V* and 2.0778 *mV/V* per pound of load, respectively. The gain for all the experiments was fixed at 100 and the excitation signal was set at 10 *V*. This produced an output voltage to load ratio of 0.9657 *V/lb* for SL 146502 and 0.8507 *V/lb* for SL 146503, respectively.

The commercially available software package LabView, developed and marketed by National Instruments, was used for the acquisition of the transducer force with velocity data. The program displayed the recorded data (voltage) plotted against time and its statistics such as 'mean'. A Pentium III PC with Windows XP operating system was used to power the data acquisition software.

Experimental procedure

There were two experiments that were conducted to determine drag forces (i.e., flat and corner orientations, see Fig. 4-5). The following steps describe the experimental procedure followed to measure the drag coefficient.

- Fix the model to the force balance system with one of the flat faces normal to the wind direction (see Fig. 4-5)
- Test the model over a range of wind speeds, increased incrementally up to the maximum force that the force transducers could record.
- Record the force output at each wind velocity and compute the mean drag coefficient at that speed
- Plot the mean drag coefficient as a function of Reynolds number
- Rotate the model by 15 degrees such that the corner to corner (corner orientation, see Fig. 4-5) of the model is along the wind direction
- Repeat the test and plot the mean drag coefficient as a function of Reynolds number

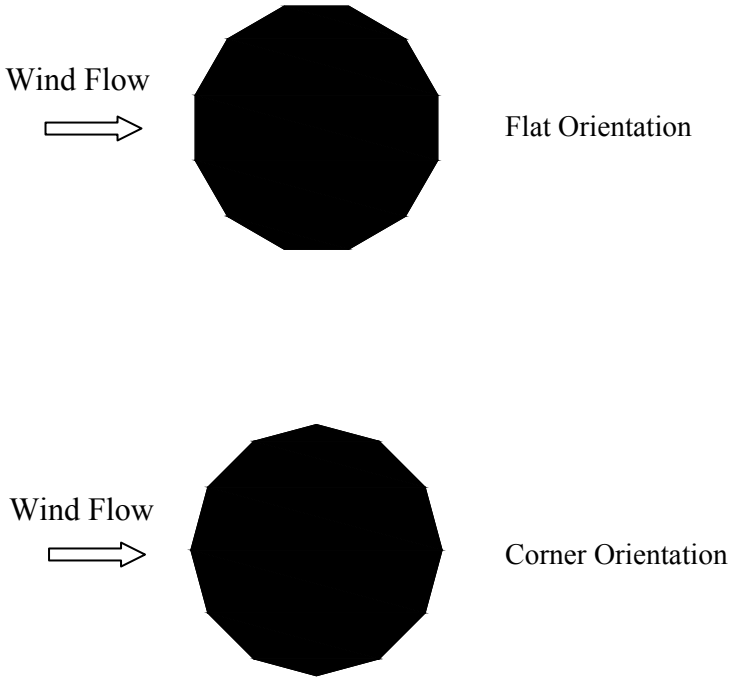

Figure 4-5. Dodecagonal model orientations

4.3.2. Dynamic Test

Figure 4-6 shows the dynamic test setup that was used to study the vortex shedding induced response. The vertical motion dynamic setup was designed to allow only single-degree-of-freedom; that is; the test model was free to vibrate only transverse to the wind direction. The model was suspended by a set of eight linear coil springs and chains, four on each side of the model. Two force transducers were used, one at the bottom and one at the top placed at diagonally opposite springs as shown in Fig. 4-6.

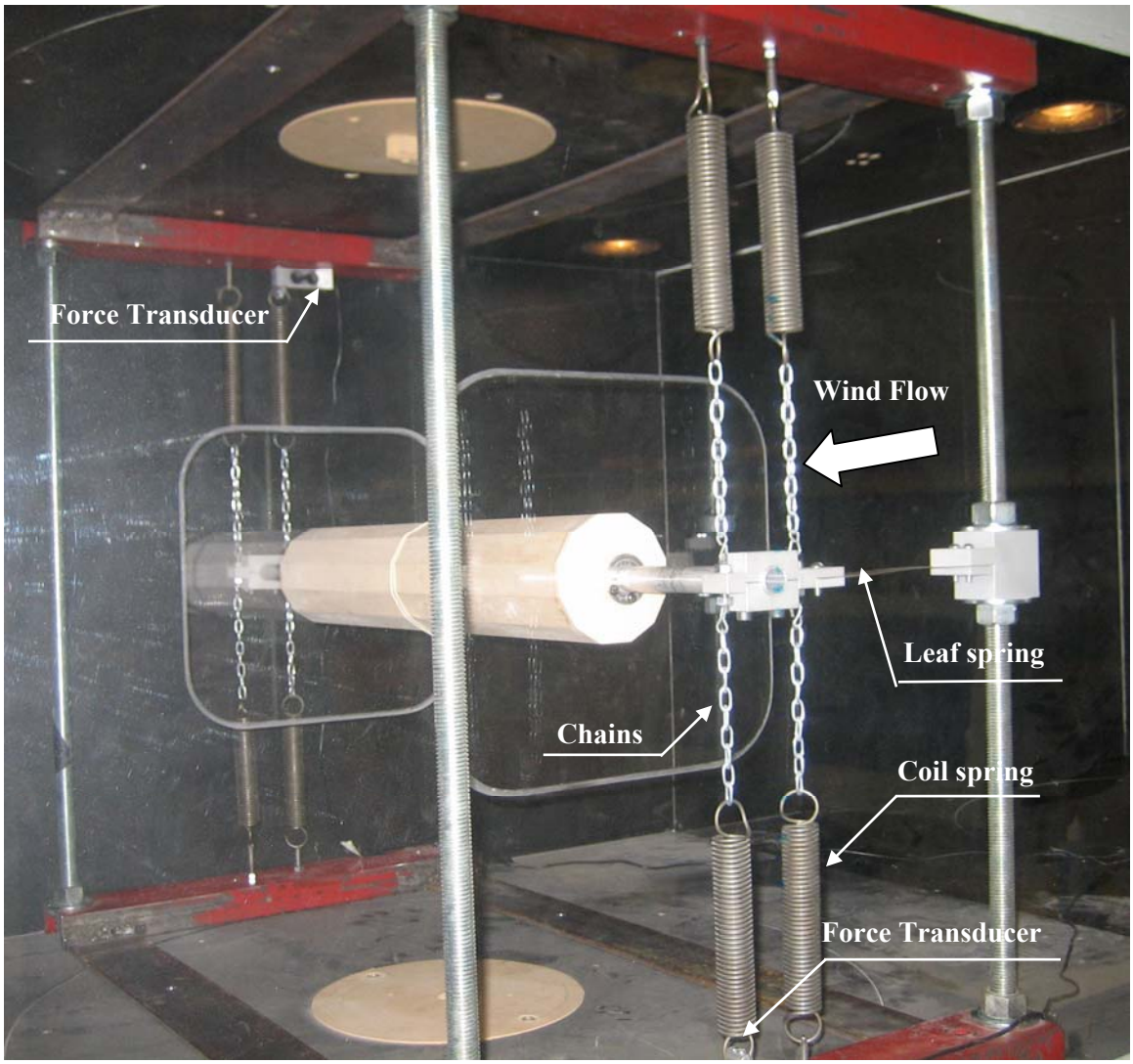

Figure 4-6. System view for dynamic test

Spring Suspension System

The spring suspension system was attached to a frame that was fixed to the test section floor and ceiling immediately adjacent to the side walls. A load cell frame was constructed with small structural channels and four 0.75 in. diameter threaded steel rods - two on each side of the test section - which spanned vertically from floor to ceiling. The suspension system was designed to allow only vertical motion; in other words, the test models were free to only vibrate transverse to the wind direction. Figure 4-7 is a schematic diagram of the dynamic test. The load cells were placed at the diagonally opposite spring to cancel the effects of any spurious modes other than the vertical one.

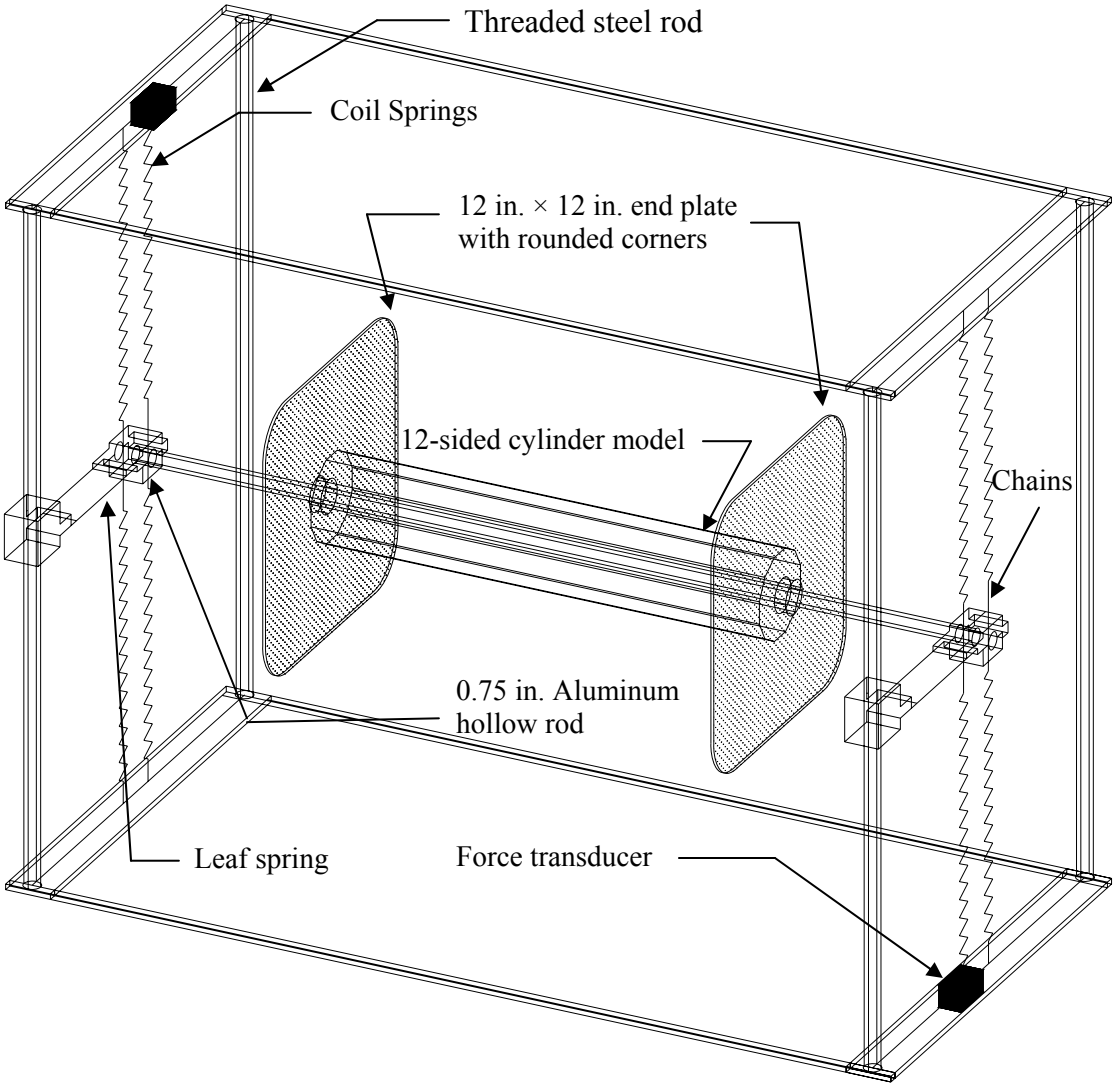

Figure 4-7. Schematic diagram of the general system for the dynamic test

The stiffness of an individual coil spring was rated at 4.13 lb/in., which was determined separately by preliminary extension testing. The combined stiffness of the eight springs was calculated to be 396.5 lb/ft. Two leaf springs on each side of the test section restrained the model in the along-wind direction. The leaf springs were 1.25 in. wide, 0.010 in. thick, and approximately 5 in. long that had negligible stiffness compared to the combined stiffness of the coil springs.

Data Acquisition System

The elastic spring force as a result of linear vertical motion was measured to obtain the displacement time histories. These force measurements were accomplished with two cantilever type force transducers (Transducer Techniques, SN 125595 and SN 125596) that have a capacity of 22 *lb* each. The transducers were rated at 1.5 *mV/V* per 22 pound of force. The gain used in these experiments was 1000 and the excitation signal was set as 10 V. This produced an output voltage to force ratio of 0.69 *V/lb* or and output voltage to displacement ratio of 2.82 *V/in.*

The signals from the two transducers were added and then halved to record average vertical motion of the test model. This arrangement of transducers and resulting signals that were combined helped to eliminate noise from any spurious pitching or yawing modes of vibrations as mentioned earlier.

Experimental procedure

As shown in Figs. 4-6 and 4-7, the section model with the flat orientation and end plates was suspended by a set of eight linear springs, four on each side of the model. The model was tested over a range of wind speeds that would produce vortex-induced vibrations. The wind speeds were increased in increments of 0.1 Hz of fan speed (AC Motor Controller) of the wind tunnel with initial fan speed set at 0.5 Hz. Each increment of fan speed represented an approximately 0.51 ft/s increase in the wind speed with an initial wind speed of approximately 3.5 ft/s.

The dynamic test procedures were established to obtain Strouhal number, the range of wind velocities producing vortex-induced vibrations, and the variation of amplitude of vortex-induced vibration with Scruton number. The following steps describe the experimental procedure followed to obtain these values for both flat orientation and corner orientation.

- Fix the model to the force balance system with one of the flat faces normal to the wind direction (flat orientation)
- Determine mass, stiffness, frequency, and damping of the system
- Calculate the Scruton number for the model
- Test the model over a range of wind speeds, increased incrementally until the model vibrates transversely
- Record and note the amplitude of the displacement at each wind speed
- Record time histories of displacement over the range of wind speeds that produced vibrations with appropriate sampling rate (1000 Hz) and duration (30 seconds)

- Compute the Strouhal number and vortex shedding frequency as a function of wind speed
- Plot the amplitude as a function of reduced velocity to explore large amplitude motions

4.3.3. Buffeting Test

The relationship between fluctuating wind velocity in the upstream flow and fluctuating wind load that it induces on a structure is commonly referred to as "Aerodynamic Admittance" [39]. Generally, this relation is determined experimentally since the flow around a structure in turbulent wind is too complex to be handled analytically. The buffeting indicial functions were obtained from static wind-tunnel model tests with an x probe hot-wire that was used to obtain the horizontal and vertical wind velocity fluctuations. Figure 4-8 shows the experimented setup for the buffeting test.

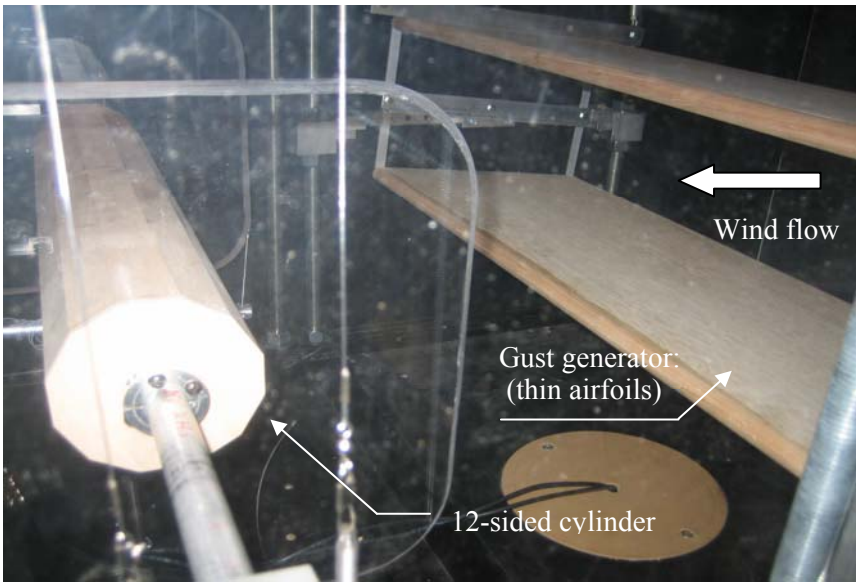

Figure 4-8. Experiment setup for the buffeting test

X-probe Hot-Wire Anemometer (HWA)

Hot-wire anemometry (HWA) is likely to remain the principal research tool for turbulent flow studies. Hot-wire probes are available as four types of sensors: Miniature wires, Gold-plated wires, Fiber-film or Film-sensors. Probes are available in one, two, and three dimensional versions as single, dual and triple sensor probes referring to the number of sensors [90].

In this study, two-component velocity measurements needed to be made. This was accomplished with a dual sensor probe with two wires placed in an X-configuration as shown in Fig. 4-9. An x-probe enables simultaneous measurements of two velocity components. An x-probe hot-wire consists of two inclined wires placed close together to form an "*X*". For analysis purposes, it is

usually assumed that the two wires are contained in the same plane. AN-1003, produced by *AAA LAB SYSTEM LTD*., was used to calibrate the hot wires and to measure flow fluctuating velocities (see Fig. 4-10).

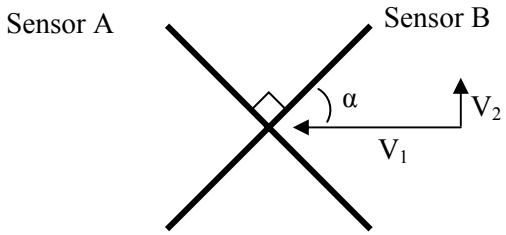

Figure 4-9. Configuration of x-probe

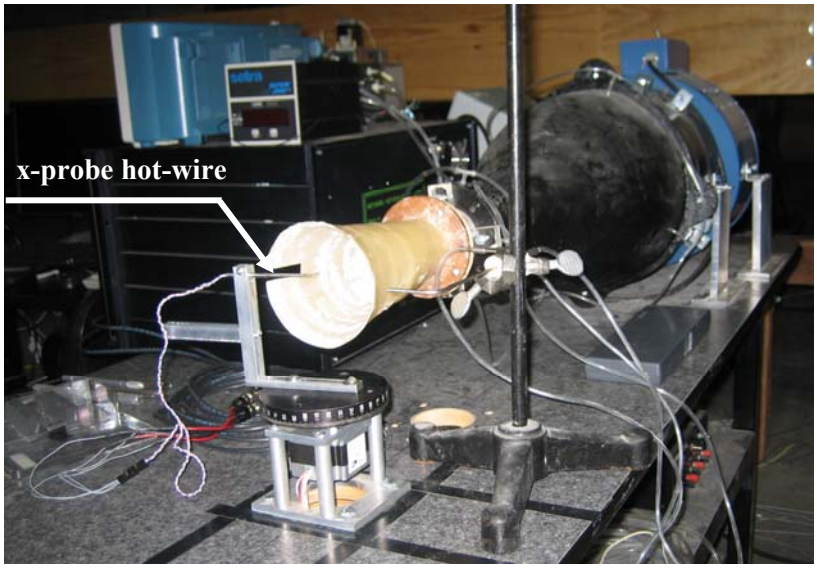

Figure 4-10. Calibration system for the x-probe hot-wire

The effective velocities $V_{A,\,eff}$ and $V_{B,\,eff}$ in the hot-wire coordinate system defined by the sensors can be written in terms of the three-components of velocity V_1, V_2 and V_3 as shown below [91]:

$$V_{A,eff}^2 = (V_1 \cdot \cos\alpha - V_2 \cdot \sin\alpha)^2 + k_T^2 (V_1 \cdot \sin\alpha + V_2 \cdot \cos\alpha)^2 + k_N^2 \cdot V_3^2 \tag{4.1}$$

$$V_{B,eff}^2 = (V_1 \cdot \sin\alpha + V_2 \cdot \cos\alpha)^2 + k_T^2 (V_1 \cdot \cos\alpha - V_2 \cdot \sin\alpha)^2 + k_N^2 \cdot V_3^2 \tag{4.2}$$

where, α = the angle between V_1 and sensor B

k_T and k_N = empirically determined factors

The coordinates are usually selected such that V_3 is zero, and k_T is zero and k_N becomes 1 if sensors are sufficiently long [91]. Then, Eqs. 4.1 and 4.2 reduce to:

$$V_{A,eff}^2 = (V_1 \cdot \cos\alpha - V_2 \cdot \sin\alpha)^2 \tag{4.3}$$

$$V_{B,eff}^2 = (V_1 \cdot \sin\alpha + V_2 \cdot \cos\alpha)^2 \tag{4.4}$$

Further, if α is 45 degrees then Eqs 4.3 and 4.4 can be re-written as:

$$V_1 = \frac{\sqrt{2}}{2} \cdot (V_{A,eff} + V_{B,eff}) \tag{4.5}$$

$$V_2 = \frac{\sqrt{2}}{2} \cdot (V_{A,eff} - V_{B,eff}) \tag{4.6}$$

The x-probe hot-wire calibration curves were used for the effective velocities in the buffeting test. In these curves, the best fit lines were determined using Excel software, and from Eqs. 4.5 and 4.6, the fluctuating wind velocities in along-win and vertical-wind directions (V_1 and V_2) can be obtained.

Gust generator

A gust generator (see Fig. 4-11) was constructed of two thin parallel airfoils linked together by a set of levers that can produce a gust with harmonic oscillations, thereby generating sinusoidal horizontal and vertical velocity components. The airfoils have a thickness of 0.75 in., a length of 12 in., and a width of 20 in. and were placed parallel to the flow direction with a 8 in. space between the two. The gust generator system was placed at an upstream distance of 6 in. from the front surface of the cylinder and could oscillate with a maximum amplitude of approximately ±6 degree to produce the wind gust. The x-probe hot-wire was placed along the centerline and upstream of the model as shown in Fig. 4-11. Figure 4-12 shows a schematic diagram for the buffeting test model setup.

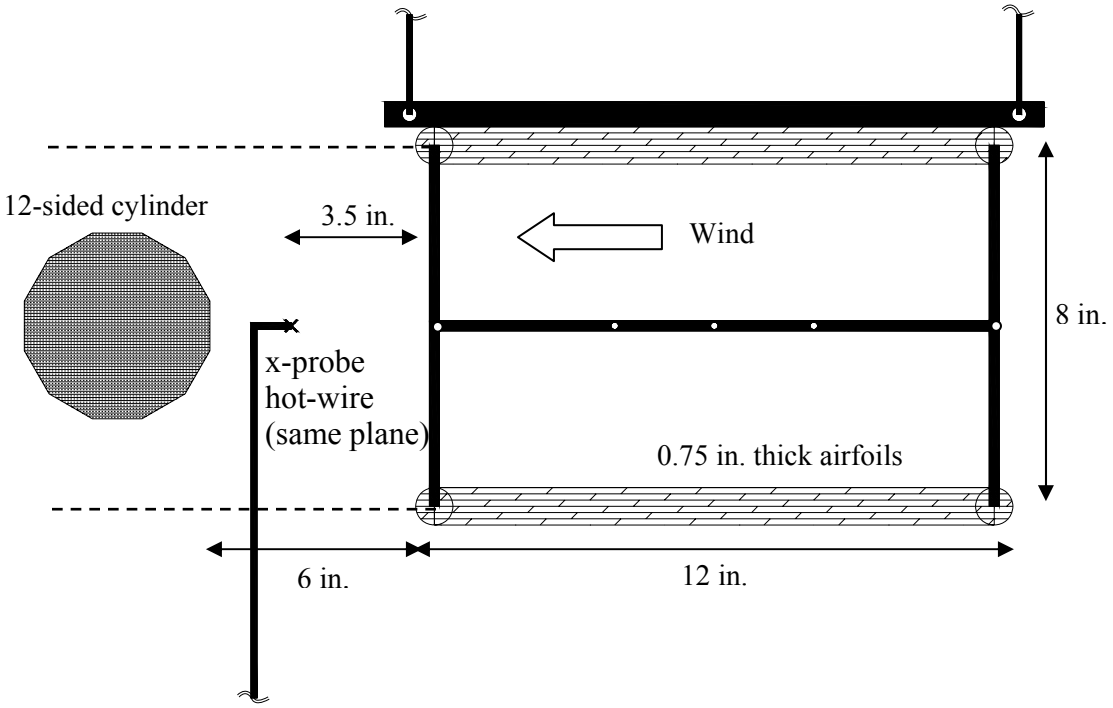

(a) Angle of attack = 0°

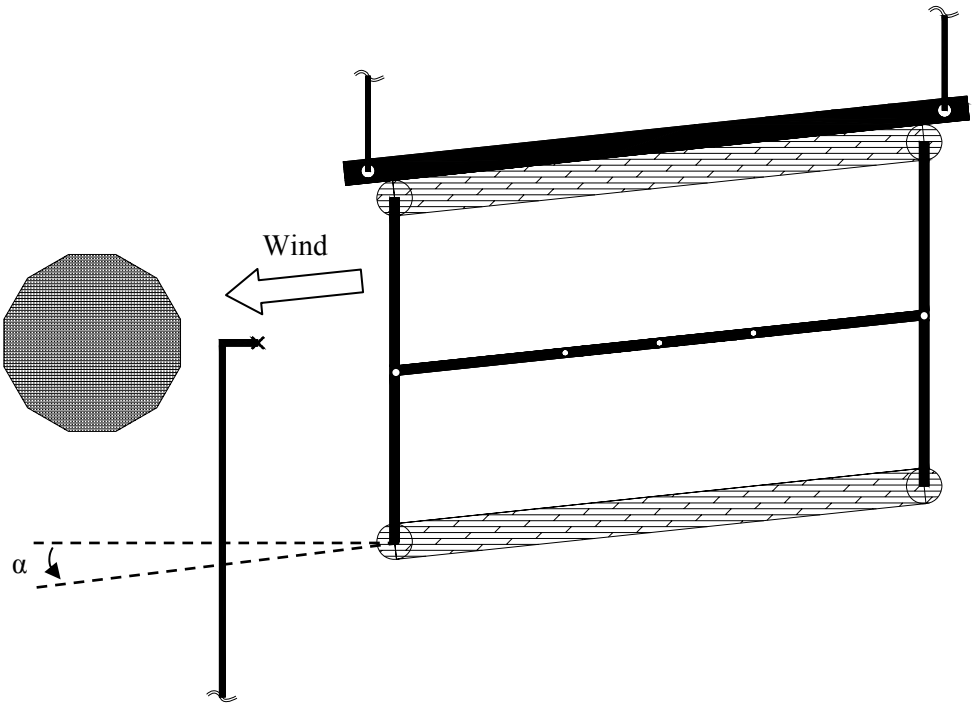

(b) $\alpha \approx +6°$

Figure 4-11. Schematic diagrams for the buffeting test

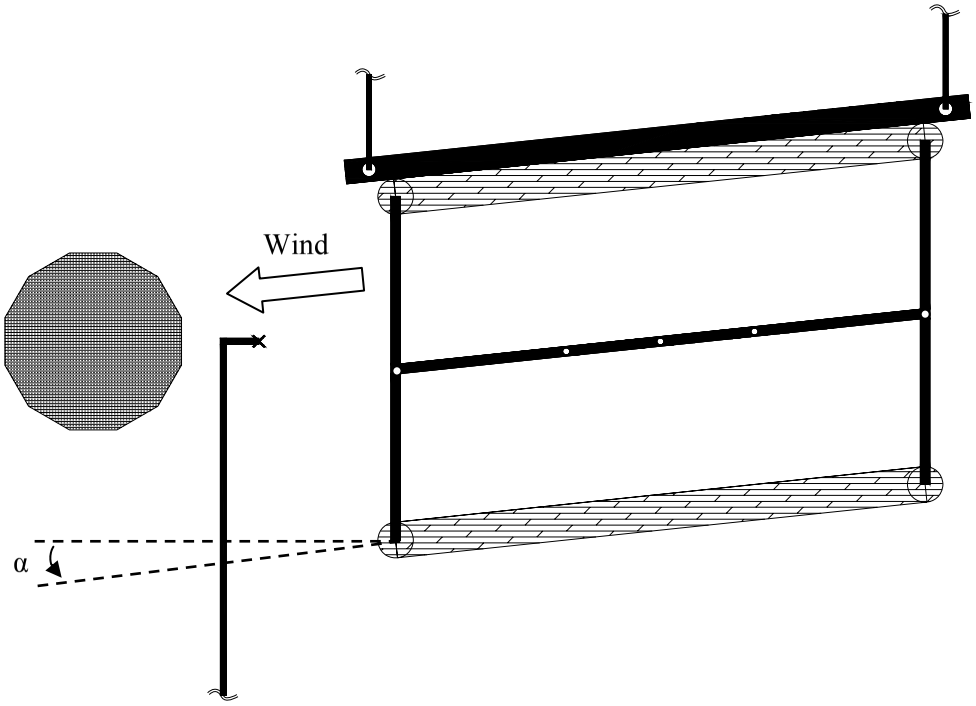

(c) α ≈ -6°

Figure 4-11. (Continued)

Force-Balance and Data Acquisition System

The force measurements are accomplished with eight force transducers (Transducer Techniques, SL 194344 to SL 194350 and SL 194352) that have a capacity of 2.5 *lb* each. Four of these were used for drag measurement and the other four force transducers were used for lift measurement.

Experimental procedure

Buffeting tests were completed to obtain the buffeting indicial function for along-wind and vertical-wind directions. The following steps describe the experimental procedure.

- Calibrate a hot-wire x-probe
- Fix the gust generator
- Fix the 12-sided model into the force balance system downstream of the gust generator
- Place the hot-wire at a proper location downstream of the gust generator
- Test the model over a range of wind speeds, increased incrementally up to the maximum force that the force transducers can record

- Record the mean and fluctuating drag and lift forces on the model and the horizontal and vertical wind velocities using the hot-wire x-probe at a fixed oscillating frequency of the gust generator
- Repeat the above for several frequencies
- Compute the power spectral density functions for the aerodynamic forces and fluctuating wind speeds
- Obtain the aerodynamic admittance functions for the drag and lift forces by comparing the power spectral density functions of the force and wind speed

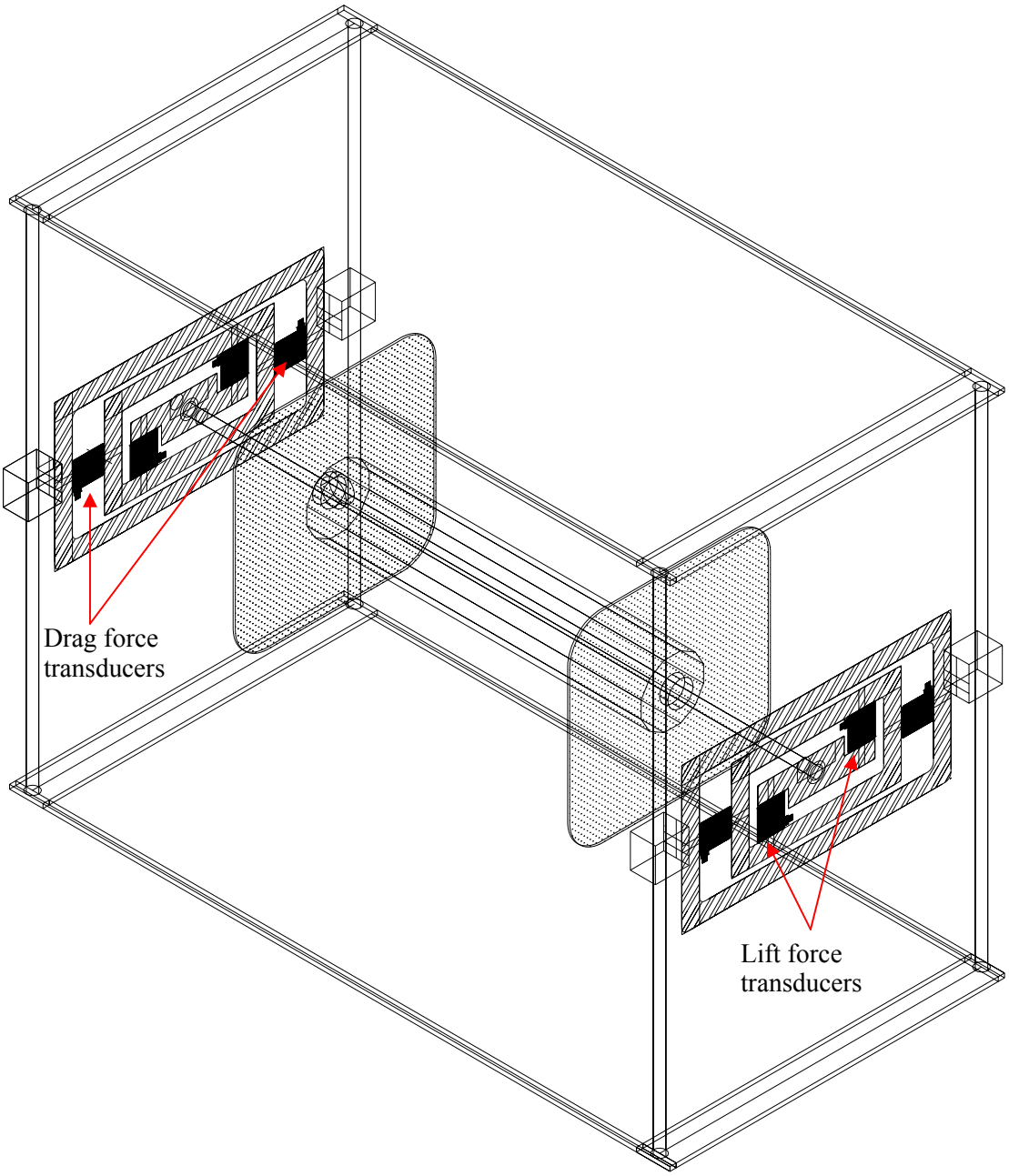

Figure 4-12. Schematic view of buffeting test

4.4. Results

From the wind tunnel tests described previously, several aerodynamic parameters were derived such as the static drag coefficient, the slope of aerodynamic lift coefficient, Strouhal number, the lock-in range of wind velocities and amplitude of vortex-induced vibration as a function of Scruton number. These parameters will be used later in the mathematical model to predict vortex-induced and buffeting induced response of the HMLP structure.

4.4.1. Static Test

The wind speeds in this test were varied from 2 ft/s to 100 ft/s to yield a range of Reynolds numbers (Re) from 2.5×10^4 to 2.3×10^5. The drag coefficient C_D can be calculated from the measured drag force and mean wind speed using the following equation.

$$C_D = \frac{F_D}{\frac{1}{2} \cdot \rho \cdot U^2 \cdot A} \tag{4.7}$$

where, F_D = drag force

ρ = air density

U = mean wind speed

A = projected area of model

To verify the force-balance system, drag coefficients for a circular cylinder was measured at several Reynolds number and compared with other references. The average difference of drag coefficient at Re between 4.0×10^4 and 1.0×10^5 was 2.3%. Figure 4-13 shows the mean drag coefficient versus Reynolds number (Re) for the uniform dodecagonal shape cylinder. In this plot, it can be observed that the mean drag coefficient (C_D) for the case of corner orientation increases until Re equals approximately 1.5×10^5 beyond which it tends to converge to 1.45. In the case of flat orientation, the C_D appears to stabilize at 1.56 at approximately the same Re. The experiments indicated that the angle of attack of the wind on the cylinder influences the drag coefficient and also show that the flat orientation results in a slightly higher C_D than that of the corner orientation at most Reynolds numbers.

According to Scruton [92], the C_D for a 12-sided polygon with flat orientation is 1.3 in the subcritical region and 1.0 in the supercritical region. James [63] also conducted several wind tunnel tests to measure drag and lift coefficients on various polygon shaped cylinders. For a 12-sided cylinder, James [63] found a constant drag coefficient, 1.4 and 1.2 for flat and corner orientations, respectively from Re 3.0×10^5 to 2.0×10^6.

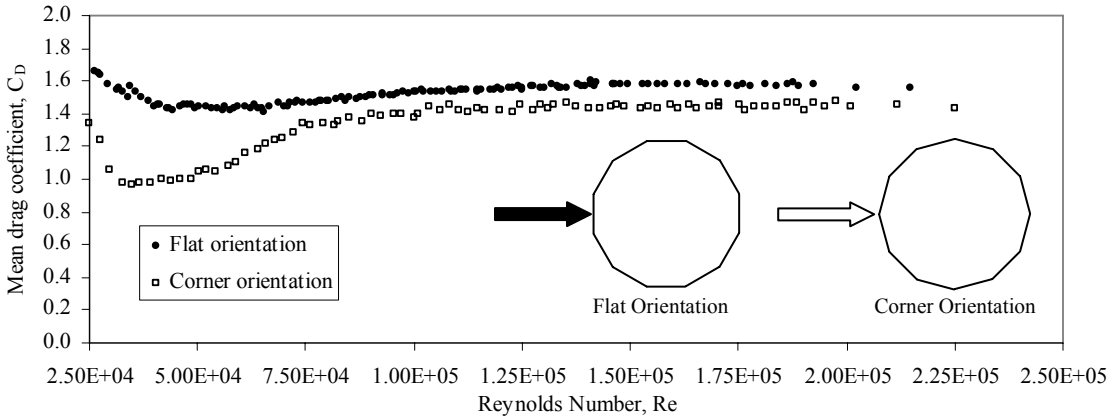

Figure 4-13. Drag coefficient (C_D) for the dodecagonal cylinder

Slope of lift coefficient

The mean lift coefficients (C_L) for various angles of attack were obtained and are shown in Fig. 4-14. The ratio of C_L and angle of attack were calculated to be approximately $-0.7 \cdot \pi$ and $0.5 \cdot \pi$ for flat and corner orientation, respectively. The Reynolds number (Re) varied from 9.3×10^4 to 1.6×10^5 in these tests. The lift coefficient C_L can be calculated from the measured lift force and mean wind speed using the following equation.

$$C_L = \frac{F_L}{\frac{1}{2} \cdot \rho \cdot U^2 \cdot A} \tag{4.8}$$

where, F_L = lift force, and other parameters are described in Eq. 4.7.

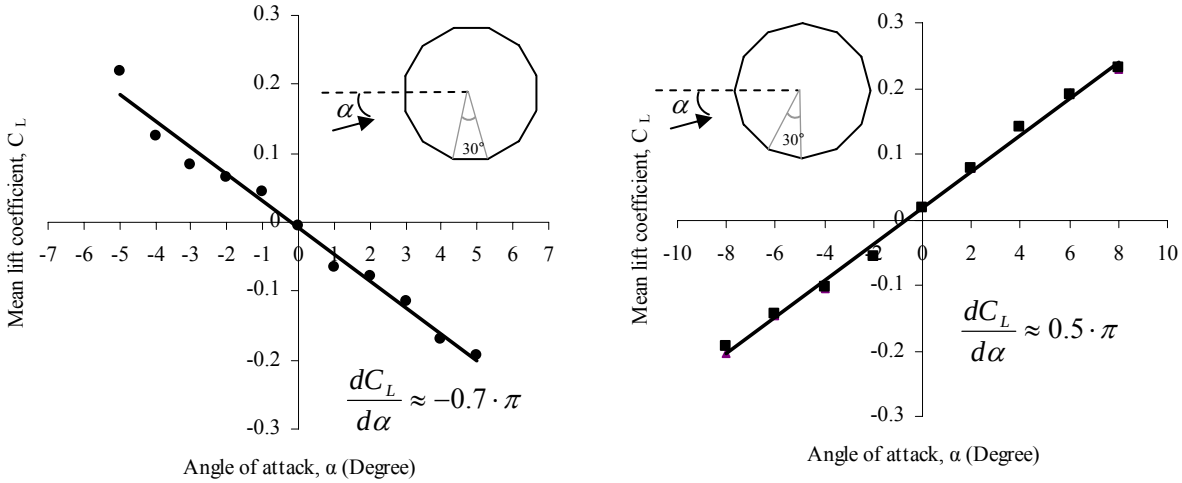

Figure 4-14. Lift coefficient (C_L) and its slope for the dodecagonal cylinder

4.4.2. Dynamic Test

A dynamic suspension system was designed to allow single degree-of-freedom vibration of the cylinder along the vertical direction (i.e, the model was free to vibrate transverse to the wind flow). The model was suspended by a set of eight linear springs, four on each side of the model. The natural frequency, damping, mass and stiffness of the system is described subsequently in this section. The tests were conducted for both the flat and the corner orientations (see Fig. 4-15).

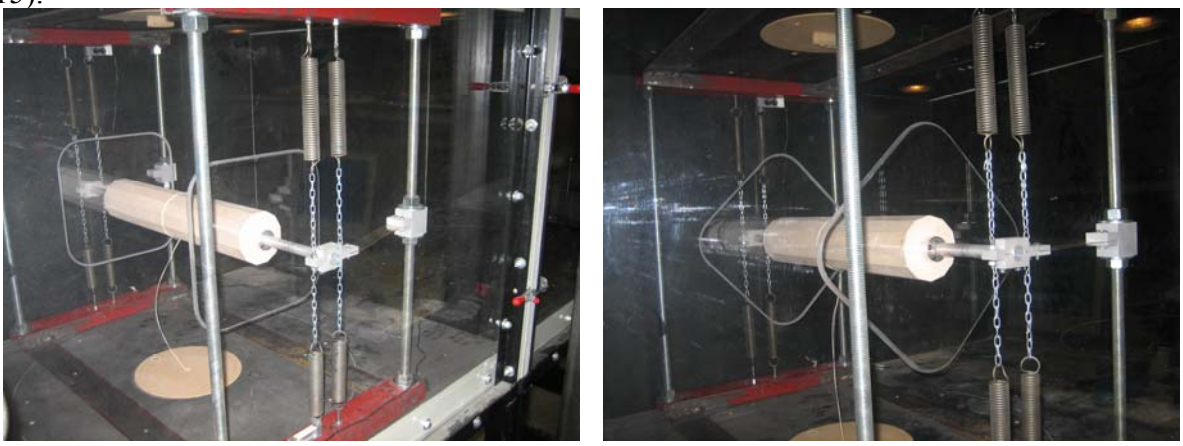

(a) Flat orientation (b) Corner orientation

Figure 4-15. Configuration of test orientation

Lock-in range and Strouhal number

The model was tested over a range of wind speeds that would produce vortex-induced vibrations. Figure 4-16 shows the response in the lock-in region of a freely vibrating cylinder. As shown in the figure, higher amplitudes were achieved when the reduced velocity is within a distinct range.

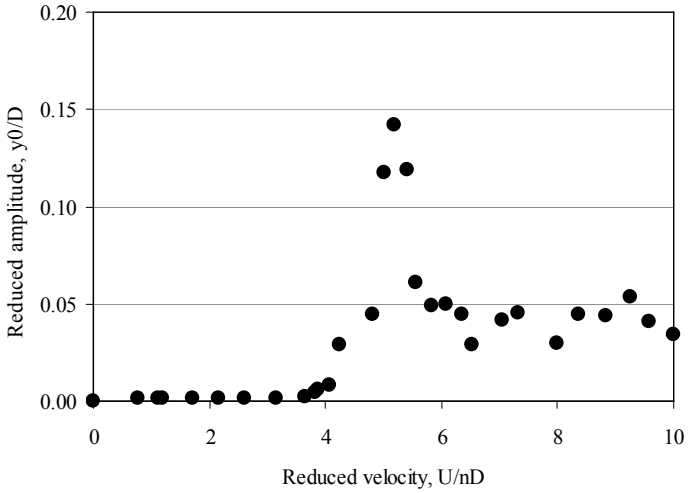

Figure 4-16. Vortex-induced vibration of a 12-sided cylinder

The lock-in range and Strouhal number ($fs \cdot D/U \approx 0.2$) are shown in Fig. 4-17. Lock-in occurs when the vortex-shedding frequency matches the natural frequency of the system which occurs at a critical wind speed and the response at the lock-in region is much larger than that at normal case. The lock-in region remains over a range of wind speeds as shown in Fig. 4-17. Hence, lock-in occurs for a reduced velocity between 5 and 7.

Figure 4-18 shows the frequency spectrum of the displacement response of the elastically supported cylinder before lock-in (a), at lock-in (b) and after lock-in (c) for the flat face orientation, where f_s and f_n are the vortex-shedding frequency and natural frequency of the cylinder, respectively. This shows that the model produces greatly amplified displacements when the vortex shedding frequency matches the natural frequency of the system.

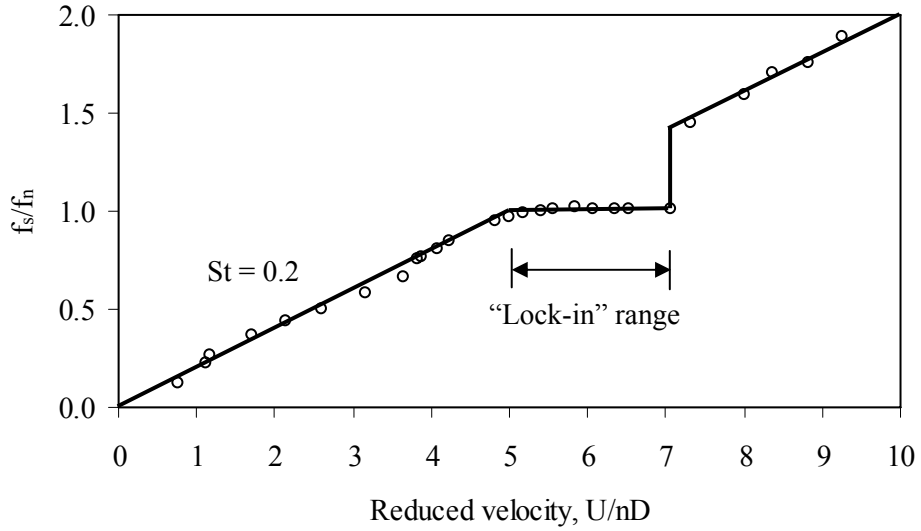

Figure 4-17. Lock-in range for the 12-sided cylinder and Strouhal number

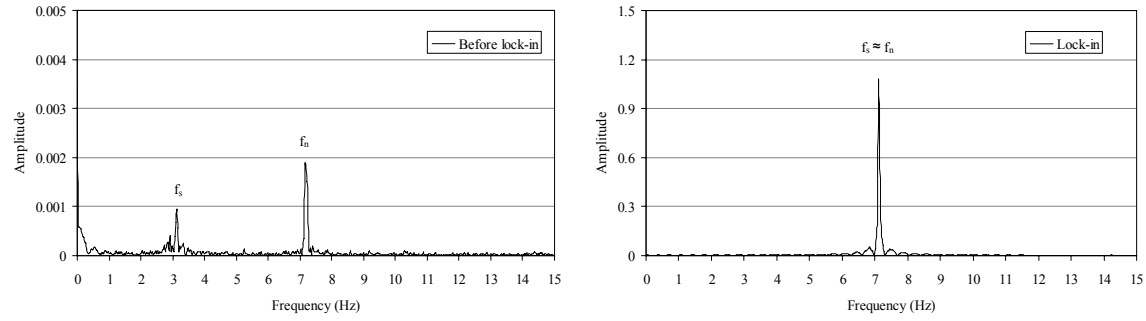

(a) before lock-in (b) at lock-in

Figure 4-18. Frequency spectra of displacement response of cylinder

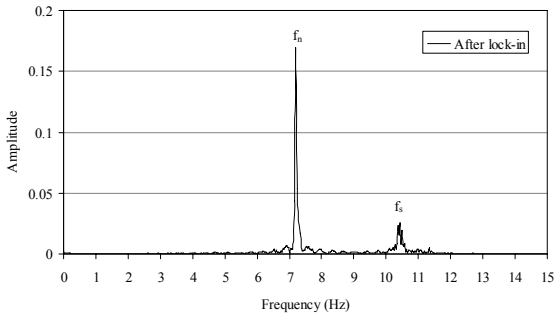

(c) after lock-in

Figure 4-18. (Continued)

Scruton number

Amplitude of the model is related to the Scruton number. In order to determine amplitude versus the Scruton number (Eq. 2.5), several parameters were required, including: the inertial mass, stiffness, natural frequency, and system damping.

$$S_c = \frac{m\zeta}{\rho D^2}, \tag{2.5}$$

where, m = mass per unit length

ζ = critical damping ratio

ρ = flow density

D = cross-wind dimension of the cross-section

The inertial mass, stiffness and natural frequency for each case were determined using the added mass method. To test multiple specimens of the model with different mass, pairs of commercially available C clamps with different weights were clamped to the previously described plastic end plates. A total of five pairs of clamps and one thin steel plate were used. The clamps and the plate were attached to the plastic end plates in opposite directions of the cylinder to avoid introducing torsion in the model. The system damping for each case was determined experimentally using the logarithmic decrement method. Figure 4.19 shows the photographs of the system for the multiple specimens with added mass using pairs of C clamps.

The system natural frequency can be expressed as,

$$\omega_n = \sqrt{\frac{k}{m}} \quad \text{or} \quad \omega_n^2 = \frac{k}{m} \quad \text{or} \quad \frac{1}{\omega_n^2} = \frac{m}{k} \tag{4.9}$$

where, ω_n = the natural frequency of the system

k and m = the system stiffness and mass, respectively

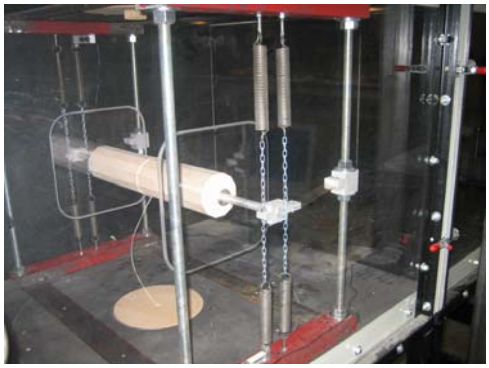

(a) Case 1: 0 lb

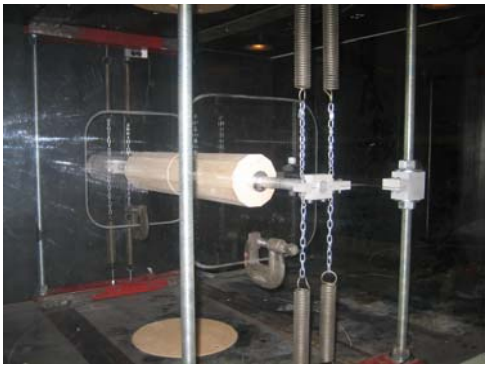

(b) Case 2: 3.6 lbs

(c) Case 3: 7.3 lbs

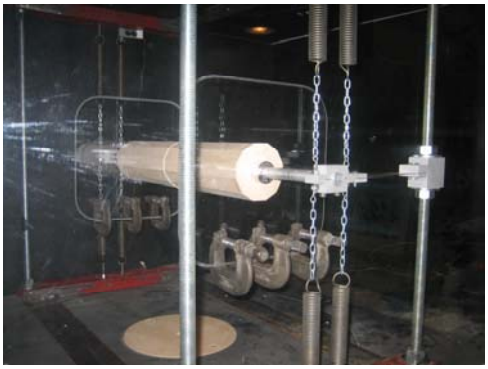

(d) Case 4: 11.2 lbs

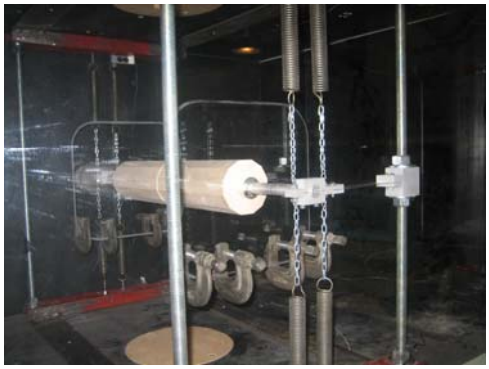

(e) Case 3: 15.4 lbs

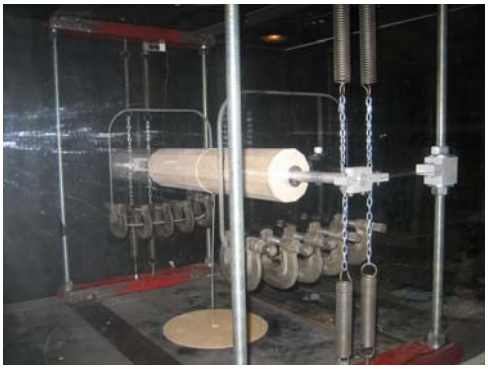

(f) Case 6: 19.7 lbs

Figure 4-19. Multiple specimens with added mass using pairs of C clamps attached to the end plates

The above equation can be expressed in terms of the added mass (M_{add}),

$$\frac{1}{\omega_i^2} = \frac{m + M_{add}}{k} \tag{4.10}$$

Table 4-1 summarizes the added mass and corresponding natural frequency and damping ratio. A plot for the added mass versus the inverse of the square of the circular frequency is shown in Fig. 4-20 along with a best-fit line. The figure shows that the inverse of the square of circular frequency is linearly proportional to the added mass. The intercept in y axis ($1/\omega_n^2$, at added mass of zero) and slope of the best fit line was determined to be 0.000504 and 0.00264, respectively. The square root of inverse of the intercept value was then determined to be 44.54 rad/sec. The stiffness of the system was calculated to be 378.77 lb/ft by inversing the slope. The inertial mass of the system (without added mass) can be obtained simply using Eq. 4.10 as 0.19 slugs. Table 4-2 lists the system frequency, stiffness and inertial mass that were calculated using the best fit line.

Note that the inertial weight of 6.15 lb is greater than the weight of the model (4.48lb) because of accessories attached to the model. The inertial mass per unot length (m) was calculated for each 'added mass' case by adding the magnitude of the added mass to the inertial mass of the 'zero added mass' case and Scruton number for each 'added mass' case was calculated (Eq. 4.10). The inertial mass per unit length damping and corresponding Scruton number for each case are listed in Table 4-1.

Scruton number (S_c) for each of added mass was calculated using Equation 2.5 and the reduced amplitude (y_0/D, maximum amplitude / diameter of the model) was obtained from the measurement when the maximum displacement occurred. The best fit line was also plotted and is shown in Fig. 4-21. The equation for the best fit line was derived similar to the empirical formula by Griffin et al. (see Eq. 2.6) for circular cylinder and expressed as:

$$\frac{y_0}{D} = \frac{1.91}{[1 + 0.72 \cdot (8 \cdot \pi^2 \cdot S_t{}^2 \cdot S_c)]^{2.45}}, \tag{4.11}$$

where, y_0 = maximum amplitude

D = cross-wind dimension of the cross-section

S_t = the Strouhal number

S_c = the Scruton number

Table 4-1. System frequencies with added mass

Weight	Added Weight		Total weight	Total mass	Frequency	Frequency	$1/\omega^2$	amping rat	Inertial mass	Sc
kg	kg	lb	lb	slugs	Hz	rad/s	s^2/rad^2	%	slugs	
2.030	0	0.00	4.48	0.14	7.151	44.93	0.000495	0.186%	0.191	0.858
3.010	0.980	2.16	6.64	0.07	6.088	38.25	0.000683	0.284%	0.258	1.776
3.672	1.642	3.62	8.10	0.11	5.637	35.42	0.000797	0.139%	0.303	1.024
4.652	2.622	5.78	10.26	0.18	5.127	32.21	0.000964	0.145%	0.370	1.303
5.359	3.329	7.34	11.82	0.23	4.781	30.04	0.001108	0.158%	0.419	1.605
6.339	4.309	9.50	13.98	0.30	4.434	27.86	0.001288	0.221%	0.486	2.606
7.101	5.071	11.18	15.66	0.35	4.209	26.45	0.001430	0.167%	0.538	2.182
8.081	6.051	13.34	17.82	0.41	3.977	24.99	0.001601	0.200%	0.605	2.941
9.024	6.994	15.42	19.90	0.48	3.781	23.75	0.001772	0.176%	0.670	2.870
10.004	7.974	17.58	22.06	0.55	3.607	22.66	0.001947	0.175%	0.737	3.140
10.957	8.927	19.68	24.16	0.61	3.459	21.73	0.002118	0.186%	0.802	3.618
11.927	9.897	21.82	26.30	0.68	3.326	20.90	0.002289	0.186%	0.869	3.925
12.807	10.777	23.76	28.24	0.74	3.217	20.21	0.002448	0.211%	0.929	4.767

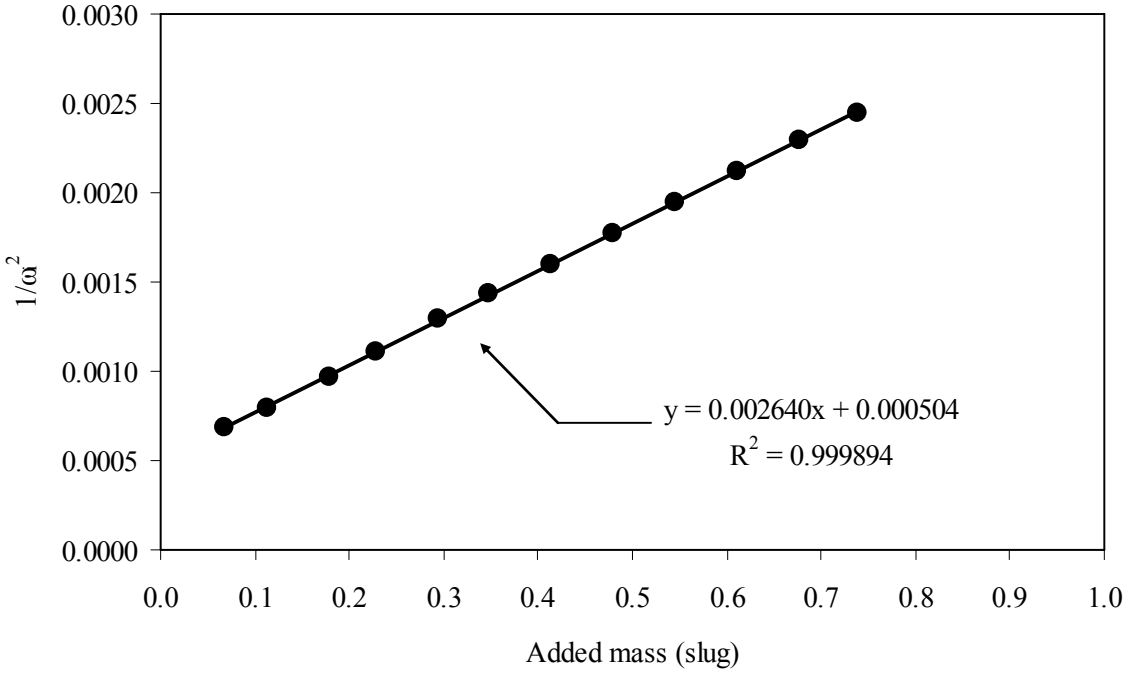

Figure 4-20. Inertial mass identification of cylinder

Table 4-2. Adjusted system frequency and mass

Frequency	**Frequency**	**Stiffness**	**Inertial mass**	**Weight**
rad/s	Hz	lb/ft	Slugs	lb
44.544	7.089	378.769	0.191	6.147

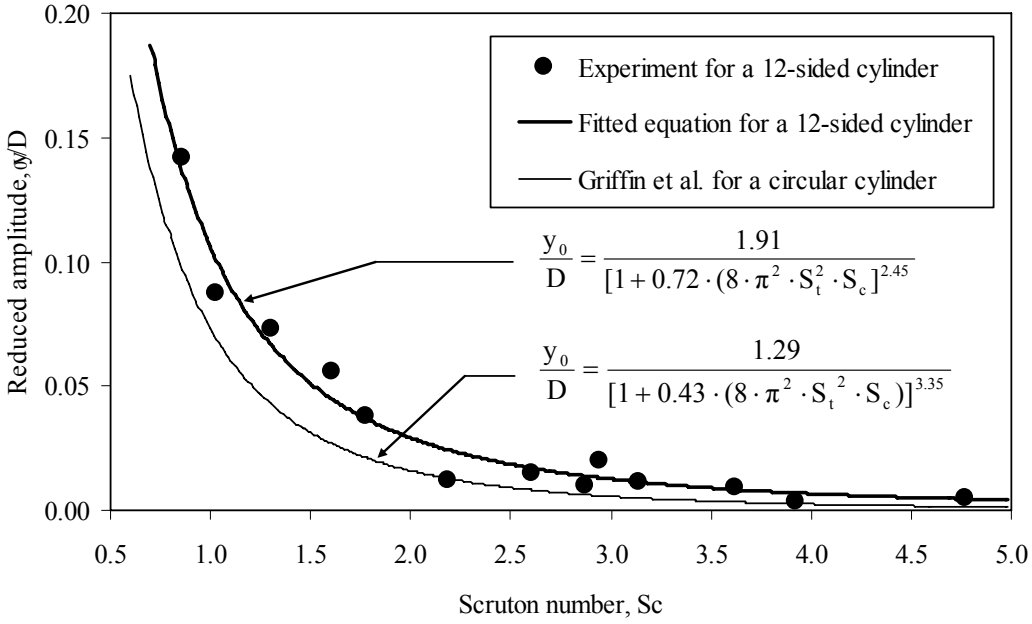

Figure 4-21. Scruton number vs. maximum amplitude for the 12-sided cylinder

4.4.3. Buffeting Test

The relationship in the frequency domain between the power spectral density of turbulence in the upstream flow and the power spectral density of fluctuating wind load that it induces on a structure can be defined in terms of an aerodynamic admittance that is a function of the reduced frequency. A similar relationship in the time domain can be defined in terms of buffeting indicial functions. Generally, these relationships need to be determined experimentally since the flow around a structure in turbulent wind is too complex to be derived analytically.

In this study, the aerodynamic admittance functions for drag and lift forces were obtained experimentally from the static wind-tunnel model tests. A hot-wire x- probe was used to obtain the horizontal and vertical wind velocity fluctuations and force transducers were used to simultaneously measure the aerodynamic lift or drag on the model. As described previously, a gust generator was fixed upstream of the model to generate a sinusoidal gust, with vertical and horizontal velocity fluctuations, at a fixed frequency. The power spectral density functions [36] for the buffeting forces in along-wind and lateral-wind directions are follows:

$$S_{F_b^x F_b^x}(n) = (\frac{1}{2} \cdot \rho \cdot U^2 \cdot A \cdot C_D)^2 \cdot \frac{4 \cdot S_{uu}(n)}{U^2} \cdot \chi_u^2(n) \tag{4.12}$$

$$S_{F_b^y F_b^y}(n) = [\frac{1}{2} \cdot \rho \cdot U^2 \cdot A \cdot (C_D + \frac{dC_L}{d\alpha})]^2 \cdot \frac{4 \cdot S_{ww}(n)}{U^2} \cdot \chi_w{}^2(n) \tag{4.13}$$

where, $S_{F_b^x F_b^x}(n)$ and $S_{F_b^y F_b^y}(n)$ = power spectral density function for the along and lateral buffeting forces, respectively

$S_{uu}(n)$ and $S_{ww}(n)$ = power spectral density function for the along and lateral-wind velocity fluctuations respectively

$\chi_u^2(n)$ and $\chi_w^2(n)$ = aerodynamic admittance function for along and lateral forces, respectively

Figure 4-22 shows the aerodynamic admittance functions calculated from the buffeting wind-tunnel tests. The frequency of the gust generator and the wind speed were both chosen to obtain a range of the reduced frequency (K) from 0.005 to 1.5. Specifically, the frequency of the gust generator ranged from approximately 0.2 to 4 Hz while the wind velocity varied approximately 5 ft/s to 65 ft/s.

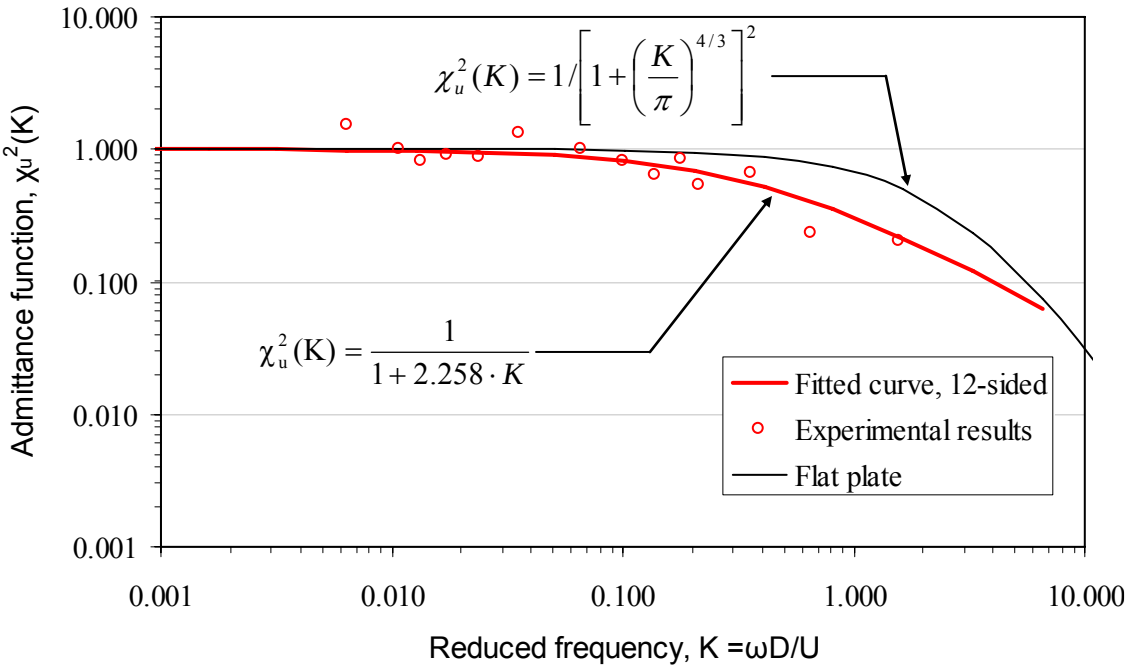

(a) Along-wind admittance function (χ_u^2)

Figure 4-22. Aerodynamic admittance functions for a dodecagonal cylinder

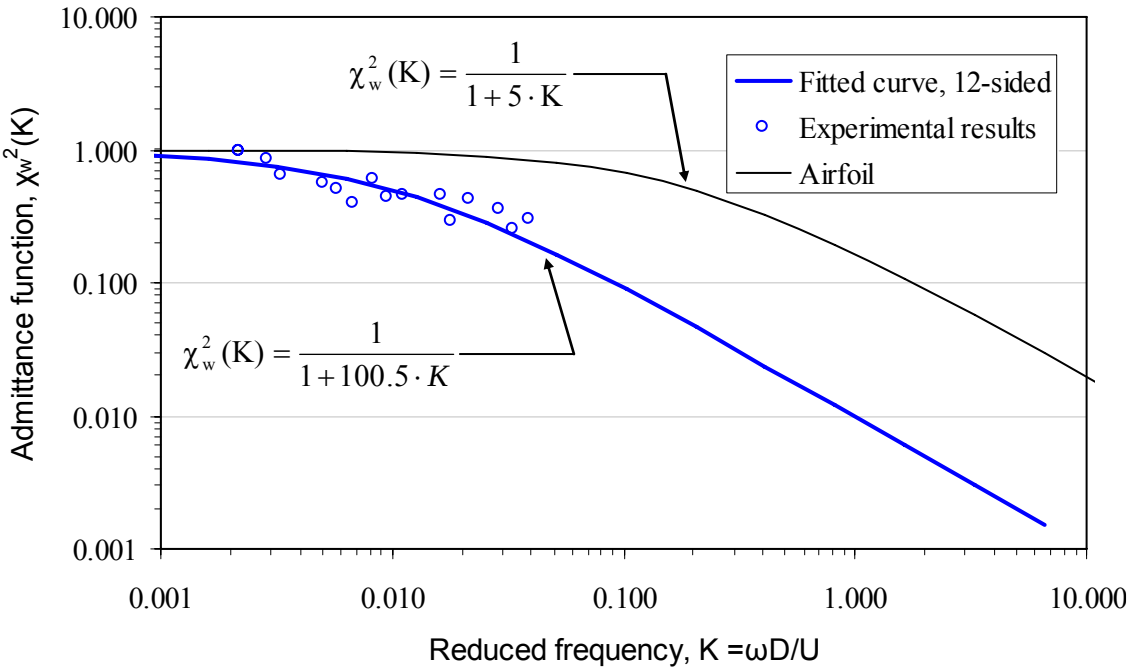

(b) Lateral-wind admittance function (χ_w^2)

Figure 4-22. (Continued)

5. TIME-DOMAIN MODELING FOR COUPLED BUFFETING AND VORTEX-SHEDDING INDUCED RESPONSE

Various aerodynamic parameters from wind tunnel testing were used to develop the time-domain mathematical model which is discussed in this chapter. The coupled buffeting and vortex-shedding induced response of the HMLP as predicted by the time-domain model is compared with the data from long-term monitoring.

5.1. Identification of Buffeting Indicial Function from Admittance Function

The relationship between fluctuating wind velocity in the upstream flow and fluctuating wind load that it induces on a structure is commonly referred to as "Aerodynamic Admittance" [39]. The relationship in the frequency domain between the power spectral density of turbulence in the upstream flow and power spectral density of fluctuating wind load that it induces on a structure can be defined in terms of an aerodynamic admittance that is a function of the reduced frequency. A similar relationship in the time domain can be defined in terms of buffeting indicial functions.

An expression, known as Sears' function (see Eq. 2.7), for the aerodynamic admittance of a thin symmetrical airfoil was theoretically derived by Sears [41], and Liepmann [42] suggested a somewhat simpler expression (see in Eq. 2.8). Jancauskas [43 and 44] verified the Sears' theoretical plot experimentally for an airfoil and gave a simple approximate expression (see Fig. 2-8) as defined in Eq. 5.1. The approximate form of aerodynamic admittance function for lift force, $\chi_w^2(\mathrm{K})$, on an airfoil is given as follows [46]:

$$\chi_w^2(\mathrm{K}) = \frac{1}{1+5\cdot K} = \left|\Phi(K)\right|^2 \tag{5.1}$$

where, K = reduced frequency = $n\cdot\pi\cdot c / U$

c = chord length of an airfoil

U = mean wind velocity

$\Phi(K)$ = Sears' function

The Sears' function and the derivative of the buffeting indicial function for lift force with respect to 's', $\phi_w'(s) = A_1\cdot e^{-A_2\cdot s} + A_3\cdot e^{-A_4\cdot s}$, where A_1 to A_4 are constants, and 's' is non-dimensional time defined as $U\cdot t/c$, are related by Fourier Transform. The Sears' function can be expressed in terms of a complex form as follows:

$$\Phi(K) = \int_0^\infty \phi_w'(\sigma)\cdot e^{-i\cdot K\cdot\sigma}\cdot d\sigma = \left(\frac{A_1\cdot K}{A_2^2+K^2} + \frac{A_3\cdot K}{A_4^2+K^2}\right) - i\cdot\left(\frac{A_1\cdot A_2}{A_2^2+K^2} + \frac{A_3\cdot A_4}{A_4^2+K^2}\right) \tag{5.2}$$

Thus, the following relationship can be shown using Eqs. 5.1 and 5.2 as:

$$\chi_w^2(K) = \frac{1}{1+5\cdot K} = \left|\Phi(K)\right|^2 = \left(\frac{A_1\cdot K}{A_2^2+K^2} + \frac{A_3\cdot K}{A_4^2+K^2}\right)^2 + \left(\frac{A_1\cdot A_2}{A_2^2+K^2} + \frac{A_3\cdot A_4}{A_4^2+K^2}\right)^2 \tag{5.3}$$

Commercially available software, Origin, was used to find the constants $A_1 - A_4$ which satisfy Eq. 5.3. The constants A_1 to A_4 were determined as: $A_1 = 0.053$, $A_2 = 0.122$, $A_3 = 0.515$ and $A_4 = 0.972$. The derivative of the buffeting indicial function as derived here for an airfoil lift force matches closely with the derivative of Küssner function (see Eq. 5.4) [46] validating the procedure used here to identify the constants. The aerodynamic admittance for drag force on a flat plate was shown in Eg. 2.9. Based on the same numerical procedure as above, the derivative of buffeting indicial function for drag force on a flat plate can expressed in Eq. 5.5.

$$\phi_w'(s) = 0.065\cdot e^{-0.130\cdot s} + 0.500\cdot e^{-s} \tag{5.4}$$

$$\phi_u'(s) = 0.075\cdot e^{-0.513\cdot s} + 1.794\cdot e^{-2.111\cdot s} \tag{5.5}$$

The same numerical procedure can be applied to the measured admittance functions for lift and drag forces can be used to obtain $\phi_w'(s)$ and $\phi_u'(s)$ for the dodecagonal cylindrical section so that these functions can be used to predict buffeting response of HMLP outlined later in Section 5.4.

5.2. The Derivative of Buffeting Indicial Function for a Dodecagonal Cross Section

Aerodynamic admittance functions were defined earlier in Section 4.4.3. The derivative of buffeting indicial function for a dodecagonal cross section can be derived based on the procedure discussed in Section 5.1.1. Thus, the following relationships similar to Eq. 5.3 can be derived from the aerodynamic admittance function of this shape as derived in Ch. 4.:

$$\chi_u^2(K) = \frac{1}{1+2.258\cdot K} = \left(\frac{A_1\cdot K}{A_2^2+K^2} + \frac{A_3\cdot K}{A_4^2+K^2}\right)^2 + \left(\frac{A_1\cdot A_2}{A_2^2+K^2} + \frac{A_3\cdot A_4}{A_4^2+K^2}\right)^2 \tag{5.6}$$

$$\chi_w^2(K) = \frac{1}{1+100.5\cdot K} = \left(\frac{A_1\cdot K}{A_2^2+K^2} + \frac{A_3\cdot K}{A_4^2+K^2}\right)^2 + \left(\frac{A_1\cdot A_2}{A_2^2+K^2} + \frac{A_3\cdot A_4}{A_4^2+K^2}\right)^2 \tag{5.7}$$

The constants A_1 to A_4 in Eq. 5.6 were determined as: $A_1 = 0.060$, $A_2 = 0.183$, $A_3 = 0.85$ and $A_4 = 1.309$ for drag force. For lift force, the constants A_1 to A_4 in Eq. 5.7 were determined as: $A_1 = 0.0086$, $A_2 = 0.0124$, $A_3 = 0.0695$ and $A_4 = 0.2563$. If a third-order exponential decay function of the buffeting indicial function is used instead a more accurate form of the function could be derived.

The second-order and third-order forms of the exponential decay function used to model the derivative of buffeting indicial functions for drag and lift forces on a dodecagonal cylinder are compared as follows:

$$\phi_u'(s) = 0.060 \cdot e^{-0.183 \cdot s} + 0.850 \cdot e^{-1.309 \cdot s} \tag{5.8a}$$

or

$$\phi_u'(s) = 0.007 \cdot e^{-0.062 \cdot s} + 0.943 \cdot e^{-1.788 \cdot s} + 0.123 \cdot e^{-0.346 \cdot s} \tag{5.8b}$$

$$\phi_w'(s) = 0.009 \cdot e^{-0.012 \cdot s} + 0.069 \cdot e^{-0.256 \cdot s} \tag{5.9a}$$

or

$$\phi_w'(s) = 0.0042 \cdot e^{-0.0075 \cdot s} + 0.1002 \cdot e^{-0.7613 \cdot s} + 0.0201 \cdot e^{-0.0639 \cdot s} \tag{5.9b}$$

Figure 5-1 shows that the magnitude of the complex third-order exponential decay functions more closely match the original admittance functions used to derive the indicial functions.

5.3. Simulation of Turbulent Wind Velocity

The turbulence components of wind velocity in along-wind (u) and lateral-wind (w) directions can be generated at *m* number of locations along the height of the HMLP using wind velocity spectral density functions [93 and 94] using Eq. 5.10.

$$u_i(\mathrm{t}) \text{ or } \mathrm{w}_i(\mathrm{t}) = \sum_{l=1}^{m} \sum_{k=1}^{N} \left| H_{il}(\omega_k) \right| \sqrt{2\Delta\omega_k} \cdot \cos[\omega_k t + \theta_{il}(\omega_k) + \phi_{lk}] \quad \text{for i} = 1, 2, .., \mathrm{m} \tag{5.10}$$

where,

H_{il} = the (i, l) entry of the matrix H which satisfies wind spectrum, $S = H \cdot \overline{H}^T$

$\overline{H}^T$ = the matrix transposition of the complex conjugate of H

$\Delta\omega_k$ = the chosen frequency intervals

$\theta_{il}(\omega_k) = \tan^{-1}[\mathrm{Im}\{H_{il}(\omega_k)\} / \mathrm{Re}\{H_{il}(\omega_k)\}]$

$\mathrm{Im}\{H_{il}(\omega_k)\}$ = the imaginary component of $H_{il}(\omega_k)$

$\mathrm{Re}\{H_{il}(\omega_k)\}$ = the real component of $H_{il}(\omega_k)$

ϕ_{lk} = the random phase angles from its unit uniform distribution between 0 and 2π ($l = 1, 2, \ldots, m$; $k = 1, 2, \ldots, N$)

N = the number of discrete frequencies ω_k , over the range of the wind spectrum

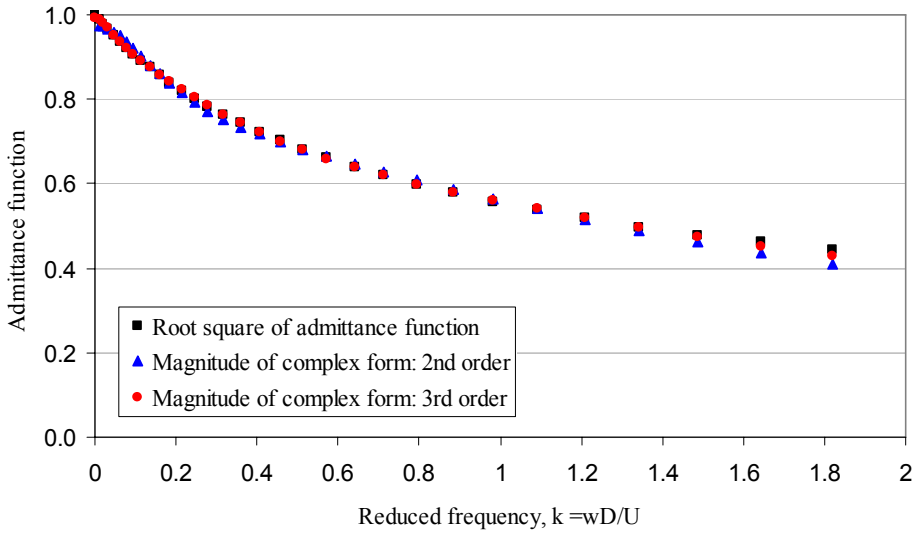

(a) Drag force

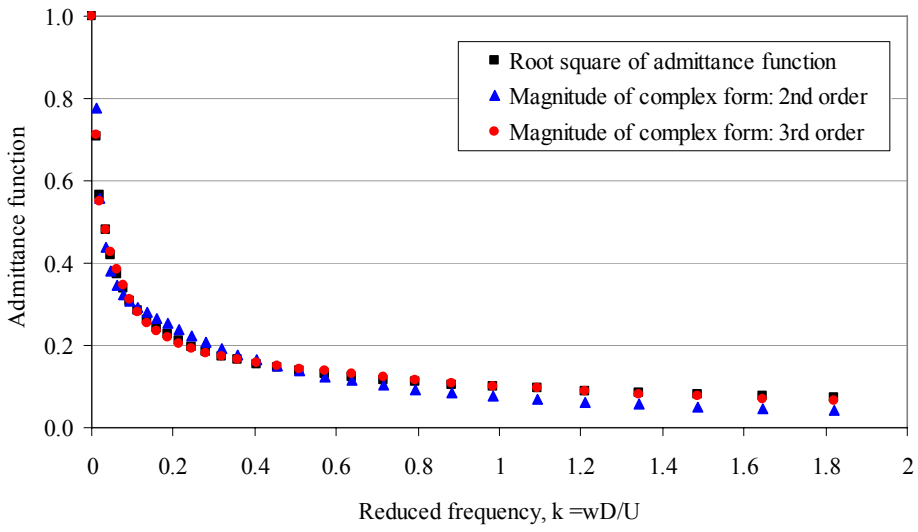

(b) Lift force

Figure 5-1. Admittance function

Samples of time histories generated by Eq. 5.10 are presented in Figs. 5-2 and 5-3. The turbulence intensities at 33ft for both along-wind and lateral-wind directions were determined to be approximately 14% from long-term monitoring data (see Ch. 3). The empirical equations for wind turbulence power spectral density (Eqs. 5.11a and 5.11b) mentioned in Simiu and Scanlan [39] were used for the simulation. The following variables or parameters were also considered for the simulation: U(Z) from Eq. 3.2, $I_u(Z)$ and $I_w(Z)$ from Eq. 3.3 (exposure coefficient, c = 0.14 for both directions), $\beta = 6.0$, exponential decay coefficients used for co-spectra $C_z = 10$ and 6.67 for along-wind and lateral-wind direction, respectively (see Eq 5.12) [39], time increment $\Delta t = 0.1$s, maximum simulated time $T_{max} = 60$s, frequency increment $\Delta f = 0.1$Hz, maximum frequency $f_{max} = 12$Hz.

$$\frac{n \cdot S_{uu}(z,n)}{u_*^2} = \frac{200 f}{(1+50 f)^{5/3}} \tag{5.11a}$$

$$\frac{n \cdot S_{ww}(z,n)}{u_*^2} = \frac{15 f}{(1+9.5 f)^{5/3}} \tag{5.11b}$$

where,

n = frequency

$S_{uu}(z,n)$ and $S_{ww}(z,n)$ = wind turbulence power spectral density functions in along-wind and lateral-wind directions, respectively

u_*^2 =square of friction velocity = $\frac{I^2 \cdot U^2}{\beta}$

I = turbulence intensity

U = mean wind speed

β = independent wind parameter ≈ 6 for open terrain

f = reduced frequency = $\frac{n \cdot z}{U}$

z = elevation from ground

$$S_{ij}(n) = \sqrt{S_i(n) \cdot S_j(n)} \cdot Coh_{ij}(n) \tag{5.12}$$

where,

$S_{ij}(n)$ = cross-spectra between two points i and j

$S_i(n)$ and $S_j(n)$ = wind turbulence power spectral density functions in along-wind and lateral-wind directions at specific height i and j, respectively

$Coh_{ij}(n)$ = square root of the coherence function = $e^{-\hat{f}}$

$\hat{f}$ = decay variable = $\dfrac{n \cdot C_z \cdot |z_1 - z_2|}{\frac{1}{2}[U(z_1) + U(z_2)]}$

C_z = exponential decay coefficient

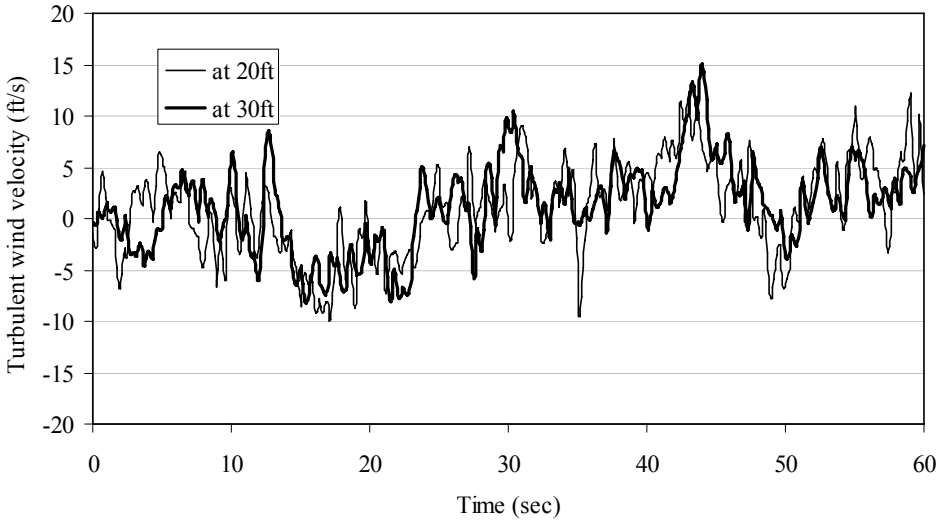

(a) at 20ft and 30ft

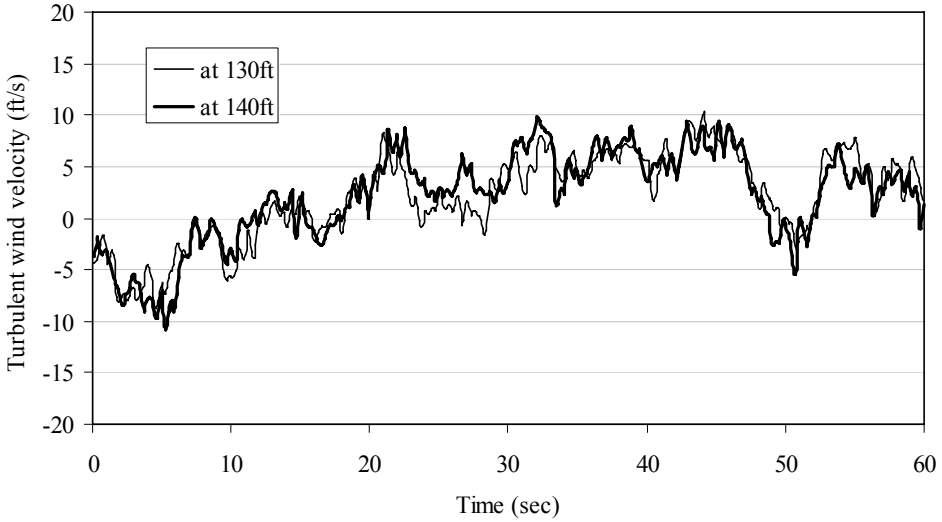

(b) at 130ft and 140ft

Figure 5-2. Simulated turbulent wind velocity in along-wind direction at a mean wind speed of 35 ft/s

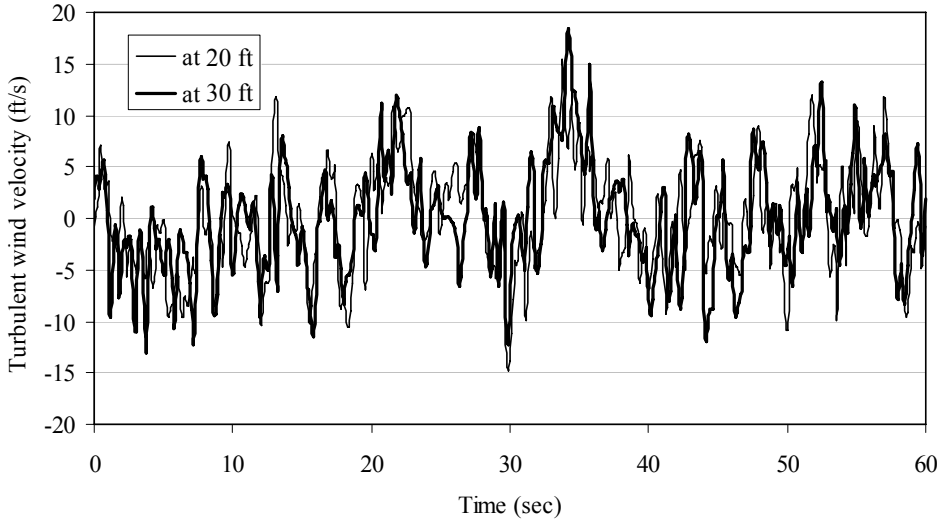

(a) at 20ft and 30ft

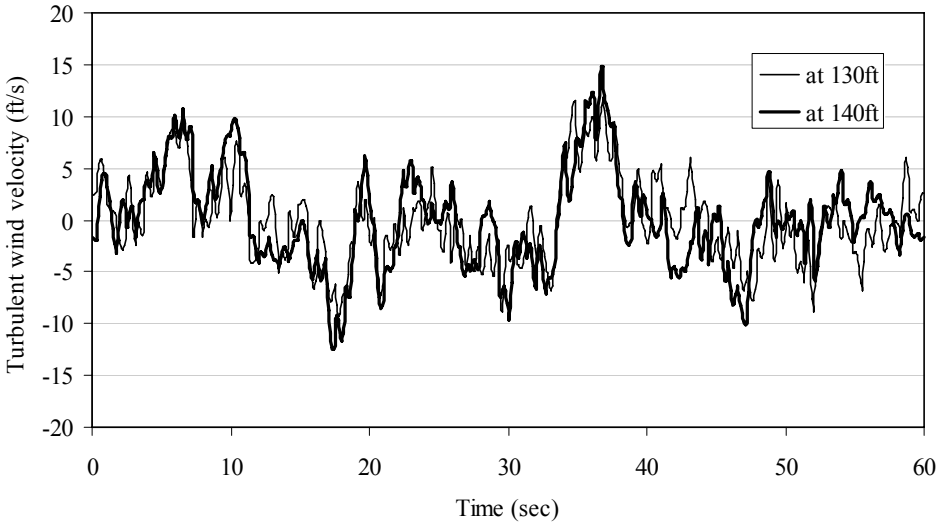

(b) at 130ft and 140ft

Figure 5-3. Simulated turbulent wind velocity in lateral-wind direction at a mean wind speed of 35 ft/s

5.4. Response of HMLP

Figure 5-4 shows the aerodynamic forces on a slender support structure at height z. Based on the quasi-steady theory, the buffeting forces are simply related to the wind velocity fluctuations. However, these forces per unit length of the structure can be expressed in terms of the aerodynamic admittance functions since the quasi-steady theory does not hold in practice.

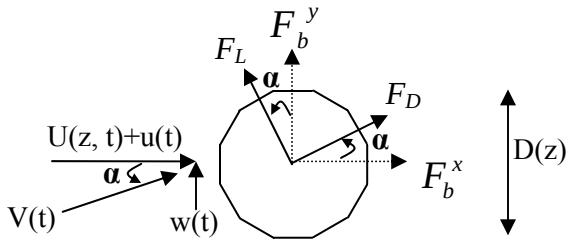

Figure 5-4. Aerodynamic forces on a slender support structure at height z

$$F_b^x(t) = \frac{1}{2}\cdot\rho\cdot U^2\cdot D\cdot C_D\cdot\frac{2u(t)}{U}\cdot\chi_u(n) \tag{5.13a}$$

$$F_b^y(t) = -\frac{1}{2}\cdot\rho\cdot U^2\cdot D\cdot(C_D + C_L^{'})\cdot\frac{w(t)}{U}\cdot\chi_w(n) \tag{5.13b}$$

where, $u(t)$ and $w(t)$ = the wind velocity fluctuations in the along-wind and across-wind directions, respectively.

$\chi_u^2(n)$ and $\chi_w^2(n)$ = the aerodynamic admittance functions for drag and lift forces, respectively.

$C_L^{'}$ = $dC_L/d\alpha$, α is angle of attack (Fig. 5-4)

The power spectral density functions for the buffeting forces in along-wind and cross-wind directions were derived and shown earlier in Eqs. 4.12 and 4.13. In time domain, the same buffeting forces in terms of non-dimensional time s = U·t/D can be expressed as follows:

$$F_b^x(s) = \rho\cdot U\cdot D\cdot C_D\cdot\int_0^s[u(\sigma)\cdot\phi_u^{'}(s-\sigma)]\cdot d\sigma \tag{5.14a}$$

$$F_b^y(s) = -\frac{1}{2}\cdot\rho\cdot U\cdot D\cdot(C_D + C_L^{'})\cdot\int_0^s[w(\sigma)\cdot\phi_w^{'}(s-\sigma)]\cdot d\sigma \tag{5.14b}$$

where, $\phi_u^{'}(s)$ and $\phi_w^{'}(s)$ = derivatives of buffeting indicial functions, $\phi_u(s)$ and $\phi_w(s)$, respectively

5.4.1. Along-Wind Response

For the along-wind response of the HMLP, it has become conventional to separate the time-dependant force into self-excited component (se) influenced primarily by the mean speed of the incoming flow and buffeting (b) component due to the turbulence in the incoming wind flow. Thus, the drag force per unit length could be represented as the sum of a self-excited component and a buffeting component:

$$F^x = F_{se}^x + F_b^x \tag{5.15}$$

The buffeting force component in along-wind direction can be expressed as in Eq. 5.14a while the self-excited component can be expressed using a flutter derivative [95]:

$$F_{se}^x(t) = \frac{1}{2} \cdot \rho \cdot U^2 \cdot D \cdot [K \cdot P_1^* \cdot \frac{\dot{y}}{U}] \tag{5.16}$$

where, K = the reduced frequency = $\omega \cdot D/U$

P_1^* = non-dimensional function of reduced frequency or reduced velocity known as flutter derivative = $-2C_D/K$ in Quasi-steady form as used here

Thus, the along-wind response for the HMLP can be calculated using Eq. 5-17.

$$\ddot{q}_i(t) + 2\zeta_i \omega_i \dot{q}_i(t) + \omega_i^2 q_i(t) = \frac{\int_0^L \phi_i^x(z) \cdot F^x(z,t) \cdot dz}{M_i}, i = 1,2,3,... \tag{5.17}$$

where, q_i = generalized coordinate in along-wind direction in i^{th} mode

ζ_i = damping ratio in i^{th} mode

ω_i = circular frequency in i^{th} mode

$\phi_i^x(z)$ = x component of normalized i^{th} mode

M_i = generalized mass in i^{th} mode

F^x = distributed x component drag force

x(z,t) = along-wind response = $\sum_{i=1}^{N} \phi_i^x(z) \cdot q_i(t)$

Figure 5-5 shows the maximum values of the stress-range for response in along-wind direction as simulated for a period of 60 seconds for wind speed varying from 5ft/s to 55ft/s in increments of 10ft/s. As shown in this figure, the simulated stress range seems to be proportional to the square of the mean wind speed and generally compares well with the mean field data at most wind speeds. It certainly falls within the envelope of ±3 times the standard deviation (σ) of the raw data from the mean stress range at each wind speed as shown by dotted lines in Fig. 5-5.

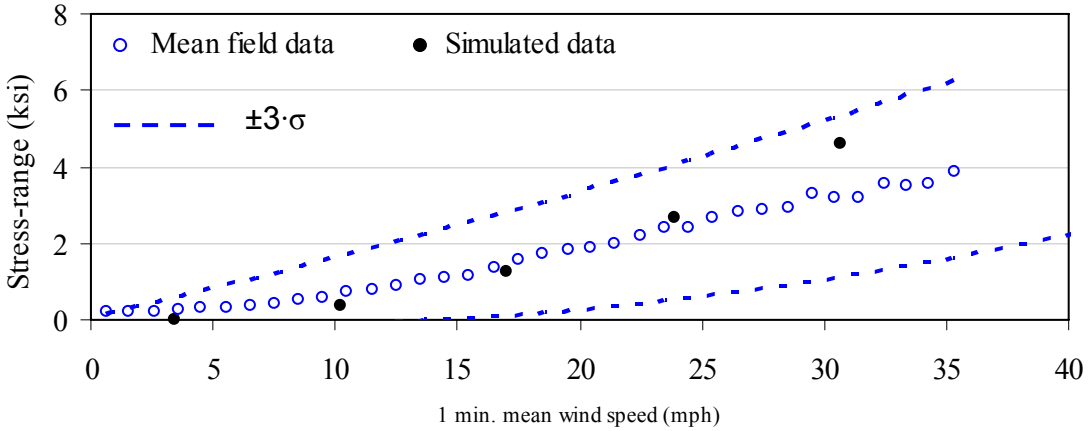

Figure 5-5. Simulated stress-range in along-wind direction

5.4.2. Across-Wind Response

For across-wind response of the HMLP, it is conventional to separate the force into self-excited (se), buffeting (b) and vortex shedding (v) components as given below:

$$F^{y} = F_{se}^{y} + F_{b}^{y} + F_{v}^{y} \tag{5.18}$$

The buffeting component in lateral-wind direction is expressed as in Eq. 5.14b while the self-excited component can be expressed using a flutter derivative [95]:

$$F_{se}^{y}(t) = \frac{1}{2} \cdot \rho \cdot U^{2} \cdot D \cdot [K \cdot H_{1}^{*} \cdot \frac{\dot{y}}{U}] \tag{5.19}$$

where, K = the reduced frequency = $\omega \cdot D/U$

H_1^* = non-dimensional function of reduced frequency or reduced velocity known as flutter derivative = $-(C_D+C_L')/K$ in Quasi-steady form as used here

Scanlan's Van-der Pole Oscillator model [39] was used for calculating the vortex-shedding force.

$$F_{v}^{y}(t) = \frac{1}{2} \cdot \rho \cdot U^{2} \cdot D \cdot \left[Y_{1} \cdot (1 - \varepsilon \cdot \frac{y^{2}}{D^{2}}) \cdot \frac{\dot{y}}{U} + Y_{2} \cdot \frac{y}{D} + \widetilde{C}_{L} \cdot \sin(\omega_{n} \cdot t + \phi) \right] \tag{5.20}$$

where, Y_1 and ε = self-exited damping parameters

Y_2 = linear aeroelastic stiffness parameter

$\widetilde{C}_L$ = rms of lift coefficient

$(\dot{})$ = derivative with respect to time

Y_1, ε, Y_2, and $\widetilde{C}_L$ are aerodynamic functions of reduced frequency, K at lock-in wind speeds and Y_2 and $\widetilde{C}_L$ were ignored here since these have negligible effects on the response [39]. The aerodynamic damping parameters, Y_1 and ε are functions of Scruton number (see Fig. 5-6) during "lock-in". These were extracted from wind tunnel experimental observations of steady-state amplitudes of the model at "lock-in" based on Eq. 5.21 [39].

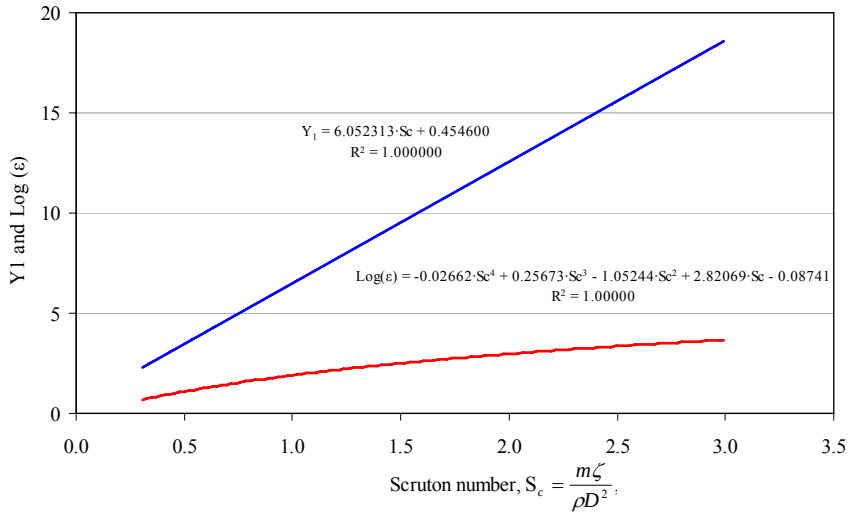

Figure 5-6. Aerodynamic damping parameters during "lock-in"

$$\frac{y_0}{D} = 2\left[\frac{Y_1 - 8\pi \cdot S_c \cdot S_t}{\varepsilon \cdot Y_1}\right]^{1/2} \tag{5.21}$$

where, $\frac{y_0}{D}$ = reduced amplitude

S_c = Scruton number $= \frac{m\zeta}{\rho D^2}$,

m = mass per unit length

ζ = damping ratio

ρ = flow density

D = cross-wind dimension of the cross-section

S_t = Strouhal number = $\frac{f_s \cdot D}{U}$,

f_s = vortex-shedding frequency

U = mean wind speed

The across-wind response for HMLP can be expressed as:

$$\ddot{r}_i(t) + 2\zeta_i \omega_i \dot{r}_i(t) + \omega_i^2 r_i(t) = \frac{\int_0^L \phi_i^y(z) \cdot F^x(z,t) \cdot dz}{M_i}, i = 1,2,3,... \quad (5.22)$$

where, r_i = generalized coordinate in across-wind direction in i^{th} mode

$\phi_i^y(z)$ = y component of the normalized i^{th} mode shape

y(z,t) = across-wind response = $\sum_{i=1}^{N} \phi_i^y(z) \cdot r_i(t)$

Once the self-excited and vortex shedding components are transferred to the left side of Eq. 5.22, the equation of motion can be written as:

$$\ddot{r}_i(t) + 2\omega_i \dot{r}_i(t)[\zeta_i + \zeta_i^{a,se} + \zeta_i^{a,v1} + \zeta_i^{a,v2}] + \omega_i^2 r_i(t) = \frac{\int_0^L \phi_i^y(z) \cdot F_b^y(z,t) \cdot dz}{M_i}, i = 1,2,.. \quad (5.23)$$

where, ζ_i = structural damping

$\zeta_i^{a,se}$ = self-excited induced damping

$$= \frac{\int_0^L \frac{1}{2} \cdot \rho \cdot U \cdot D \cdot (C_D + C_L') \cdot \phi_i^y(z)^2 \cdot dz}{2 \cdot \omega_i \cdot M_i} \quad (5.23a)$$

$\zeta_i^{a,v1}$ = vortex induced linear damping

$$= -\frac{\int_0^L \frac{1}{2} \cdot \rho \cdot U \cdot D \cdot Y_1 \cdot \phi_i^2 \cdot dz}{2 \cdot \omega_i \cdot M_i} \quad (5.23b)$$

$$\zeta_i^{a,v2} = \text{vortex induced nonlinear damping} = \frac{\int_0^L \frac{1}{2} \cdot \rho \cdot U \cdot \varepsilon \frac{(\phi_i^y(z) \cdot r_i)^2}{D} \cdot \phi_i^y(z)^2 \cdot dz}{2 \cdot \omega_i \cdot M_i} \quad (5.23c)$$

The amplitude of the across-wind response could become larger if the total damping is negative while it could become smaller if the total damping is positive. Eq. 5.23a brings negative damping in the case of 12-sided cylinder (flat orientation) because $(C_D + C_L^{'})$ is negative in the equation. Eq. 5.23b also brings negative damping while Eq. 5.23c always brings positive damping. In Eq. 5.23, the total damping would be controlled by structural damping (ζ_i), self-excited induced damping ($\zeta_i^{a,se}$) and vortex shedding induced linear damping ($\zeta_i^{a,v1}$) while Eq. 5.23c ($\zeta_i^{a,v2}$) controls the amplitude of the vibration.

When r is small, the quadratic term r^2 is negligible and the structure becomes a linear differential equation with a negative damping. Alternately, when r is large, the term r^2 becomes dominant and the damping becomes positive. Once the total damping is negative, the amplitude of vibration is controlled by Eq. 5.23c.

Figure 5-7 plots the total aerodynamic damping induced by self-excited forces and vortex shedding induced forces and negative of the structural damping as given in Eq. 5.23 for first to fourth modes of vibration (ζ_1^a to ζ_4^a). The aerodynamic damping increases linearly with wind speed. The peaks represent the damping induced by vortex shedding component in "lock-in" region. Peak of aerodynamic damping in second mode exceeds structural damping in second mode for wind speeds of 6.2 – 6.8 mph. Peak of aerodynamic damping in first mode exceeds at wind speed of approximately 30 mph and buffeting will be significant at this speed.

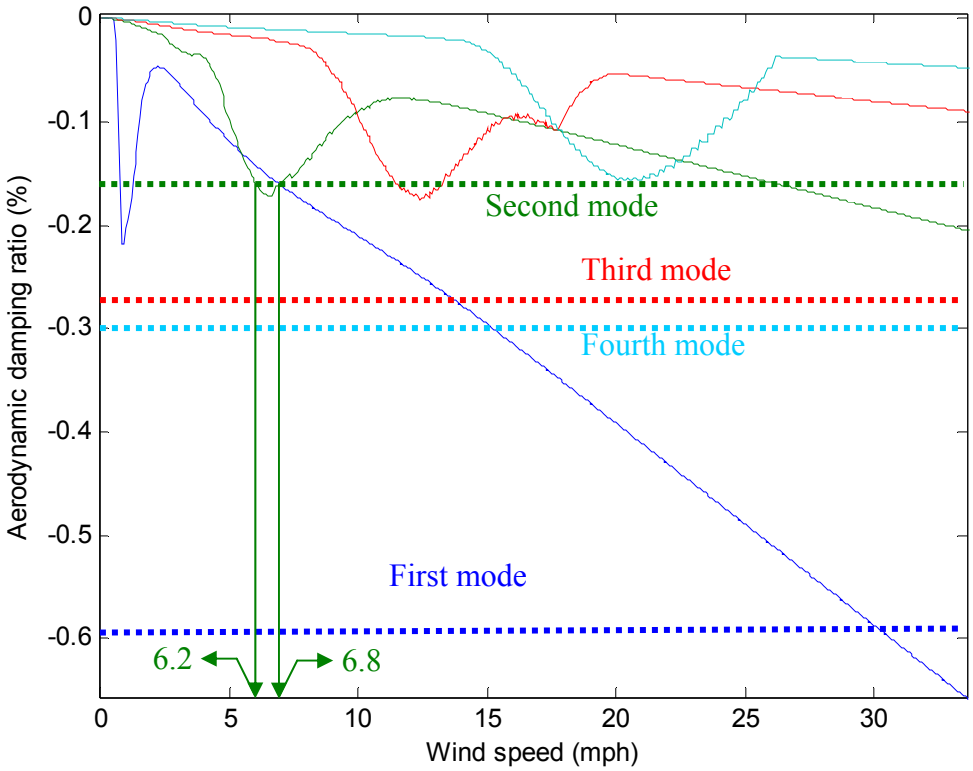

--- First mode structural damping, ζ_1

--- Second mode structural damping, ζ_2

--- Third mode structural damping, ζ_3

--- Fourth mode structural damping, ζ_4

— First mode aerodynamic damping, $\zeta_1{}^a$

— Second mode aerodynamic damping, $\zeta_2{}^a$

— Third mode aerodynamic damping, $\zeta_3{}^a$

— Fourth mode aerodynamic damping, $\zeta_4{}^a$

Figure 5-7. Aerodynamic damping induced by vortex shedding and self excited components

Equation 5.23 can be solved by commercially available software, MATLAB. Figure 5-8 shows the simulated stress-range in lateral-wind direction for a period of 60 seconds for a range of wind speed from 2.5ft/s to 50ft/s with an increment of 2.5ft/s. As shown in this figure, the simulated stress range outside the "lock-in" range seems to be generally proportional to the square of the wind speed and it lies within ±3σ of the mean raw data. The simulated data show smaller stress-range than the average field data. The maximum stress range was determined as 3.82 ksi at 6.6 mph wind speed which is close to the maximum stress range of 3.74 ksi observed in the field at that wind speed. The simulated data like the field observation also shows second mode vibration within 3-8 mph wind speeds.

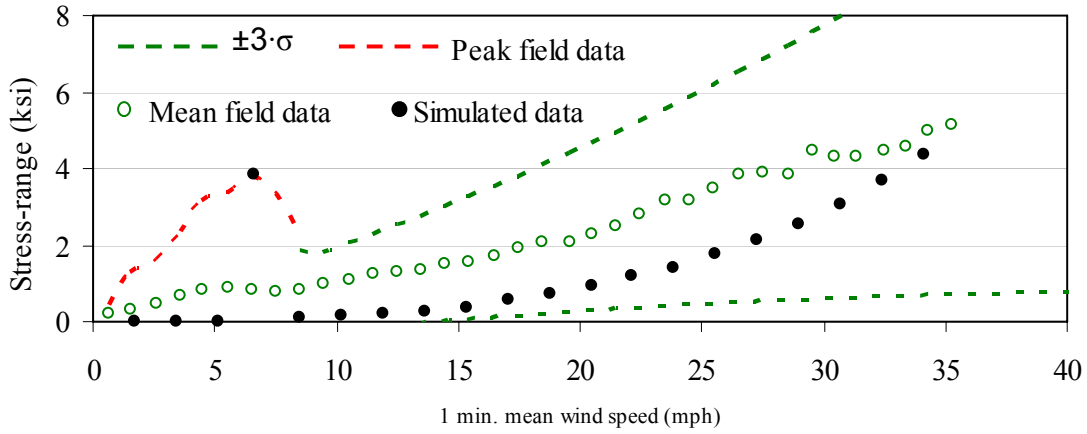

Figure 5-8. Simulated stress-range in across-wind direction

Total time of simulation plays a significant role in the modeling for across-wind response because it takes time to reach a steady-state. The modeling for across-wind response was conducted for 60 seconds which may not be enough. It is difficult to figure out the time needed to reach a steady-state by aerodynamic damping components. To minimize the simulation time, a reasonable initial displacement (in generalized coordinate) or velocity was used in the model. Relatively small or large initial displacement in the model could not produce the steady-state visually within the time of simulation (see Fig. 5-9) and thus several trials were be made to find a reasonable value.

The appropriate initial displacement determined from all the trials for achieving steady-state within 60 seconds in the model and the result of the steady-state (second mode, 1.3 Hz) simulation achieved at a wind speed of 6.6 mph (9.7ft/s) is shown in Fig 5-10.

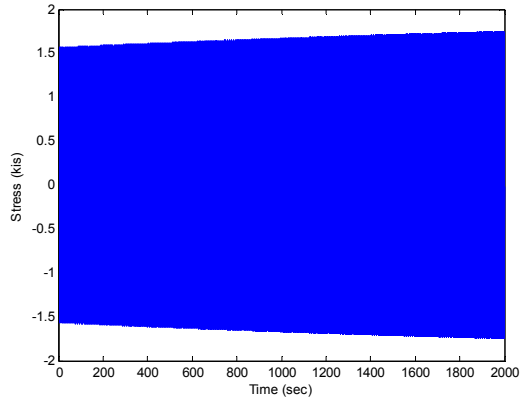

(a) for small initial displacement

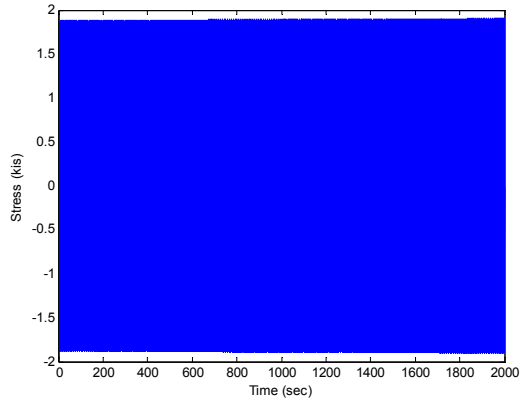

(b) for appropriate initial displacement

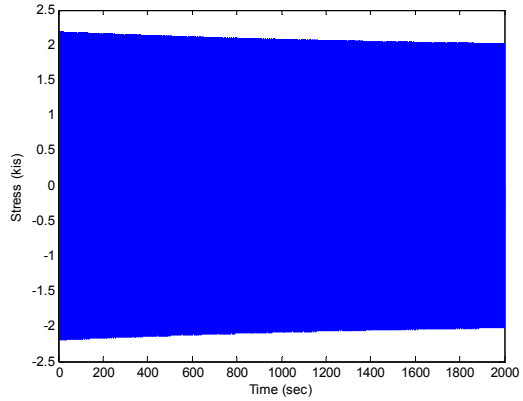

(c) for large initial displacement

Figure 5-9. Stress induced by aerodynamic damping with different initial conditions

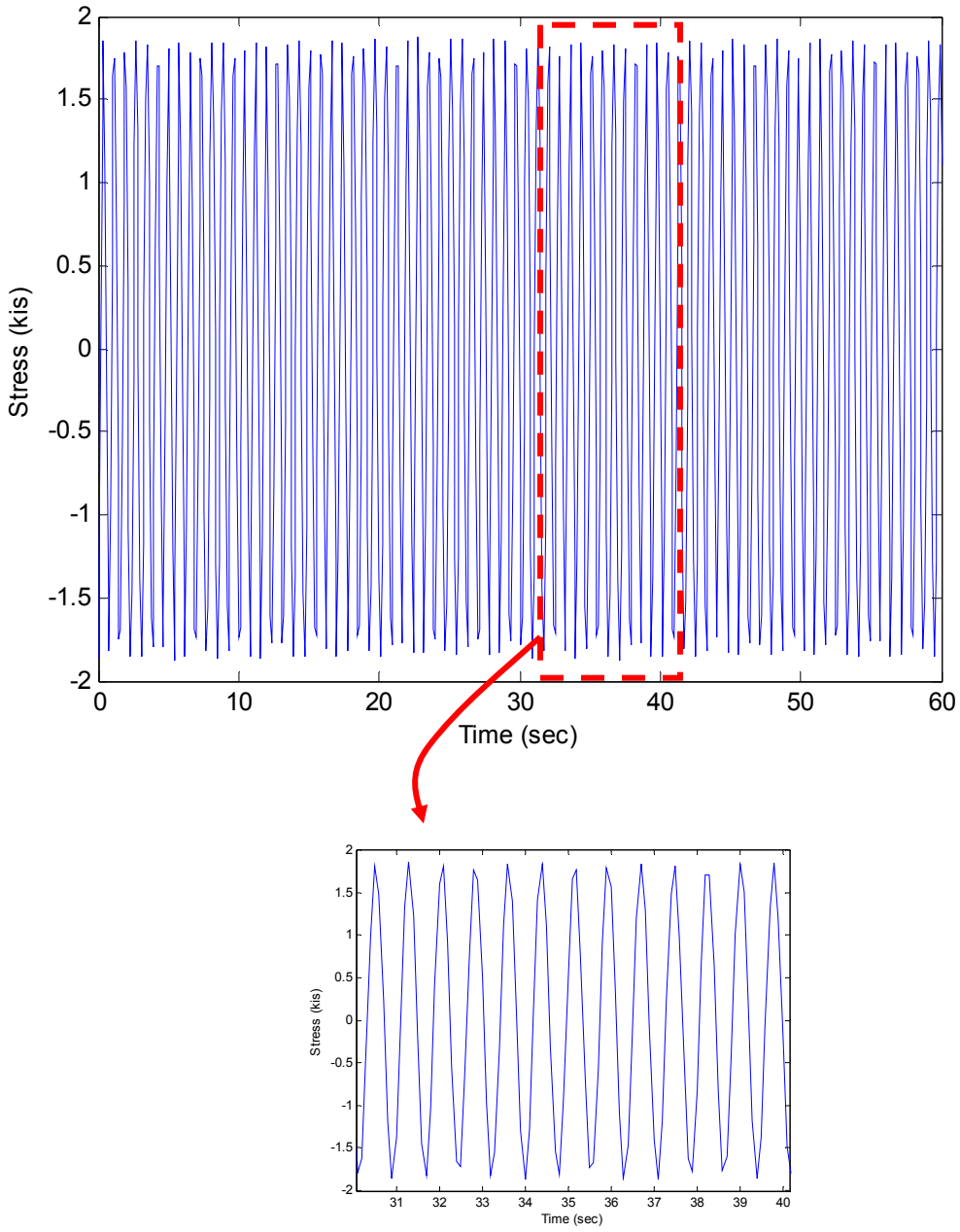

Figure 5-10. Across-wind response of HMLP at wind speed of 6.6mph

6. SUMMARY, CONCLUSIONS, AND RECOMMENDATIONS

6.1. Summary

Recently, there have been a number of failures of High-Mast Light Pole (HMLP) in the U.S. that have been attributed as wind-induced fatigue. It is widely accepted that there is considerable uncertainty in the calculation of wind-induced loads on HMLP in both the American Association of State Highway and Transportation (AASHTO) and the Canadian Highway Bridge Design Code (CAN/CSA) provisions; thus, the current procedure and equations used for wind-induced fatigue design needed to be reevaluated and possibly modified.

A luminary support structure or HMLP is generally susceptible to two primary types of wind loading induced by natural wind gusts or buffeting and vortex shedding, both of which excite the structure dynamically and can cause fatigue damage [7]. Vortex shedding alternatively creates areas of negative pressures on either side of a structure normal to the wind direction. This causes the structure to oscillate transverse to the wind direction. While mathematical models to predict response of two-dimensional sections from vortex shedding and buffeting in the frequency domain exist, there is not a single model that can predict a coupled response resulting from both the phenomena for the full-range of wind speeds and turbulence fields and that too for a three-dimensional structure such as an HMLP. Since the fatigue life of a structure or its components depend on the different number of stress cycles with corresponding mean stress levels and stress amplitudes that the structure experience during its lifetime, the existing frequency-domain models for calculating the response from aerodynamic loads could not be used and so a time-domain model for predicting the response was needed.

The primary objective of this research was to develop a procedure for predicting wind loads in the time domain as induced by vortex shedding and buffeting. To accomplish this, a three-pronged approach was used based on field monitoring of the long-term response of a HMLP subjected to wind-induced vibration, wind tunnel tests of the HMLP cross section to extract its aerodynamic properties and the developed analytical procedure where all the information obtained from the field and wind tunnel tests were used as inputs in the coupled dynamic equations of motion for predicting the wind-induced response and resulting stress of a HMLP. The field monitoring was accomplished by full-scale measurement of response of a HMLP located near Mason City next to I-35. The wind tunnel tests on a section model of the HMLP cross section (12-sided cylinder) were conducted in the Bill James Wind Tunnel in the WiST Laboratory at Iowa State University. Finally, the coupled dynamic model that was developed for predicting the wind-excited response was validated by comparing its simulation results with the data collected from field monitoring for a given wind environment. Agreement between the analytical predictions and field data was found to be very satisfactory. With further refinement of some of the parameters used in the dynamic model, the predictions can be improved even further.

In this study, for the first time, a time-domain coupled model of buffeting and vortex-induced aeroelastic forces was developed and used to predict the response of an actual structure whose response was already known. The study also contributes to the procedure for extraction of

indicial functions that define the buffeting forces and their actual forms in addition to systematically finding other aerodynamic parameters of a 12-sided cylinder. The model was able to predict the vortex-induced response in the second-mode of vibration as was frequently observed in the field. The procedure and mathematical model developed in this study can be used to predict the wind-induced response of other slender and free standing structures as well.

6.2. Conclusions

The following conclusions can be drawn based on the current work as presented in the previous chapters:

- The highest stress ranges were caused by buffeting at wind speeds above 20 mph. Buffeting induced excitation was observed primarily in the first mode of vibration of the HMLP during the long-term monitoring. The maximum stress range was measured as 12.4 ksi at an elevation of 5.75 ft during the long-term monitoring.
- Even though a stress range above the constant amplitude fatigue limit (CAFL) of 2.6 ksi (Category E' [7]) was observed at high wind speeds and predicted by the mathematical model, its frequency of occurrence was small during the monitoring period of 15 months because the cumulative frequency of occurrence of wind speeds above 20 mph was below 5%. Thus, buffeting was not a significant contributor to fatigue damage of HMLP considered in this study subjected to the given wind environment.
- Vortex shedding excitation was observed primarily in the second mode of vibration of the HMLP. This is contrary to that considered in the AASHTO design code. The second-mode vortex shedding vibration in the HMLP was frequently observed at low wind speeds of 3-8 mph and was later verified with the mathematical model. Third-mode vortex shedding vibration was also observed occasionally but it was not found to be stable enough to produce significant stresses. Although the measured stress ranges due to vortex shedding were lower than those caused by buffeting at higher wind speeds, the maximum stress range due to the second-mode vortex shedding excitation was measured to exceed the CAFL of 2.6 ksi that could potentially cause fatigue. The accumulation of a large number of fatigue cycles in second mode of vibration due to vortex shedding occurring at low wind speeds between 3 to 8 mph was much higher than those caused by first mode excitation due to buffeting occurring above 20 mph. Thus, it appears that the second mode response should be considered in the design or vortex-induced excitation of HMLPs.
- For the across-wind response of the HMLP, it was convenient to separate the aerodynamic force on the HMLP into self-excited, buffeting and vortex shedding components. The cross section of the HMLP considered here had negative aerodynamic damping that reduces the inherent damping in the system at higher wind speeds to the extent that the buffeting response could be significant and "galloping" could occur. Therefore, consideration of buffeting in the presence of self-excited forces was deemed necessary and important for this study. This showed that this HMLP is vulnerable to high-amplitude oscillations at much higher wind speeds. Earlier studies missed this fact.

- The critical damping ratio in the second mode of vibration from the pluck test was found to be lower (approximately 0.17%) than that in the first mode of vibration (approximately 0.6%) and this is much lower than the design value. For fatigue design due to vortex shedding, AASHTO recommends using a damping ratio of 0.5% when the actual damping is unknown; similarly the Canadian Bridge Code specifies a damping ratio of 0.75% when experimentally determined values are unavailable. However, these damping ratios used in design codes appear to be not conservative based on the current study. Therefore, a conservative value of damping ratio for the fatigue design due to vortex shedding should be less than 0.5% for poles that are of similar type as considered here.

6.3. Recommendations

Based on the results presented above, the following recommendations are made:

- Several aerodynamic parameters are significant for predicting buffeting and vortex shedding loads on a support structure: the static force coefficients and their slopes with angle of attack, Strouhal number, the lock-in range of wind velocities and amplitude of vortex-induced vibration as a function of Scruton number, aerodynamic admittance functions or indicial functions, etc. These aerodynamic parameters for the 12-sided cylindrical section shape were obtained from wind tunnel testing and mathematical modeling was formulated and its results compared with the data collected from field monitoring. The aerodynamic parameters for shapes other than that studied here are required to fully develop buffeting and vortex-shedding induced loads for various other HMLPs and a parametric study with different structural properties and wind environment would be useful to develop more accurate fatigue design equations. The parametric study should include structural properties such as height of structure, taper ratio, cross-sectional shape, structural damping ratio and mass per unit length, etc, and various wind parameters such as wind terrains and wind climatic zones. This parametric study would be useful in determining the influence of each of these variables and their critical values on the fatigue life of the HMLPs and similar structures. The parametric study will eventually help to improve the equation for static design loads and the associated procedure for fatigue design as given in the design codes.
- To increase the fatigue life of all the HMLPs like the one considered here, it is suggested that this HMLP or Pole 1 be retrofitted like Pole 2. Vortex suppression device such as shroud or damping device could be also used to minimize the vortex induced vibration that was found to be dominant in this study. The time-domain coupled buffeting-vortex shedding model as developed here would be useful in evaluating any of these mitigation measures.

7. REFERENCES

1. Dexter, R. J. and M. J. Ricker. *Fatigue-Resistant Design of Cantilevered Signal, Sign, and Light Supports.* NCHRP Report 469. Washington, DC: Transportation Research Board, National Research Council, 2002.

2. CSA International. *Canadian Highway Bridge Design Code*. Toronto, 2000

3. Dexter, R. J. *Investigation of Cracking of High-Mast Lighting Towers*. Final Report. Iowa Department of Transportation, 2004.

4. Caracoglia, L. Analysis of light pole vibration in Illinois. http://cee.uiuc.edu/nsel/proj/luca.htm, 2007.

5. Foley, C. M. *Structural Analysis of Sign Bridge Structures and Luminaire Supports*. Report WHRP 04-03. Wisconsin Department of Transportation, 2004.

6. Chen, G. *Signal Mast Arm Failure Investigation*. Report RDT 03-010. Missouri Department of Transportation, 2003.

7. American Association of State Highway and Transportation Officials. *Standard Specifications for Structural Support for Highway Signs, Luminaries, and Traffic Signals*. Washington, DC, 2001

8. Bruce, B., et. al. *Iowa's high mast light poles: a proactive management approach*. Proceedings of the 2005 Mid-continent Transportation Research Symposium, 2005

9. American Association of State Highway and Transportation Officials. *Standard Specifications for Structural Support for Highway Signs, Luminaries, and Traffic Signals*. Washington, DC, 1994

10. Fouad H. F., E. A. Calvert, and E. Nunez. *Structural Supports for Highway Signs, Luminaires, and Traffic Signals*. NCHRP Report 411. Washington, DC: Transportation Research Board, National Research Council, 1998.

11. Kaczinski, M. R., R. J. Dexter, and J. P. Van Dien. *Fatigue-Resistant Design of Cantilevered Signal, Sign, and Light Supports*. NCHRP Report 412. Washington, DC: Transportation Research Board, National Research Council, 1998.

12. Fouad H. F., E. A. Calvert, and E. Nunez. *Structural Supports for Highway Signs, Luminaries, and Traffic Signals*. NCHRP Report 494. Washington, DC: Transportation Research Board, National Research Council, 2003.

13. Van Dien, J. P. "Fatigue resistant design of cantilevered sign, signal, and luminaire support structures." Master's Thesis, Lehigh University, 1995.

14. Johns K. W. and R. J. Dexter. *Fatigue Testing and Failure Analysis of Aluminum*

Luminaire Support Structures. ATLSS Report No. 98-06. Lehigh University, 1998.

15. Johns, K. W. and R. J. Dexter. *Fatigue Related Wind Loads on Highway Support Structures*. ATLSS Report No. 98-03. New Jersey Department of Transportation, 1998.

16. Hodgson, I. C. and Robert J. Connor. *Field instrumentation and analysis of prototype and existing light poles on the Bronx-Whitestone bridge*. ATLSS Report No. 03-17. Lehigh University, 2003.

17. Connor, R. J. and Hussam N. Mahmoud. *Failure investigation of two cantilevered sign structures in the City of Hazelton*. ATLSS Report No. 04-24. Lehigh University, 2004.

18. Gregg, F. and B. Patrick Collins. *Traffic signal pole research (Damping)*. Final Report Volume No. 1 (testing and modeling). Wyoming Department of Transportation, 2001.

19. Gregg, F. and B. Patrick Collins. *Traffic signal pole research (Damping)*. Final Report Volume No. 2 (field testing). Wyoming Department of Transportation, 2002.

20. Gray B. D. "Fatigue effects on traffic signal structures." Master's thesis, University of Wyoming, 1999.

21. McManus, P. S. *Evaluation of damping in cantilevered traffic signal structures under forced vibrations*. Master's thesis, University of Wyoming, 2000.

22. South, J. M. *Fatigue analysis of overhead sign and signal structures*. FHWA/IL/PR-115. Illinois Department of Transpiration,, 1994.

23. Fouad, F. H. and Elizabeth Calvert. *Evaluating the design safety of highway structural supports*. UTCA Report number 00218. University Transportation Center at Alabama, 2001.

24. Fouad, F. H. and Elizabeth Calvert. *AASHTO 2001 Design of overhead cantilevered sign supports*. UTCA Report number 00216. University Transportation Center at Alabama, 2004.

25. Davidson, J. S., Fouad H. Fouad, et.al. *Computer-based sign, luminaries, and traffic signal support design tools for state and country engineers*. UTCA Report number 00467. Alabama: University Transportation Center, 2004.

26. Bridge Engineering Software & Technology Center. *Sign bridge analysis and evaluation system (SABRE)*. University of Maryland, Revision 3A, 2000.

27. DelGrego M. and John T. DeWolf. *Field monitoring and evaluation for sign support structures subject to dynamic loads*. JHR 03-291. Connecticut Department of Transportation, 2003.

28. DeWolf, J. T. and Jun Yang. *Stability analysis of truss type highway sign support structures*. JHR 00-280. Connecticut Department of Transportation, 2000.

29. Sreenivas, A. *Wind loads on untethered-span-wire traffic-signal poles*. FHWA/NY/SR-97/126. New York State Department of Transportation, 1997.

30. Koenigs, M. T., Tamer A. Botros, et.al. *Fatigue strength of signal mast arm connections*. FHWA/TX-04/0-3178-2. Texas Department of Transportation, 2003

31. Chen, G., et.al. *Signal mast arm fatigue failure investigation*. RDT 03-010. Missouri Department of Transportation, 2003.

32. Cook, R. A., D. Bloomquist, et.al. *Design, testing, and specification of a mechanical damping device for mast arm traffic signal structures*. BC-050. Florida Department of Transportation, 2000.

33. McDonald, J. R., et.al. *Wind load effects on signs, luminaries, and traffic signal structures*. 1303-F. Texas Department of Transportation, 1995.

34. Lindt, J. W. and Jonathan S. Goode. *Development of a reliability-based design procedure for high-mast lighting structural supports in Colorado*. SRR-91. Colorado Department of Transportation, 2006.

35. Goode, J. S. "Correlated wind turbulence and aeroelastic instability modeling for 3-D time-domain analysis of slender structural systems." Ph.D. Dissertation, Colorado State University, 2007.

36. Dyrbye, C. and Svend O. Hansen. *Wind loads on structures*. New York, NY: John Wiley & Sons, 1997.

37. Garrett, J. L. "Flow-induced vibration of elastically supported rectangular cylinders." Ph.D. Dissertation, Iowa State University, 2003.

38. Blevins, R. D. *Flow-induced vibratio., 2nd ed*. New York, NY: Van Nostrand Reinnhold, 1990.

39. Simiu E. and R. H. Scanlan. *Wind Effects on Structures, Fundamentals and Applications to Design.* 3rd ed. New York, NY: John Wiley & Sons, 1996.

40. Sockel, H. *Wind-excited vibrations of structures*. New York, NY: Springer-Verlag Wien, 1994.

41. Sears, W. R. *Some aspects of non-stationary airfoil theory and its practical applications*. Journal of the Aeronautical Science. 8:104-108, 1941.

42. Liepmann, H. W. *On the application of statistical concepts to the buffeting problem*, Journal of the Aeronautical Science. 19:793-800, 1952.

43. Jancauskas, E. D. “The cross-wind excitation of bluff structures and the incident turbulence mechanism.” Ph.D. Dissertation, Melbourne, Australia: Monash University, 1983.

44. Jancauskas, E. D. and W. H. Melbourne. *The aerodynamic admittance of two-dimensional rectangular section cylinders in smooth flow*. Journal of Wind Engineering and Industrial Aerodynamics. 23:395-408, 1986.

45. Scanlan, R. H. and N. P. Jones. *A form of aerodynamic admittance for use in bridge aeroelastic analysis*. Journal of Fluids and Structures. 13:1017-1027, 1999.

46. Scanlan, R. H. *Problematics in formulation of wind-force models for bridge decks*. Journal of Engineering Mechanics. 119:7, 1993.

47. Holmes, J. D. *Wind loading of structures*. New York, NY: Taylor & Francis, 2001.

48. Hatanaka A. and H. Tanaka. *New estimation method of aerodynamic admittance function*. Journal of Wind Engineering and Industrial Aerodynamics. 90:2073-2086, 2002.

49. Peil, U. and Matthias Behrens. *Aerodynamic admittance models for buffeting excitation of high and slender structures*. Journal of Wind Engineering and Industrial Aerodynamics. 95:73-90, 2007.

50. Jones, R. T. *The unsteady lift on a wing of finite aspect ratio*. NACA Report 681. Langley, VA : U.S. National Advisory Committee for Aeronautics, 1940.

51. Chen, X. and Ahsan Kareem. *Advances in modeling of aerodynamic forces on bridge decks*. Journal of Engineering Mechanics. 128:11, 2002.

52. Chen, X. and Ahsan Kareem. *Time domain flutter and buffeting response analysis of bridge*. Journal of Engineering Mechanics. 126:1, 2000.

53. Scanlan, R. H. and Jean-Guy Béliveau. *Indicial aerodynamic functions for bridge decks.* Journal of Engineering Mechanics. 100:4, 1974.

54. Scanlan, R. H. *Role of indicial functions in buffeting analysis of bridges*. Journal of Structural Engineering. 110:7, 1984.

55. Caracoglia, L. and N. P. Jones. *Time domain vs. frequency domain characterization of aeroelastic forces for bridge deck sections*. Journal of Wind Engineering and Industrial Aerodynamics. 91:371-402, 2003.

56. Zhang, X. and J. M. W. Brownjohn. *Time domain formulation of self-excited forces on bridge deck for wind tunnel experiment*. Journal of Wind Engineering and Industrial Aerodynamics. 91:723-736, 2003.

57. Costa, C. and Claudio Borri. *Application of indicial functions in bridge deck aeroelasticity*. Journal of Wind Engineering and Industrial Aerodynamics. 94:859-881, 2006.

58. Costai, C. *Aerodynamic admittance functions and buffeting forces for bridges via indicial functions*. Journal of Fluids and Structures. 23:413-428, 2007.

59. Liu, H. *Wind Engineering*. New Jersey: Prentice Hall, 1991

60. Kolousek, V., et al. *Wind effects on Civil Engineering Structures*. New York: Elsevier Science Publishing Company, 1984.

61. Kitagawa, T., et al. *An experimental study on vortex-induced vibration of a circular cylinder tower at a high wind speed*. Journal of wind Engineering and Industrial Aerodynamics. 69-71:731-744, 1997.

62. Bosch, H. R. and R. M. Guterres, *Wind tunnel experimental investigation on tapered cylinders for highway support structures*. Journal of wind Engineering and Industrial Aerodynamics. 89:1311-1323, 2001.

63. James, W. D. "Effects of Reynolds number and corner radius on two-dimensional flow around octagonal, dodecagonal and hexdecagonal cyliners." PhD Dissertation, Iowa State University, 1976.

64. Balasubramanian, S., et al. *An experimental investigation of the vortex-excited vibrations of pivoted tapered circular cylinders in uniform and shear flow*. Journal of wind Engineering and Industrial Aerodynamics. 89:757-784, 2001.

65. Sumner, D., et al. *Vortex shedding from a finite circular cylinder of small aspect ratio*. CSME 2004 Forum. 625-633, 2004.

66. Park, C. and Sang-Joon Lee. *Free end effects on the near wake flow structure behind a finite circular cylinder*. Journal of wind Engineering and Industrial Aerodynamics. 88:231-246, 2000.

67. Gabbai, R. D. and H. Benaroya. *An overview of modeling and experiments of vortex-induced vibration of circular cylinders.* Journal of Sound and Vibration. 282:575-616, 2005.

68. Barhoush, H. M. "Analytical model of long span bridge vortex-shedding response." Ph.D. Dissertation, University of Miami, 1993.

69. Kim, S. and Hiroshi Sakamoto. *Characteristics of fluctuating lift forces of a circular cylinder during generation of vortex excitation*. Wind and Structures. 9:2:109-124, 2006.

70. Gupta, H. and P. P. Sarkar. *Identification of vortex-induced response parameters in time domain.* Journal of Engineering Mechanics. 122:11:1031-1037, 1996.

71. Diana, G., et al. *Complex aerodynamic admittance function role in buffeting response of a bridge deck*. Journal of wind Engineering and Industrial Aerodynamics. 90:2057-2072, 2002.

72. Goswami, I., R. H. Scanlan, and N. P. Jones. *Vortex shedding from circular cylinders: Experimental data and a new model*. Journal of wind Engineering and Industrial Aerodynamics. 41-44:763-774, 1992.

73. Goswami, I., R. H. Scanlan, and N. P. Jones, *Vortex-induced vibration of circular cylinders. I: Experimental data*. Journal of Engineering Mechanics. 119:11:2270-2287, 1993.

74. Goswami, I., R. H. Scanlan, and N. P. Jones, *Vortex-induced vibration of circular cylinders. II: New model*. Journal of Engineering Mechanics. 119:11:2288-2302, 1993.

75. Scanlan, R. H. *Bridge flutter derivatives at vortex lock-in. Journal of Structural Engineering*. 124:4:450-458, 1998.

76. Ehsan, F. and R. H. Scanlan. *Vortex-induced vibrations of flexible bridges*. Journal of Engineering Mechanics. 116:6:1392-1411, 1990.

77. Li, Q. S., et al. *Full-scale measurements and numerical evaluation of wind-induced vibration of a 63-story reinforced concrete tall building*. Engineering Structures. 26:1779-1794, 2004.

78. Li, Q. S., et al. *Full scale measurements of wind effects on tall building. Journal of wind Engineering and Industrial Aerodynamics*. 74-76:741-750, 1998.

79. Ruscheweyh, H. and Thomas Galemann. *Full-scale measurements of wind-induced oscillations of chimneys*. Journal of wind Engineering and Industrial Aerodynamics. 65:55-62, 1996.

80. Ruscheweyh, H., et al., *Long-term full-scale measurements of wind induced vibrations of steel stacks.* Journal of wind Engineering and Industrial Aerodynamics. 74-76:777-783, 1998.

81. Tranvik, P. and Goran Alpsten. *Dynamic Behavior under Wind Loading of a 90m Steel Chimney*. Report S-01041 and 9647-3. Sweden: Alstom Power Sweden, 2002.

82. Miyahiota, K., et al., *Full-scale measurements of wind-induced responses on the Hamamatsu ACT Tower*. Journal of wind Engineering and Industrial Aerodynamics. 74-76:943-953, 1998.

83. Pagnini, L. C. and Giovanni Solari, *Damping measurements of steel poles and tubular towers*. Engineering Structures. 23:1085-1095, 2001.

84. Robertson, A. P., et al. *Wind-induced fatigue loading of tubular steel lighting columns*. Wind and Structures. 4:163-176, 2001.

85. Iowa Wind Energy Institute under Iowa Energy Center. *Estimated average annual wind speeds*. http://www.energy.iastate.edu/renewable/wind/images/windmap-iowa_annual.gif, 2007.

86. Connor, R. J. and I. C. Hodgson. *Field instrumentation and testing of high-mast lighting towers in the state of Iowa*, Final Report. Iowa Department of Transportation, 2006.

87. Swanson Analysis System, Inc. ANSYS User's Manual for Revision 5.0 Procedures. Huston, PA, 1992.

88. Structural Engineering Institute. *Minimum design loads for buildings and other structures*: SEI/ASCE 7-05 (ASCE Standard No. 7-05). The American Society of Civil Engineers, 2007.

89. Garrett, J. L. "Flow-induced vibration of elastically supported rectangular cylinders." Ph.D. Dissertation, Iowa State University, 2003.

90. Jorgensen, F. E. *How to measure turbulence with hot-wire anemometers – a practical guide*. Dantec Dynamics, 2005.

91. Goldstein, R. J. *Fluid Mechanics Measurements*, Hemisphere Publishing Corporation. New York, 1983.

92. Scruton, C. *An Introduction to Wind Effects on Structures*. Engineering Design Guides. 40, BSI & CEI, 1981.

93. Shinozuka, M. *Simulation of Multivariate and Multidimensional Random Processes*. The Journal of the Acoustical Society of America. 49:357-368, 1971.

94. Yang, W. W. and T. Y .P. Chang. *Numerical simulation of turbulent fluctuations along the axis of a bridge.* Engineering Structures. 20:9:837-848, 1998.

95. Sarkar, P. P. "New identification methods applied to the response of flexible bridges to wind." Ph.D. Dissertation, Johns Hopkins University, 1992.